TUMOR RESPONSIVE TARGETED MULTIFUNCTIONAL NANOSYSTEMS FOR CANCER IMAGING, CHEMO- AND siRNA THERAPY

By

RONAK SAVLA

A Dissertation submitted to the

Graduate School-New Brunswick

Rutgers, The State University of New Jersey

In partial fulfillment of the requirements

for the degree of

Doctor of Philosophy

Graduate Program in Pharmaceutical Science

written under the direction of

Professor Tamara Minko, PhD

and approved by

_____
_____
_____
_____

New Brunswick, New Jersey

January 2015

ABSTRACT OF THE DISSERTATION

Tumor Responsive Targeted Multifunctional Nanosystems for Cancer Imaging, Chemo- and siRNA Therapy

By RONAK SAVLA

Dissertation Director:
Tamara Minko, PhD.

Cancer is one of the most insidious diseases. Compromising of over 100 different types and sharing the unifying factors of uncontrolled growth and metastasis, unmet clinical needs in terms of cancer diagnosis and treatment continue to exist. It is widely accepted that most forms of cancer are treatable or even curable if detected before widespread metastasis occurs. Nearly a quarter of deaths in the United States is the result of cancer and it only trails heart disease in terms of annual mortality.

Surgery, chemotherapy, and radiation therapy are the primary treatment modalities for cancer. Research in these procedures has resulted in substantial benefits for cancer patients, but there is still room for an improvement. However, a time has been reached at which it appears that the benefits from these modalities have been reached the maximum. Therefore, it is vital to develop new strategies for the diagnosis and treatment of cancer.

The field of nanotechnology is concerned with structures in the nanometer size range and holds the potential to drastically impact and improve the lives of patients suffering from cancer. Not only can nanotechnology improve current methods of diagnosis and treatment, it has a possibility of introducing newer and better modalities.

The overall purpose of this work is to develop novel nanotechnology-based methodologies for the diagnosis and treatment of various forms of cancers. The first aim of the project is the development of a multifunctional targeted nanosystem for the delivery of siRNA to overcome drug resistance. The second aspect is the synthesis of a quantum dot-based delivery system that releases drug in response to pH changes. The third aim is the development of a targeted, tumor environment responsive magnetic resonance nanoparticle contrast agent coupled with a nanoparticle-based treatment.

DEDICATION

To my wonderful parents;

Whose sacrifices, blessings, and love allowed me to succeed

To my advisor, Professor Tamara Minko,

Who has helped and guided me and become an inspiration

To my sister;

Who loves unconditionally and keeps life interesting

ACKNOWLEDGEMENTS

I would not be here without the generous help of so many wonderful people. Therefore to me, this is the most important part of my dissertation. First, I would like to thank my advisor, Professor Tamara Minko. She exemplifies what a great advisor should be and has become a role model for me. Her guidance, support, passion, and belief in her students are awe inspiring.

I would like to thank my committee members for taking time from their busy schedules to provide suggestions: Professors Guofeng You, Leonid Kagan, and Huixin He. I would like to further thank Dr. He because she accepted me into her lab after my freshman year of college and the experience of working in her lab solidified my interest in research.I also would like to express my gratitude to our collaborators and co-authors, Professors Lorna Rodriguez (Cancer Institute of New Jersey) and Suzie Chen (Department of Chemical Biology, EMSOP), for valuable discussion and providing ovarian cancer tissues from patients and mice with spontaneously developed melanoma.

Very few people are blessed to meet someone, who becomes a truly close friend. Someone who makes the good times more enjoyable and softens the blows of difficult times. Someone who is inspiring and for whom you want to better yourself. I would like to thank my friend and "partner in crime," Vera Ivanova. Our adventures were filled with perpetual laughter only interrupted by pauses of smiling to allow the pain in our cheeks and stomachs to subside. Reflecting back on our time as lab mates does not signify the end of a chapter or book; rather it is only the prologue of our friendship.

I would also like to thank my former and present colleagues: Dr. Oleh Taratula, Dr. Olga Garbuzenko, Dr. Min Zhang, Dr. Vatsal Shah, John Praskavich, Milin Shah, and Andriy Kuzmov.

We thank Dr. D.C. Reimer from Rutgers Laboratory Animal Services for his help with the implementation of an orthotopic mouse model of human lung cancer and Mr. D. Adler from Rutgers Molecular Imaging Center for his assistance with obtaining and analysis of animal images.

I would like to extend my gratitude to office staff in the Department of Pharmaceutics: Marianne Shen; Sharana Taylor; and Hui Pung. They work arduously behind the scenes to ensure everything runs smoothly for the rest of the department.

I would like to thank Dean Joseph Barone and Dr. Michael Toscani. Their help and encouragement has helped me professionally. I hope to continue to build our relations to continue to gain from their wisdom.

My motivation to succeed is derived from the love, support, and sacrifices of my parents. They are willing to do whatever it takes to see their children succeed. They always put their children's needs before their own. Even though they were not able to receive higher education, their mission is to have their children reach beyond their potentials. I cannot think of any way to adequately repay them for everything they have done for me except to make them proud. My younger sister is a continuous reminder to not take life too seriously and remain a kid at heart. It is through her, I have learned what it means to care for and love another person.

Finally, I would like to extend my gratitude to everyone, who has supported me throughout my life.

This research was supported in part by grants R01 CA111766 and R01 CA138533 from the National Cancer Institute.

TABLE OF CONTENTS

ABSTRACT OF THE DISSERTATION..... ii
DEDICATION..... iv
ACKNOWLEDGEMENTS..... v
LIST OF TABLES..... xii
LIST OF FIGURES..... xiii
1 INTRODUCTION..... 1
2 BACKGROUND AND SIGNIFICANCE..... 7
2.1 Diagnosis of Cancer..... 7
2.2 Chemotherapeutics for the Treatment of Cancer..... 8
2.2.1 Limitations of Therapeutic Efficacy..... 13
2.3 siRNA as a Novel Treatment Modality..... 14
2.3.1 siRNA vs DNA Nanoparticle-Based Delivery..... 17
2.4 Nanoparticles as Multifunctional Tools..... 19
2.5 Nanoparticle Systems for Therapy..... 20
2.5.1 Dendrimers..... 21
2.5.2 Lipid Particles..... 24
2.6 Nanoparticles for Diagnosis..... 26
2.6.1 Quantum Dots..... 29
2.6.2 Superparamagnetic Iron Oxide Nanoparticles (SPIONs)..... 32
2.6.3 Manganese Oxide Nanoparticles..... 33
2.7 Cancer Targeting..... 34
2.7.1 Luteinizing Hormone-Releasing Hormone (LHRH)..... 35
2.7.2 Mucin Proteins..... 36
3 SPECIFIC AIMS..... 44
4 EVALUATION OF THE EFFECT OF DENDRIMER GENERATION ON siRNA CONSENSATION AND GENE SILENCING..... 48
4.1 Introduction..... 48
4.2 Materials and Methods..... 51
4.2.1 Materials..... 51
4.2.2 Cell Line..... 52
4.2.3 Ethidium Bromide Dye Displacement Assay..... 53
4.2.4 Formulation of siRNA-Dendrimer Complexes..... 53
4.2.5 Atomic Force Microscopy (AFM)..... 54
4.2.6 Agarose Gel Retardation Assay..... 54
4.2.7 Dynamic Light Scattering (DLS)..... 54
4.2.8 *In vitro* Cytotoxicity..... 55
4.2.9 Cellular Internalization..... 55
4.2.10 Gene Expression..... 56
4.2.11 Statistical Analysis..... 57
4.3 Results..... 58
4.3.1 Evaluation of Interaction Between siRNA and PPI Dendrimers of Different Generations by EtBr Displacement Assay..... 58

4.3.2 Size and Morphology of Formulated siRNA-Dendrimer Complexes……. 59
4.3.3 Cellular Internalization and Intracellular Localization of siRNA-Dendrimer Complexes…… 60
4.3.4 Gene Silencing Efficiency of siRNA-Dendrimer Complexes *in vitro*…… 61
4.3.5 *In vitro* Cytotoxicity of PPI Dendrimers…… 62
4.4 Discussion…… 63
4.5 Conclusions…… 69
5 MULTIFUNCTIONAL NANOMEDICINE PLATFORM FOR CANCER SPECIFIC DELIVERY OF siRNA BY SUPERPARAMAGNETIC IRON OXIDE NANOPARTICLES-DENDRIMER COMPLEXES…… 77
5.1 Introduction…… 77
5.2 Materials and Methods…… 81
5.2.1 Materials…… 81
5.2.2 Superparamagnetic Iron Oxide (SPIO) Nanoparticles preparation…… 82
5.2.3 Ethidium Bromide Dye Displacement Assay…… 83
5.2.4 Preparation of SPIO-PPI G5-siRNA Complexes…… 85
5.2.5 Modification of SPIO-PPI G5-siRNA Complexes with PEG and LHRH…… 85
5.2.6 Degree of PEGylation…… 86
5.2.7 Agarose Gel Retardation Assay…… 86
5.2.8 Evaluation of LHRH Peptide Reaction with SPIO-PPI G5-siRNA Complexes…… 87
5.2.9 Dynamic Light Scattering…… 88
5.2.10 Atomic Force Microscopy…… 88
5.2.11 Cell Lines…… 89
5.2.12 Cellular Internalization of siRNA…… 89
5.2.13 *In vitro* Cytotoxicity…… 90
5.2.14 Gene Expression…… 91
5.2.15 *In vivo* Study…… 92
5.2.16 Statistical Analysis…… 92
5.3 Results…… 93
5.3.1 Mixture of SPIO Nanoparticles and PPI G5 as a Carrier for siRNA Delivery…… 93
5.3.2 Characterization of siRNA Complexes…… 94
5.3.3 PEGylation and *in vitro* Transfection of siRNA Complexes…… 95
5.3.4 Specific Targeting of SPIO-PPI G5-siRNA Complexes to Cancer Cells by LHRH Peptide…… 96
5.3.5 *In vitro* Cytotoxicity of siRNA Complexes…… 99
5.3.6 Co-Delivery of siRNA and an Anticancer Drug…… 99
5.3.7 Antitumor Activity…… 100
5.4 Discussion…… 101
5.5 Conclusions…… 105
6 TUMOR TARGETED QUANTUM DOT-MUCIN 1 APTAMER-DOXORUBICIN CONJUGATE FOR IMAGING AND TREATMENT OF CANCER…… 114
6.1 Introduction…… 114

6.2 Materials and Methods…… 121
6.2.1 Materials…… 121
6.2.2 Synthesis of Quantum Dot-MUC 1 Aptamer Conjugates…… 122
6.2.3 Synthesis of Quantum Dot-MUC1 Aptamer-Doxorubicin Conjugates….. 123
6.2.4 Synthesis of Quantum Dot-Doxorubicin Conjugates…… 123
6.2.5 Determination of Doxorubicin Loading…… 124
6.2.6 Hydrolytic Release of Doxorubicin…… 124
6.2.7 Cell Line…… 125
6.2.8 Cytotoxicity Assay…… 125
6.2.9 Cellular Internalization and Localization…… 125
6.2.10 Animal Tumor Model, *in vivo* Imaging and Organ Distribution…… 126
6.2.11 Statistical Analysis…… 126
6.3 Results…… 127
6.4 Discussion…… 129
6.5 Conclusions…… 136
7 TUMOR-TARGETED RESPONSIVE NANOPARTICLE-BASED SYSTEMS FOR MAGNETIC RESONANCE IMAGING AND THERAPY…… 143
7.1 Introduction…… 143
7.2 Materials and Methods…… 148
7.2.1 Materials…… 148
7.2.2 Synthesis of Mn_3O_4 Hydrophobic Cores…… 150
7.2.3 Synthesis of Water Soluble Mn_3O_4 Nanoparticles (NH_2/MAL Mn_3O_4 NPs) 150
7.2.4 Conjugation of MMP2 Cleavable Peptide (MMP2/MAL Mn_3O_4 NPs)…… 151
7.2.5 Attachment of LHRH Targeting Moiety (MMP2/LHRH Mn_3O_4 NPs)…… 151
7.2.6 Attachment of Anti-Melanoma Antibody (MMP2/ab733 Mn_3O_4 NPs)…… 152
7.2.7 Quantification of Manganese Content in Mn_3O_4 NP Formulations…… 153
7.2.8 MMP2 Gene Expression…… 153
7.2.9 Digestion of MMP2-Cleavable Peptide…… 154
7.2.10 Synthesis of Nanostructured Lipid Carriers (NLCs)…… 154
7.2.11 Vemurafenib HPLC Calibration Curve…… 155
7.2.12 Vemurafenib Entrapment Efficiency and Loading in NLCs…… 156
7.2.13 NLC Drug Entrapment Stability…… 156
7.2.14 Size Distribution and Cytotoxicity…… 156
7.2.15 Genotoxicity…… 157
7.2.16 Cancer Cells…… 158
7.2.17 Animal Cancer Models…… 160
7.2.18 *In vivo* Optical and Magnetic Resonance Imaging…… 160
7.2.19 Statistical Analysis…… 161
7.3 Results…… 162
7.3.1 Synthesis and Characterization of Water Soluble Manganese Oxide Nanoparticles…… 162
7.3.2 Synthesis and Characterization of Vem-NLCs…… 164
7.3.3 Cytotoxicity and Genotoxicity of Nanoparticle Formulations…… 166
7.3.4 *In vivo* Animal Magnetic Resonance Imaging…… 166

7.4 Discussion..... 168
7.5 Conclusions..... 177
8 REFERENCES..... 186

LIST OF TABLES

Table 1.1 Stage at diagnosis and 5-year survival for selected cancer types…… 6
Table 7.1 Size of manganese oxide nanoparticles…… 178
Table 7.2 Increase in magnetic resonance signal intensity post-dose…… 179

LIST OF FIGURES

Figure 2.1 Mechanism of gene silencing…… 40
Figure 2.2 Nanoparticle carriers…… 41
Figure 2.3 Structure of PPI G3 with labeled regions: core; interior branches; interior cavity; and terminal groups…… 42
Figure 2.4 Structure of DNA aptamer targeted for MUC1 surface protein. Structure with internal base pairing predicted using mfold software…… 43
Figure 4.1 Ethidium bromide dye assay for binding affinity…… 71
Figure 4.2 A) Evaluation of the siRNA complexion with PPI dendrimers by gel retardation assay…… 72
Figure 4.3 Representative AFM images of complexes formed by siRNA in the presence of dendrimers…… 73
Figure 4.4 Size distributions of siRNA-dendrimer complexes and internalization of siRNA-dendrimer complexes by A549 human lung cancer cells…… 74
Figure 4.5 Confocal microscopy images of A549 human lung cancer cells incubated with siRNA-dendrimer complexes…… 75
Figure 4.6 The effect of incubation of A549 human lung cancer cells with siRNA-dendrimer complexes on the expression of BCL2 mRNA…… 76
Figure 5.1 The preparation of tumor-targeted, stable siRNA nanoparticles…… 106
Figure 5.2 siRNA complexation efficiency of SPIO nanoparticles and PPI G5 dendrimer evaluated by the ethidium bromide dye displacement assay and agarose gel electrophoresis…… 107
Figure 5.3 Size distributions of 5 nm SPIO-PPI G5-siRNA complexes prior and after modification with PEG and targeting LHRH peptide and representative atomic force microscope image of the formed nanoparticles…… 108
Figure 5.4 Representative fluorescence microscopic images of SPIO-PPI G5- siRNA complexes after incubation with LHRH-positive A549 and LHRH-negative SKOV-3 cancer cells…… 109
Figure 5.5 Image of RT-PCR products and expression of the *BCL2* gene in human A549 and SKOV-3 cancer cells after treatment with SPIO-PPI G5- siRNA complexes…… 110
Figure 5.6 Representative confocal microscopy images of A549 human cancer cells incubated for 24 h with SPIO-PPI G5-siRNA-PEG-LHRH…… 111
Figure 5.7 Cytotoxicity of SPIO-PPI G5- siRNA complexes with and without cisplatin against A549 human cancer cells. Means ± SD are shown…… 112
Figure 5.8 Antitumor activities of different formulations…… 113
Figure 6.1 Diagnosis, surgery and chemotherapy in treatment of ovarian cancer…… 137
Figure 6.2 Synthesis of quantum dot- MUC1 aptamer- doxorubicin conjugate…… 138
Figure 6.3 Characterization of non-modified quantum dots- doxorubicin conjugates…… 139
Figure 6.4 Intracellular localization of quantum dot formulations in multidrug resistant A2780/AD human ovarian carcinoma cells…… 140
Figure 6.5 Cytotoxicity of different formulations of quantum dots…… 141
Figure 6.6 Organ and tumor content of non-modified quantum dots and tumor-targeted by MUC1 aptamer QD conjugate…… 142

Figure 7.1 Size distribution of the size of PEGylated Mn_3O_4 nanoparticles before and after storage (164 days) and chemical structures of MMP2 cleavable and LHRH cancer targeting peptides…… 180
Figure 7.2 Expression of MMP2 mRNA and cleavage of MMP2 peptide after incubation with human MMP2 enzyme……. 181
Figure 7.3 Cytotoxicity of nanoparticles to healthy cells and cytotoxicity of free non-conjugated vemurafenib (Vem) and NLC-encapsulated Vem in COLO 829 metastatic melanoma cells…… 182
Figure 7.4 Genotoxicity of nanoparticles……. 183
Figure 7.5 Enhancement in MRI sensitivity and specificity by cancer-targeted Mn_3O_4 nanoparticles…….... 184
Figure 7.6 Distribution of cancer-targeted Mn_3O_4 nanoparticles and enhancement in MRI signal intensity…… 185

1 INTRODUCTION

The term cancer refers to a group of over 100 diseases that are characterized by having features such as uncontrolled growth, local tissue invasion, and distant metastasis. It is thought to develop from cells, which have altered growth control mechanisms and proliferation. Cancer is the leading cause of death in Americans younger than eighty-five years of age. [1, 2]. The goal of reducing morbidity and mortality from cancer lies in improved diagnosis and treatment of the disease. Most cancers are diagnosed when the cancer has spread to distant sites (Table 1) [3].Because of its superficial appearance, melanoma of the skin tends to be detected at early stages. However, the incidence for melanoma has been increasing whereas the opposite holds true for most other forms of cancer. When detected at earlier stages, studies have demonstrated that most cancers are treatable if not curable. As shown in Table 1, the 5-year survival is highest for early stages of cancers, but drops precipitously at advanced stages.

The ideal methods for diagnosis and treatment have remained elusive despite the tremendous advancements. Diagnosis is heavily dependent on physical exams, biomarker tests or imaging. Unfortunately, each screening method lacks the sensitivity to diagnose cancer at its earliest stages. After diagnosis, treatment is the next logical step. Cancer treatment typically involved a combination of different strategies: surgery; radiation; chemotherapy; and biologic therapy. [1, 4]. Because of the lagging nature of diagnosis, patients typically receive treatment after the cancer has metastasized.

Tumors consist of heterogenous populations of cells that are at various phases of the cell cycle. This presents a barrier for single agent chemotherapy since most chemotherapy agents are cell cycle specific. This has resulted in combination chemotherapy regimens as the standard of care. Even though combination regimens are effective, cancers are usually diagnosed when they are at advanced stages. Advanced stage cancers are usually large in size and have multiple metastases. It is difficult to deliver therapeutics to cells located at the innermost position of the tumor [4]. Also, chemotherapeutics may not be able to distribute to all sites of metastases.

In essence, cancer cells are the same as normal healthy cells. However, dysregulation of genetic control make them susceptible to uncontrolled growth and metastasis. This presents difficulty in designing and delivery of therapeutic to kill cancer cells and avoid damaging healthy cells. Certain cell markers that are overexpressed can be used to help guide therapy. Not only will guided therapy spare healthy cells, it can also increase concentrations of therapeutics in the tumor environment. Luteinizing hormone releasing hormone receptor and mucin-1 receptor are found to be overexpressed on the surface of many epithelial carcinomas. Many extracellular components are overexpressed as well. Matrix metalloproteinases are extracellular enzymes that help shape the extracellular matrix. Levels of these enzymes have been found to be elevated in cancers with high metastatic potential.

A newer method in the arsenal to fight cancer is RNA interference. The primary belief is that exogenous administration of double stranded RNA or short interfering RNA (siRNA) can depress the expression of genes of interest. The applicability in cancer therapeutic is that most cancers have overexpression or overt “ON” signal for genes related to growth. However, RNA molecules lack adequate stability properties for systemic administration and must be packaged in a suitable carrier to reach therapeutic concentrations at target sites.

Theranostics is an emerging field in medical research that is believed by many to improve overall patient therapy and outcome by combining diagnostic and specific therapeutic properties [5]. Nanoparticles have many of the properties that are sought in theranostics applications. Imaging capabilities of nanoparticles would allow for non-invasive diagnosis and simultaneous delivery of therapeutic agents can accelerate therapy [6].

Nanotechnology is a research area with broad goals. Overall, nanotechnology research is concerned with matter or structures with dimensions between 3 and 200 nm [7]. Others restrict the definition to the study of ma-made materials with at least one dimension between 1-100 nm [6]. In terms of medical research, nanomedicine is utilized to solve problems associated with delivery of lipophilic drugs, delivery of drugs through membranes, delivery of macromolecules, simultaneous delivery of multiple drugs, imaging, and real-time monitoring of *in vivo* effect [8].

Nanoparticle properties such as size, surface groups, and surface charge can be fine-tuned for the desired purpose. In addition, many nanoparticles are suited for imaging applications and hence for diagnosis. There is immense interest in developing a single particle for both the diagnosis and treatment of various illnesses such as cancer. However, there are many drawbacks to this approach. The complexity of synthesis would be challenging to say the least. In addition, quality control measurements for several steps will have to be developed. A single diagnostic particle containing therapeutic payload may lead to unnecessary exposure to false positive tissues. Considering these deficiencies, it may be advantageous to develop an integrated multi-particle system for diagnosis and treatment.

The use of nanoparticles lends many advantages to drug delivery [9]. Association of drug molecules with nanoparticles via conjugation, entrapment, or adsorbtion, improves drug solubility. Nanoparticles can assist with drug transport across barriers and selectively delivery drugs to target tissues. Because off-target deposition is minimized, lower doses of drug can be administered to patients. Other advantages include more favorable pharmacokinetics, enhanced drug stability in circulation, controlled drug release, overcome drug resistance, and deliver several active components.

Consequently, there is growing interest to develop drug delivery systems for the treatment of cancers. The most basic systems consist of a drug and a nanocarrier, which are macromolecular structures such as polymers, liposomes, dendrimers, and colloidal

nanoparticles (Fig. 4). Nanotechnology is a rapidly growing field and is predicted to have profound impact on the direction of future drug delivery research. The basic goal of these systems is to increase accumulation of drugs at the target site. One method for increasing bioavailability is to increase circulation half-life and enhance accumulation of macromolecules in solid tumors by the enhanced permeability and retention (EPR) effect. Researchers have come to classify EPR as a passive targeting approach. Further increase in drug accumulation in tumors is possible through active targeting, the use of ligands that recognize specific proteins on cancer cells or the faulty blood vessels associated with tumor growth [10].

Many of the same nanoparticle properties that are advantageous for drug delivery are also beneficial for imaging and diagnostic purposes. Nanoparticles have found a wide range for use as diagnostic devices in vitro and in vivo. Nanoparticles have typically been shown to improve contrast for different imaging modalities.

Cancer Type	Stage	Stage at Diagnosis (%)	5-year Survival Rate (%)
Lung & bronchus	Localized	15	54
	Regional	22	26
	Distant	57	4
Melanoma of the skin	Localized	84	96
	Regional	9	62
	Distant	4	16
Ovary	Localized	15	92
	Regional	18	72
	Distant	61	27

Table 1.1 Stage at diagnosis and 5-year survival for selected cancer types [3].

2 BACKGROUND AND SIGNIFICANCE

2.1 Diagnosis of Cancer

The first step in achieving improved outcomes in cancer patients is improved diagnostic procedures and methods. It is widely acceptable and shown that when cancer is detected at early stages, it is treatable if not curable. Patients treated at early stages often have much higher survival rates than those who received treatment once their cancer had progressed. One of the biggest challenges in diagnosis is the detection of metastases and micrometastases.

Diagnosis is usually achieved by imaging procedures, biomarker screening, palpitation, or blood screening. Each screening modality is severely restricted to certain types of cancers and even further restricted to progressive stages of cancer. Accepted biomarker screening is limited to prostate specific antigen for prostate cancer and monitoring of CA-125 levels for ovarian cancer. However, there is a high probability of false positives in each case. Physical screening including palpitation is only able to diagnose cancers that present at or near the surface of the body such as breast cancer and melanoma. Blood screening has proven very useful for the diagnosis and prognosis of blood cancers such as leukemias and lymphomas. Medical imaging procedures such as computed tomography (CT), X-ray, positron emission tomography (PET) and magnetic resonance

imaging (MRI) and are very commonly utilized in the clinical for the diagnosis and prognosis of multiple cancer types.

Each imaging modality has its strengths and limitations and they can be performed in combinations to gain additional detail of the anatomy. Of these procedures, MR imaging is often the preferred modality for its combination of cost efficacy and the non-invasive and non-ionizing nature of the procedure [11]. In addition, MRI provides anatomical images at high resolutions [12]. This makes MRI an attractive imaging modality for the detection of small tumors and metastases. Resolution of target structure or tissue can be enhanced by the use of MRI contrast agents [13]. Food and Drug Administration (FDA) approved MRI contrast agents include small molecule gadolinium chelates. However, potential of nephrogenic systemic fibrosis is a concern with these agents. In addition, these chelates diffuse throughout the body and their small size results in short circulation times and less than ideal accumulation at target tissues [14].

2.2 Chemotherapeutics for the Treatment of Cancer

Cancers are basically dysregulated versions of normal cells, with the same genetic materials and expressing the same proteins. Because of the extremely close similarities between cancer and normal cells, it is a herculean challenge to design a drug that exclusively targets cancer cells leaving normal cells unharmed. The most glaring difference between cancer and normal cells is the proliferation rate and thus conventional chemotherapeutics were designed to exploit this. However, many adverse

side effects still remain. A newer generation of drugs based on genetic findings of cancer has been developed. These so called molecularly targeted chemotherapeutic agents are highly specific for mutations found in cancers and have considerably decreased effect on normal cells.

Cisplatin is the platinum based chemotherapeutic agent used to treat a variety of cancers including non-small cell lung cancer, ovarian cancer, and testicular cancer. It is a small molecule drug with a chemical formula of $Pt(NH_3)_2Cl_2$ and has a formula weight of 300.05 (structure shown below).

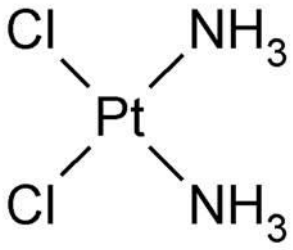

Chemical structure of cisplatin

Cisplatin is a non-specific drug that intercalates in DNA forming adducts. The chlorine atoms on the structure are displaced by hydroxyl groups and this intermediate species binds to DNA [15]. The most common complexes are instrastrand adducts between adjacent guanines (65%) and between adjacent adenine and guanine (25%). Less than 1% of adducts occur between strands. The formation of these adducts triggers programmed cell death process known as apoptosis.

Although efficacious during initial treatment, cancers typically relapse and are resistant to cisplatin therapy. The main resistance mechanisms include DNA repair through excision repair cross-complementing (ERCC) proteins or by anti-apoptosis mechanisms mediated by BCL2 protein.

Due to its non-specific nature, there are several toxicity concerns regarding cisplatin therapy. Renal toxicity is a major concern for which patients must receive additional hydration measures and must have serum electrolyte levels monitored. Cisplatin is also known to be highly emetogenic. Other toxicity concerns include myelosuppression, ototoxicity, and neurotoxicity.

Doxorubicin is another commonly used small molecule chemotherapeutic agent. It is classified as an anthracycline antibiotic. It has a similar mechanism of action as cisplatin in regards to DNA intercalation. However, doxorubicin is known to inhibit the topoisomerase II enzyme that unwinds DNA during replication. In the clinic, doxorubicin is used to treat a variety of cancers such as ovarian, lung, and breast cancers as well as different leukemias and lymphomas. It is available in a liposomal formulation, Doxil®, for the treatment of ovarian cancer, AIDS-related Kaposi's sarcoma, and multiple myeloma. Treatment with doxorubicin is limited by its lifetime cumulative cardiotoxic effects, which are possibly due to free radical generation from the quinone structure.

The chemical structure (shown below) consists of a four-member anthracene ring complex and an attached aglycone or sugar moiety. The anthracene complex acts as a

chromophore and gives doxorubicin its intense red color. Because of its chemical properties, doxorubicin is widely used in drug delivery research. The amine on the aglycone sugar moiety is typically used to conjugate doxorubicin to polymers. However, some studies have shown that the amine group resides in the minor groove of DNA and strengthens intercalation with DNA. This may explain the decrease in cytotoxic efficacy of doxorubicin conjugates. The inherent fluorescence can be utilized to quantify doxorubicin loading and release and monitoring *in vitro* distribution. The relatively higher water solubility is also attractive in performing many conjugation reactions.

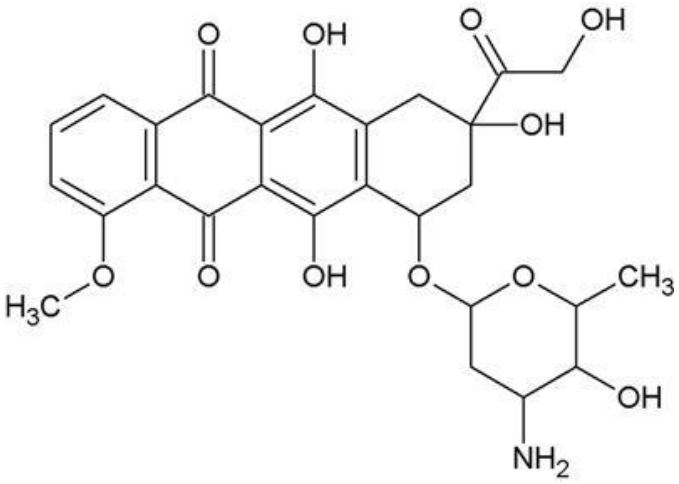

Chemical structure of doxorubicin

Melanoma is often curable at early cutaneous stages. Once the cancer has metastasized, the survivorship rate of patients is drastically lower [3]. In melanocytes, the Ras/Raf/MEK/ERK pathway is involved with growth, proliferation, and angiogenesis [16, 17]. It is responsive to numerous growth factors such as stem cell factor, fibroblast growth factor, and hepatocyte growth factor. It integrates signals from these cell

surface growth receptors and controls their gene expression via transcription factors. The pathway also has effect on the activities of proteins involved in apoptosis. The BRAF component of the pathway is the most common mutation and is found in 50-70% of melanomas. Glutamic acid for valine substitution at position 600 (V600E) accounts for the majority of BRAF mutations.

Vemurafenib is a novel drug for the treatment of melanoma [18]. Unlike cisplatin and doxorubicin, vemurafenib is considered a targeted drug. It exerts it effects primarily on cells with the V600E mutation. Therefore, it can be a more potent and safer medication for patients. Clinical trials have shown the overall response rate of 50% and these patients have regression of disease and prolonged survival [19]. Despite initial efficacy, patients may be plagued by secondary non-melanoma skin cancers or relapsing melanomas that are resistance to vemurafenib [20].

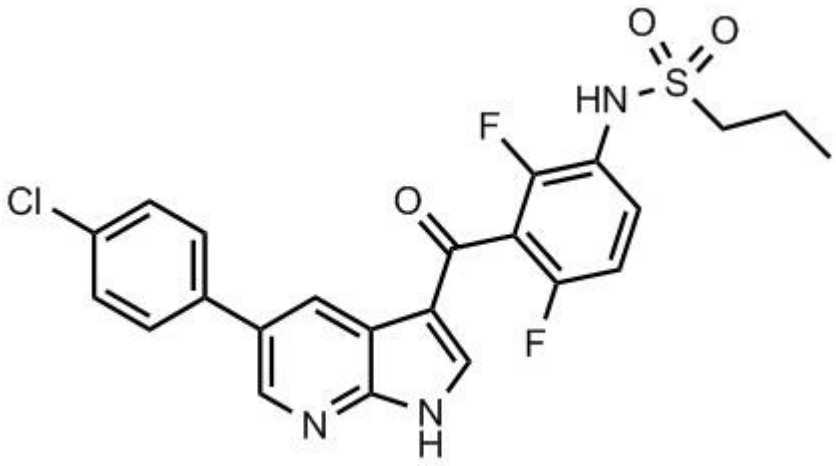

Chemical Structure of Vemurafenib

2.2.1 Limitations of Therapeutic Efficacy

Despite initial treatment success, cancers are notorious to relapse in more aggressive manifestations. Drug resistance mechanisms are up-regulated and present a major challenge to efficacious treatment. These mechanisms are present in normal cells to a lesser extent. They may have assisted in evolution to prevent toxicity from various xenobiotics. Drug mechanisms can be broadly classified into two groups: pump and non-pump resistance. Because both mechanisms may be present in most cancers, it may be necessary to target both forms of resistance [21].

Pump resistance is mediated by efflux proteins located on cellular membranes, particularly P-glycoproteins (P-gp) and multidrug resistance associated protein (MRP). These proteins are located in the cell membrane and are ATP-dependent. They are able to pump a variety of xenobiotics out of the cell cytoplasm against a concentration gradient. The aim with drug delivery using nanoparticles is to bypass these resistance proteins by internalization via endocytosis mechanisms [22].

Cancer cells have the capacity to develop various non-pump resistance mechanisms. One of the most common is BCL2 protein. It is plays a vital role in anti-apoptotic cell death after damage caused by anticancer agents (Pakunlu et al., 2006). Studies using siRNA have shown that knockdown of BCL2 expression can overcome drug resistance and improve efficacy of different anticancer agents.

To minimize patient discomfort and have high efficacy, chemotherapeutic drugs such as cisplatin and doxorubicin are administered in intervals at high doses. The doses can be increased to overcome resistance, but there will be a corresponding increase in adverse side effects. Nanotechnology offers an attractive method to overcome the numerous shortcomings of cancer chemotherapy. In regards to resistance, nanoparticle-drug conjugates can bypass efflux pumps such as P-glycoprotein. Delivery of siRNA using nanoparticle can suppress the expression of proteins involved in drug resistance. Nanoparticles tend to accumulate at tumor site passively due to enhanced permeation and retention effect. Attachment of targeting ligands can further increase tumor deposition of drug. Theoretically, lower doses of chemotherapy drugs can be administered to patients because there will be a decrease in off-target distribution, increase in tumor deposition, and potential to overcome resistance mechanisms.

2.3 siRNA as a Novel Treatment Modality

RNA interference (RNAi) has become a very popular tool in laboratory settings. Its usefulness in genetic related project lies in its inherent potency and specificity. The concept of RNAi is that the expression of a targeted gene can be suppressed by the external administration of double stranded RNA (dsRNA) containing a complementary strand termed antisense strand [23]. The antisense strand, possessing a complementary sequence to the messenger RNA strand of the targeted gene, would be able to base pair with it and prevent its translation. RNAi is used to generate cells, tissues, and animal

models with reduced or no expression of target genes [24]. In addition, knockdown of gene expression has allowed scientists to study function of the particular gene. Since a number of diseases and especially cancers result from overexpression of genes or expression of mutated genes, RNA interference (RNAi) provides a possible treatment modality.

Early studies in animal models involved the administration of dsRNA containing 200 or more nucleotides [25-28]. RNAi is related to post-transcriptional gene silencing observed in plants and fungi [29, 30]. Zamore et al. [31] demonstrated that the cellular machinery processed exogenous dsRNA into 21-23 nucleotide fragments and that these fragments act as guides for target mRNA degradation. The RNAi process utilizes many of the same proteins in the endogenous pathway involving gene expression using microRNAs. These findings spurred the creation of a new area of research seeking treatments for diseases with a genetic underpinning that were thought to be incurable at one time.

Based on the finding that exogenous dsRNA was processed into short fragments, Elbashir et al. [23] were the first group to show the suppression efficacy of synthesized dsRNA containing 21 or 22 nucleotides and that overhanging nucleotides on the 3' end help with RNA interference. The cleavage site could be moved by changing the sequence of the antisense strand to complement other mRNA sequence by having as little as a

two nucleotide shift. The new short dsRNA construct was termed short interfering RNA (siRNA) and provided the foundation for future research in the field.

Fig. 2.1 shows the overview of the RNAi process. The first step is the transfection of siRNA or dsRNA into the cell. The primary advantage of delivering siRNA over longer dsRNA is that dsRNA must be cleaved into shorter 21-22 nucleotide fragments by Dicer, RNAase III family nuclease. Once in the cytoplasm, siRNA undergoes phosphorylation of the 5' ends [32]. The sense and antisense strands are unwound and associate with a protein complex termed RNA induced silencing complex (RISC). The RISC separates the sense strand from the antisense strand. The antisense strand which is complementary to the mRNA sequence of the target gene is retained in the complex and guides the RISC to the target sequence. Based on the 5' end of the antisense strand, there is a single cleavage site of the target mRNA sequence leading to mRNA degradation.

Due to its nucleic acid structure and anionic charge, siRNA cannot be used as a form of therapy in of itself. Systemic administration of siRNA or any other nucleic acid will result in rapid degradation and a half-life of approximately one hour owing to the presence of nucleases in the plasma [33]. There has been research to increase the plasma stability of siRNA molecules [34]. Most of these techniques involve modifications to the phosphodiester backbone; however, their relatively small size can lead to urinary clearance and short residence time in plasma [33]. Even localized delivery of siRNA will be a challenge. Similar to plasmids used for gene therapy, internalization of siRNA by

cells is inefficient. Cell membranes are known to possess a negative charge and can electrostatically prevent siRNA internalization. Therefore, it is necessary to use a vector to deliver siRNA into the cytoplasm. Even when internalized, siRNA lacks the inherent capability to escape from the endosomal compartment and into the cytoplasm [35].

2.3.1 siRNA vs. DNA Nanoparticle-Based Delivery

Compared to gene delivery, siRNA therapy is a much more novel pursuit. Although there are numerous similarities between siRNA and plasmid DNA, there are also important differences that can affect selection and formulation of a nanoparticle-based delivery system.

Plasmid DNA molecules are typically several kilobases in length. The persistence length, the maximum length at which chains behave as rigid rods, can be calculated for double stranded DNA (dsDNA) and double stranded RNA (dsRNA). For dsDNA, the persistence length is 50 nm or 185 base pairs whereas for dsRNA, the persistence length is longer at 70 nm or 260 base pairs [36-39]. As is evident, plasmid DNA molecules are well over the persistence length for dsDNA and therefore have tremendous flexibility allowing for compact condensation into nanometer sized particles. Based on these calculations, siRNA, which are usually 21 base pairs, can be predicted to behave as rigid rods. Large complexes or poorly condensed siRNA complexes may be the result depending on the siRNA to polymer ratio [40]. siRNA containing particle complexes larger than 150 nm fail to enter cells via clathrin-coated pits and there is no gene silencing [41, 42].

siRNA-mediated gene knockdown in rapidly dividing cells such as cancer cells has a durational effect lasting between three and seven days [43]. In slowly dividing cells, the effects may last 3 weeks, which the natural degradation rate of siRNA [43, 44]. The shorter time in rapidly dividing cells may also be due to concentration dilution with each occurrence of cellular division.

Vectors have been extensively studied for gene therapy. Despite some differences, design of a vector for siRNA delivery can build off of the knowledge acquired from gene therapy studies. Therapy suing siRNA has several advantages and distinctions from gene therapy. Whereas gene therapy is used to induce expression of a gene, the aim of siRNA therapy is to suppress the expression of a particular gene expressed endogenously. Typically plasmid DNA molecules are used for gene therapy and contain several kilobases [45]. siRNA molecules on the other hand contain approximately 21-23 base pairs. Although the smaller size allows for easier and chemical synthesis, packaging of siRNA into nanoparticles (condensation) may arise. Because the persistence length (length over which chains act as rigid rods) for double stranded RNA is 70 nm or 260 base pairs, siRNA molecules can be expected to have rod-like properties [38, 39]. Therefore, vectors used for the delivery of plasmid DNA may not necessarily be the best for siRNA delivery. The primary advantages of siRNA are that the siRNA only has to enter the cytoplasm to exert its effect and there is no long term inhibition. Plasmid DNA must be delivered into the nucleus and integrate with the endogenous genome. The possible long term incorporation and expression may lead to toxic effects.

Most commonly used vectors are nonviral cationic vectors. In addition to protecting siRNA from the environment, these vectors endow the particles with a net positive charge that aids in cellular internalization. The primary advantage of non-viral vectors over their viral counterparts is minimization of immune recognition and response. Lipofectamine is the most commonly used vector in laboratory settings. It is a positively charge lipid. Although the transfection is high with Lipofectamine, it appears to be useful for only certain cell lines and there are numerous concerns regarding its safety in animals [46-49]. There are numerous publications evaluating various non-viral carriers for the delivery of siRNA including liposomes [50], polymers [51, 52], and metallic nanoparticles [53].

2.4 Nanoparticles as Multifunctional Tools

Nanoparticles can be designed to be like Swiss army knives in respect to their multifunctional capabilities. They can deliver multiple therapeutic payloads, can be combined to deliver a therapeutic payload and also used for imaging, or different imaging modalities can be synthesized into a single nanoparticle. When used for combined diagnostic and therapeutic purposes, nanoparticles can be termed theragnostic (theranostics) particles [54].

2.5 Nanoparticle Systems for Therapy

Nanoparticles are an attractive method for the delivery drugs, nucleic acids, peptides, and other cargoes. Their popularity is due in part to their customization properties. Properties such as size, shape, surface charge, composition, and surface functional groups can be tailored to meet almost any need.

The majority of clinically used drugs are small molecules. When administered to a patient, only a small portion of the dose reaches the target site. To compensate, a patient receives a large dose to achieve therapeutic efficacy. However, drug deposition in other tissues causes adverse side effects. This is a concern especially for chemotherapeutic drugs. Small molecule drugs can be entrapped within the matrix or conjugated or adsorbed onto the surface of nanoparticles. The goal is to increase drug concentrations at target organs and tissues and minimize drug localization in other sites. The potential for delivering small doses is possible as well.

The most common nanoparticles for drug delivery purposes are polymers, liposomes, antibodies, and inorganic nanocrystals (Fig. 2.2). These carriers have high molecular weights and can be loaded with multiple drug molecules. The bulky structure endows improved pharmacokinetics, enhanced drug stability in circulation, controlled release, overcome drug resistance, ability to deliver several anti-cancer drugs and other active components, and targeted delivery.

The delivery of low molecular weight anticancer drugs and siRNA by macromolecular carriers offers several advantages including more favorable pharmacokinetics, enhanced stability during its journey in the systemic circulation, controlled release, possibility to overcome drug resistance, ability to deliver several anti-cancer drugs and other active components, targeted delivery specifically to cancer cells, etc. Consequently, there is growing interest to develop drug delivery systems for the treatment of cancers. The most basic systems consist of a drug and a nanocarrier, which are macromolecular structures such as polymers, liposomes, dendrimers, and colloidal nanoparticles (Fig. 4). Nanotechnology is a rapidly growing field and is predicted to have profound impact on the direction of future drug delivery research. The basic goal of these systems is to increase accumulation of drugs at the target site. One method for increasing bioavailability is to increase circulation half-life and enhance accumulation of macromolecules in solid tumors by the enhanced permeability and retention (EPR) effect, a passive targeting approach. Further increase in drug accumulation in tumors is possible through active targeting, the use of ligands that recognize specific proteins on cancer cells or the faulty blood vessels associated with tumor growth [10].

2.5.1 Dendrimers

Polymers are perhaps the most well studied drug delivery carriers. Most polymers such as HPMA, PLGA, PLL, and PLA are linear polymers. Drugs can be chemically conjugated onto polymer side chains or termini or encapsulated in the matrix when the linear

polymers form condensed particles. However, the drug loading capacity per volume is quite limited.

Dendrimers are a newer class of polymers that have a three-dimensional shape [55]. The structure can be sub-divided into different regions: core; interior branches, internal cavity, and terminal groups (Fig. 2.3). Lower generation dendrimers have a more open and asymmetric structure. Dendrimers of fourth generation and higher possess a globular structure with internal cavities with a close membrane of functional groups. Because of their structure, the drug loading density is much higher than that of linear polymers. Molecules can be chemically conjugated or adsorbed onto the surface of dendrimers. The internal branches can be designed to be hydrophobic whereby lipophilic molecules can reside within the dendrimer interior.

Dendrimer conformation can change based on the pH [56]. Amino-terminated PAMAM and PPI dendrimers have basic surface groups and interiors. In the presence of a low pH ($pH \leq 4$) environment, interior tertiary amines are charged and the dendrimer has extended conformation. At neutral pH, backfolding occurs due to hydrogen bonding between the internal tertiary amines and surface primary amines. At $pH \geq 10$, the dendrimer has overall neutral charge and a resulting globular structure. These structural dynamics can be used for various applications such as loading or release in response to environmental pH changes.

Synthesis of dendrimers has a higher level of control than that of linear polymers and yields monodisperse polymers in regards to size and mass. Dendrimers can be constructed by two different methods: divergent or convergent. In the divergent method, the core is the starting point and growth is outward. Common dendrimers such as the poly(amido amine) (PAMAM) and polypropylenimine (PPI) dendrimers are produced at large scales using divergent methods. In the convergent method, synthesis begins with the terminal groups and converges to form polymeric arms or dendrons. Once the desired dendron size is reached, they are attached onto a core. The convergent method is ideal for synthesizing asymmetric dendrimers.

Dendrimers have various other properties that are advantageous for chemical reactions [55]. They are less viscous than linear polymers and have a better rheological profile due their packed ball conformation in solution. The viscosity increases with generation until typically the fourth generation and then begins to decrease. Linear polymers, in contrast to dendrimers, have a flexible coil confirmation in solution and viscosity increases with molecular weight. The tight ball packing and presence of surface functional groups allows dendrimers to be highly soluble in aqueous mediums for chemical reactions.

Along with PAMAM dendrimers, PPI dendrimers are the most widely utilized for drug and nucleic acid delivery. The PPI dendrimer core is a diaminobutane molecule and is built using tertiary propylene amines [57]. The terminal groups are typically primary amines, which are positively charged on neutral pH conditions and can be used to

electrostatically bind to nucleic acids [52, 53, 58]. PPI dendrimers with quaternary amines have been studied as gene delivery vectors as well [59].

Various studies have demonstrated that the different molecular weights of polymers affect transfection efficiency and cytotoxicity [45, 60, 61]. Cationic dendrimers like other cationic polymers (Poly-L-Lysine and polyethylenimine) have also been shown to be cytotoxic and hemolytic; therefore, it is necessary to use the smallest amount possible [62]. Strategies such as PEGylation of dendrimer structures may help to alleviate some of these toxicity concerns [52]. Another group showed that amino acid or carbohydrate functionalized generation 5 PPI (PPI G5) dendrimers had improved biocompatibility profiles compared to non-functionalized PPI G5 [63].

2.5.2 Lipid Nanoparticles

Polymers, liposomes, emulsions, and inorganic nanoparticles have been extensively studied for small molecule delivery. Solid lipid nanoparticles (SLNs) and nanostructured lipid carriers (NLCs) are more recent nanoparticle formulations that appear to have several advantages. SLNs are composed of lipids that are solid at room and body temperatures [64, 65]. Simply, the liquid lipid used in emulsions is replaced with solid lipid to form SLNs. They are usually 50-1000 nm in size and can be composed of lipid acids, mono-, di-, or tri-glycerides, or waxes [66]. In comparison, NLCs are formulated by mixing solid and liquid lipids, which are spatially different. Small molecules are entrapped between chains of fatty acids or as clusters in imperfections of the SLN

matrix. However, the use of highly pure lipids for formulation of SLNs results in low energetic, perfect crystalline form that limits drug loading and leads to drug expulsion. The combination of different lipids as in NLC formulations causes more imperfections in the matrix and results in high drug loading capacity and reduced drug expulsion. Drug release from SLNs follows a biphasic fashion; an initial burst release is followed by a slow release of drug [67].

The safety profile of SLNs and NLCs are very good because they are composed of lipids that meet Generally Recognized as Safe (GRAS) status and formulation does not require use of organic solvents [65]. Protection of lipophilic drugs is superior because molecules are incorporated in the matrix and there is prolonged release of drug.

The most potent chemotherapeutic agents being developed tend to have very poor solubility in aqueous mediums; therefore, entrapment in a lipid-based carrier is quite attractive. Emulsions and liposomes are produced using well-known excipients and at large scales, but these systems offer weak drug protection and cannot control the release of drug [64]. These two problems can be overcome using SLNs and NLCs. The liquid lipid in NLC formulation is entrapped in the voids of solid lipid crystals, but appears not to affect the overall structure [65, 68, 69]. Lipophilic drugs solubilize in the liquid lipid portion and thus entrapped within the crystal matrix. The result is higher drug loading and sustained drug release from the carrier [65, 69]. A study comparing SLNs and NLCs using clotrimazole, an antifungal agent, as a model drug demonstrated

that NLCs had better stability at high drug loading and there was no change in drug release profile after storage [65]. Chemotherapeutic agents can have serious adverse side effect profiles and entrapment in NLCs can reduce the amount of free drug in the plasma and off-target sites. The liquid and solid lipid compositions can be modified to achieve no drug release in circulation. The controllability of particle size can aid in accumulation in solid tumor tissue by active enhanced permeation and retention (EPR) effect. Lipid-PEG molecules can also be incorporated into the formulation to improve water solubility and introduce surface functional groups for attachment of targeting moieties. Other biocompatible surfactants and emulsifiers can be used to improve water solubility [66].

2.6 Nanoparticles for Diagnosis

Anatomical imaging procedures are an attractive modality because of the relatively fast results and relatively non-invasive nature. Most contrast agents for imaging purposes are small molecules or chelates. These agents tend to be rapidly cleared from systemic circulation. The short half-lives do not result in optimal accumulation in target tissues and there exists a propensity for off-target tissue uptake [14].

Imaging modalities can be classified as deep or shallow tissue modalities [70]. Shallow tissue imaging uses optical or fluorescence techniques, but is limited to structures up to two millimeters in depth. Magnetic resonance imaging (MRI), computed tomography (CT), and positron emission tomography (PET) are considered to be deep tissue

modalities. Biological active molecules and metal chelates are often used for PET imaging, but they do not meet the criteria to be called nanoparticles. MRI is an excellent imaging modality for assessing soft tissues. Magnetic nanoparticles, iron oxide nanoparticles and more recently manganese oxide nanoparticles are widely used for MR imaging studies [71]. These particles work by altering relaxation rates of water protons in tissues. Free ions tend to higher effects than bulk ions as found in nanoparticles. Therefore, it is necessary to have some interaction between water protons and the metal ions. These free ions tend to have toxic effects even at small doses; therefore, nanoparticle formulations may be a safer alternative. Unlike nanoparticles for other modalities, the contrast is a result of the nanoparticle effect and not the nanoparticle itself [14]. X-ray radiation is used to construct three dimensional images for CT imaging. Gold nanoparticles have great potential to be a CT contrast agent to help attenuate X-rays in soft tissues and they have also been studied for shallow tissue imaging [71]. Contrast agents have the strongest effect on PET imaging followed by MRI and then CT imaging [72].

Nanoparticles are attractive for both in vivo and in vitro diagnosis. They can be administered to a patient and used as an imaging agent. In respect to in vitro diagnostics, nanoparticles can be modified to attach and react with biomarkers of interest. For diagnostic purposes, nanoparticle systems should aim to have a circulation half-life of two to six hours to allow for adequate tumor deposition [73]. Longer half-lives may be necessary for nanoparticles with therapeutic payloads. There are many

studies demonstrating synthesis of multimodal imaging agents by either combining of different nanoparticles into a single carrier [74], modifying nanoparticles with optical dyes [75], or incorporating different nanoparticles into a single nanoparticle [76, 77].

Organic nanoparticles such as liposomes, micelles, and polymers have been studied for use as contrast agent. Because of the absence of any inherent contrast, these nanoparticles are simply vessels for inorganic nanoparticles, chelates, and organic dyes [70]. Inorganic nanoparticles (quantum dots, iron oxide nanoparticles, manganese oxide nanoparticles, and gold nanoparticles) are extensively studied for their imaging capabilities. Not only can nanoparticles provide traditional imaging, they can be utilized for molecular imaging to identify particular biomarkers and pathways. Bulk properties of nanoparticles can increase their overall contrast capabilities in comparison to conventional agents, which are small molecules or metal chelates.

Inorganic nanoparticles are also referred to as nanocrystals due to the crystal structures of metal ions with their counterpart ions. The size and shape of the nanocrystal is dependent on reaction conditions. Spherical shapes are most widely sought, but some applications may benefit from other shapes such as rods.

Nanoparticles have been extensively studied as imaging agents for magnetic resonance imaging (MRI) [11, 53, 78-80], positron emission tomography (PET) [81], computed tomography (CT) [82, 83], and optical imaging. The customizable properties of nanoparticles also allows for combination of imaging modalities in a single nanoparticle

[84, 85]. The bigger size of nanoparticles and the potential of PEGylation results in circulation times up to several hours to days. The properties can be fine-tuned to achieve an appropriate circulation time for the intended purpose and clearance to avoid adverse side effects. Most nanoparticles used as imaging probes are metal oxides whose cores must be synthesized at high temperatures and in inert atmospheres [86]. There is increasing research to develop less energy intensive methods for the synthesis of imaging nanoparticles. There are some toxicity concerns with metal oxide nanoparticles due to the presence of heavy metals. Researchers are also developing nanoparticles using different materials to offset this concern.

2.6.1 Quantum Dots

Quantum dots are the most widely studied nanoparticles for optical imaging particularly due to their inherent fluorescent capability [71]. Their higher photostability is an improvement over conventional dyes. They are typically composed of a core of a semiconductor metal from groups II to V in the periodic table such as cadmium selenide capped with a shell of a semiconductor metal of wider band gap. Due to toxicity concerns with regard to the presence of cadmium, there is active research in utilization of other materials. Indium phosphide quantum dots have been constructed to help alleviate some of toxicity concerns [87]. These quantum dots have emission maxima in the near infrared region allowing for in vivo imaging. The majority of the studies demonstrating quantum dot toxicity were performed using only the cadmium selenide

cores. Capping with a shell and functionalization with polymer coating immensely reduces the exposure of the core and consequently there is little to no toxic effects [88]. However, the vast majority of these quantum dots possess properties that are considered sub-optimal compared to quantum dots composed of a cadmium-containing core. Quantum dots have many advantages over traditional fluorescent dyes: quantum dots have a wideband excitation, narrow emission, long photostability, high quantum yield, single quantum dot sensitivity, and potential for multicolor imaging using a single light source [89, 90]. Quantum dots have attracted attention for use in applications such as biosensors, bioanalytical assays, cell imaging, and in vivo animal targeting [90].

Hydrophobic quantum dots must be coated with amphiphilic polymers (Fig. 5) to be dispersed in aqueous solution and used in biological applications [91]. The surface coating may affect the biological and physical properties of quantum dots including the overall dimensions. Biomolecules such as antibodies and oligonucleotides can be attached to these hydrophilic coated quantum dots using standard conjugation protocols. Studies have shown the retention of biomolecule activity of anti-cancer drugs after conjugation to quantum dots. It is highly possible for a slight decrease in binding affinity of conjugated biomolecules to their targets [91].

Fluorescence labeling is an integral part of many biological assays such as cellular labeling and tissue imaging [92]. Therefore, it is of no surprise that quantum dots have gained popularity in this field. Conventional fluorophores consisting of organic dyes,

fluorescent proteins and polymers, and other small molecules have numerous inherent inadequacies. Conventional fluorophores are also subject to having low quantum yields, pH sensitivity, and high susceptibility to chemical degradation and photo-oxidation. These inherent flaws erect barriers from achieving optimal fluorescence images and increase the propensity of not discovering minute details. Narrow excitation wavelength range and broad emission peaks are characteristic of almost all conventional fluorophores and as a result leads to difficulty in setting parameters to minimize unwanted excitations and misinterpretations due to overlapping spectra. Quantum dots overcome these deficiencies because they have superior photostability and brightness, have similar emission wavelengths as conventional dyes, the emission wavelength can be fine-tuned, and they have a wide excitation peak allowing for multicolor emission using a single excitation wavelength [70]. Quantum dots with diameters about 2 nm have a blue fluorescence (380 to 440 nm) and as the size increases to 5 nm, the fluorescence shifts to red emission (605 to 630 nm) [93, 94].

Broad overlap between donor and acceptor absorbance/emission spectra and direct excitation of acceptor complicate results. The phenomenon of Förster Resonance Energy Transfer (FRET) has enabled scientist to study interactions and mechanisms of subcellular structures and processes including interactions between proteins, ligand-receptor binding, and changes in molecules due to environmental changes [95]. Although optical imaging works well for small animals, its utilization has not transferred into the clinic and is not ideal for imaging of deeper anatomical structures.

Although widely used as fluorescence probes, quantum dots will have the biggest impact in the field of drug delivery. There is increasing interested to combine various aspects such as imaging, diagnostics, and treatment into one delivery vehicles. Based on their properties, quantum dots are the ideal candidate.

Functionalized QD are versatile and can be modified with biomolecules such as antibodies, small molecules, peptides, and aptamers [91, 96]. Due to these properties, QD can be utilized to design multifunctional systems for simultaneous imaging and delivery of therapeutic agents, a task that represents a substantial challenge for other types of nanocarriers. Recent reports showed that QD can be used in photodynamic and radiation therapy [97], which would make QD a prospective therapeutic drug carrier since radiation therapy is employed as an adjunct for the treatment of many types of cancers. In addition, quenching of fluorescence of QD by a cargo due to FRET would allow for monitoring the attachment and release of QD payload.

2.6.2 Superparamagnetic Iron Nanoparticles

Superparamagnetic iron oxide nanoparticles (SPIONs) are the most widely studied nanoparticle MRI contrast agent. They are primarily used as T2 MRI contrast agents, which produce negative or dark contrast [14]. However, they can also possess T1 or brightening contrast effects. The general rule is that smaller SPIONs have greater brightening effect and that negative contrast effect increases with size of SPIONs. Several iron based contrast agents have entered the clinic, primarily for live, spleen, and

bone marrow imaging. However, optimal utilization of SPIONs is hindered by their propensity to induce image artifacts [98].

The unique feature of superparamagnetism exhibited by SPIONs is advantageous in biological environments. SPIONs are magnetic or active only in the presence of an external magnetic field and revert back to a non-magnetic state when the magnetic field is removed [99]. SPIONs can be used for hyperthermia therapy of cancer. Hyperthermia results in direct tumor killing at temperatures in the range of 41-42˚C [100]. The use of SPIONs helps to localize the increase in temperature [101]. Reports of using iron oxide in tumor killing by hyperthermia date back to 1957 [102]. In an alternating magnetic field, the reorientation of the nanoparticles results in heat production. The small of SPIONs allows for the use of tolerable external magnetic fields whereby tissues that have not accumulated SPIONs will remain unharmed. SPIONs have also been studied for delivery of chemotherapeutics [103]. The system was designed to have triggered release of doxorubicin in response to increased temperature (40˚C) and lower pH. Hyperthermia induced by SPIONs has potential to increase efficacy of drugs by synergistic means (hyperthermia and mechanism of action of the drug), hyperthermia-induced bond breaking, and enhanced permeability due to increased temperatures [104].

2.6.3 Manganese Oxide Nanoparticles

Manganese oxide nanoparticles are a novel alternative to SPIONs. They have some advantages over SPIONs: they are positive contrast agents and they do not induce

imaging artifacts. Like SPIONs, the metal oxide core is not water soluble and must be coated with amphilic or hydrophilic polymers. The most common coating are silica shells [12, 13] and coating with lipid-PEG molecules [105, 106].

In the form of nanoparticles, manganese atoms have little contact with water and therefore bulk arrangement of atoms as in nanoparticles have low molar relaxivities and result in low positive contrast [78]. When Mn^{2+} ions are liberated (possibly in the low pH endosomal environment) from the bulk nanocrystal structure, the molar relaxivity may increase 10-fold. The synthesis of porous manganese nanoparticles may increase their contrast capability [98].

Manganese oxide nanoaprticles share many of the features of SPIONs such as surface functionalization to attach targeting moieties and drugs. It is likely that manganese oxide nanoparticles will attain as much popularity as SPIONs.

2.7 Cancer Targeting

In regards to nanocarriers, there is great debate concerning the usefulness and necessity of the incorporation of targeting moieties to increase bioavailability at the site of action. Conjugation of a targeting moiety adds another step in the synthesis and purification processes as well as another parameter for quality assurance. This type of targeting, generally qualified as an active targeting, is more effective when compared with passive targeting of nanocarriers by the EPR effect. Currently approved

nanomedicines for cancer treatment, Doxil and Abraxane, do not have targeting ligands. Reports of the benefits of targeting ligands have had mixed results. Although it appears that accumulation within the tumor environment is identical for targeted and non-targeted carriers, the cellular uptake of targeted carriers and cytotoxicity of drugs delivered by these carriers are more pronounced [8, 107]. Binding of a targeting ligand to a membrane receptor can result in receptor-mediated endocytosis and therefore increased cellular internalization.

Compared to free drug in vitro, polymer-drug conjugates (non-targeted and targeted) were shown to be less cytotoxic [108]. However, the targeted polymer-drug formulation had higher toxicity profiles than their non-targeted counterparts. Antitumor activity experiments demonstrated a slight disharmony in corroboration with in vitro results. Polymer-drug conjugates (both non-targeted and targeted) were able to reduce tumor size whereas there was a slight increase in tumor volume when mice received free drug. Targeted polymer-drug conjugates had higher antitumor effects than non-targeted conjugates. An increase in this effect was seen with increasing number of targeting moieties.

2.7.1 Luteinizing Hormone-Releasing Hormone

Luteinizing hormone-releasing hormone (LHRH), also called gonadotropin-releasing hormone, is a decapeptide secreted by the hypothalamus. It binds to corresponding LHRH receptors on the pituitary and induces the release of luteinizing

hormone and follicle-stimulating hormone [109, 110]. Levels of the LHRH receptor are highest in the pituitary, but some amounts are found in peripheral organs such as the breasts, prostate, and kidneys. Increased expression of high affinity binding sites for LHRH is found in approximately 50% of breast cancers and 80% of ovarian cancers. Extrapituitary LHRH receptors play role in growth and proliferation in an autocrine/paracrine loop fashion. Because of the proliferation on certain cancers and very little expression on visceral organs, LHRH receptor is an enticing target. Analogs of LHRH (GnRH) peptide are widely used as hormone therapy for the treatment of prostate cancer [111]. Patients receiving these analogs initially experience a surge in symptoms followed a precipitous decline in testosterone levels through negative feedback mechanisms. LHRH decapeptide has also been used as a targeting moiety by conjugation to doxorubicin [112] or attached to the surface of nanoparticles [113-115].

2.7.2 Mucin Proteins

Mucins are large O-glycosylated type 1 transmembrane proteins that form molecular barriers at epithelial surfaces of respiratory, gastrointestinal, and reproductive tracts and engage in morphogenetic signal transduction. Mucins are critical components for a cell's ability to maintain homeostasis and survive in environments with great variations in pH, ionic concentration, hydration, and oxygenation. Recent reports have suggested expanded roles of mucin proteins in cellular functions and the development of cancers. Mucins function as cell-surface

receptors which ultimately lead to their involvement in many cell-associated events such as proliferation, differentiation, apoptosis, and secretion [116, 117].

There is a growing population of studies demonstrating aberrant glycosylation pattern and over-expression of mucin receptors in some cancer types, especially adenocarcinomas. It is hypothesized that mucins are necessary for the modification of the local tumor environment during invasion, metastasis, and growth [116]. Reports have also demonstrated involvement of mucins in signal transduction pathways [116, 117]. The overexpression of aberrant forms of mucin proteins in various epithelial cancers has generated interest in studying mucin proteins as targets for the drug delivery. There are numerous studies concerning the use of monoclonal antibody (MAb) C595 as a possible therapeutic agent with anti-MUC1 activity. One approach has conjugated radioisotopes to C595 for targeted alpha therapy of pancreatic, prostate, breast, and ovarian cancers [118].

Mucin 1 (MUC1) is a member of cell-surface mucin family. MUC1 is a heterodimer whose NH2-terminal subunit contains a variable number of twenty amino acid tandem repeat subject to O-glycosylations. The MUC1 cytoplasmic tail engages in several signal transduction pathways including Ras, β- catenin, p53, EGFR, and estrogen receptor α [117, 119]. Due to the involvement in these pathways, especially interaction in the EGFR pathway, it is no surprise that a specific fragment of the MUC1 protein has been implicated to act as a receptor to induce growth of human pluripotent stem cells.

Another study has linked MUC1 as a binding partner for ErbB1 receptor [120]. ErbB1 is a tyrosine kinase that is mutated and overexpressed in cancers. MUC1 binding prevents ErbB1 degradation and increases the recycling of the receptor; therefore, the levels of ErbB1 increase over time. This provides another possible mechanism of involvement of MUC1 receptor in cancer development and as a possible target for cancer chemotherapy.

Results of a study conducted by Wang et al. [119] showed that the MUC1 cell surface protein was overexpressed in over ninety percent of cases involving primary epithelial ovarian cancer and matched metastatic lesions, but immunoreactivity was absent in normal ovarian tissue. There is a correlation between level of expression of MUC1 and progression of ovarian cancer [119]. A recent study by Khodarev et al. [121] demonstrated that MUC1 regulated genes controlling tumorigenesis, cell motility, metastasis, and angiogenesis.

Ferreira et al. [122] have developed DNA aptamers targeting MUC1 receptor (Fig. 2.4). The aptamer consists of a twenty-five nucleotide sequence and possesses high affinity for the MUC1 receptor. The aptamer forms a stable complex with MUC1 and is not easily displaced by C595 antibody, which is specific for the MUC1 receptor. Aptamers provide several advantages over antibodies such as higher binding affinity, high specificity, highly selectivity for mutated epitopes, reduced immunogenicity, and increased tumor penetration.

A recent study found that the MUC1 is cleaved on the surface of most cancers, leaving a low molecular weight transmembrane domain, MUC1* [123]. MUC1* contains only forty-five amino acid sequence in the extracellular domain. This cleavage product is sufficient to for oncogenesis. It is unknown if the aptamer will exhibit binding properties to the cleavage product.

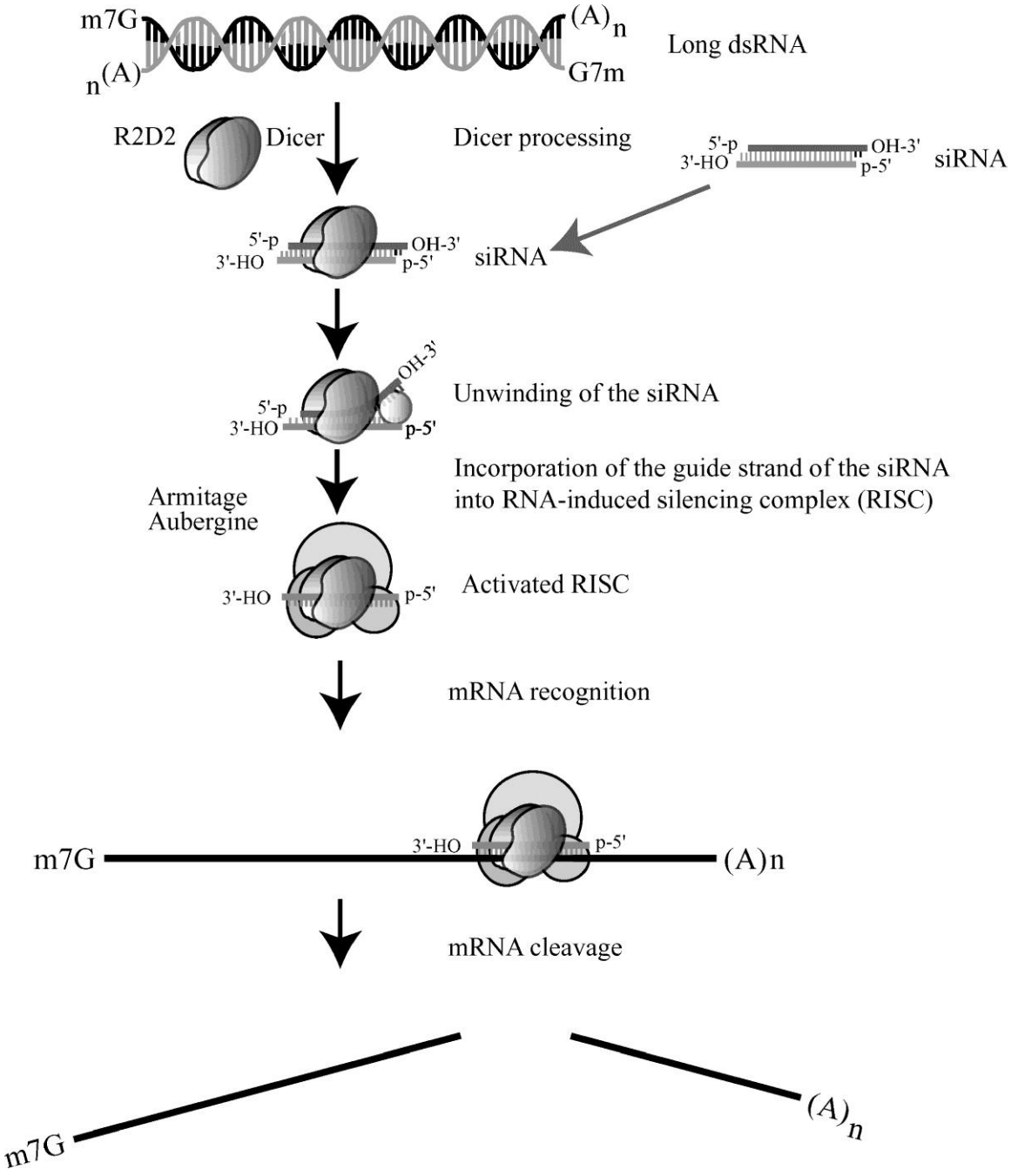

Figure 2.1 Mechanism of gene silencing (Reproduced from Ref. [33]).

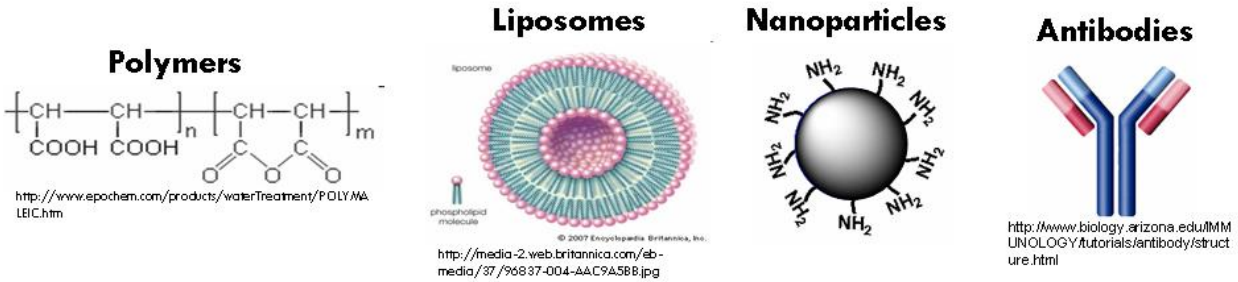

Figure 2.2 Nanoparticle carriers.

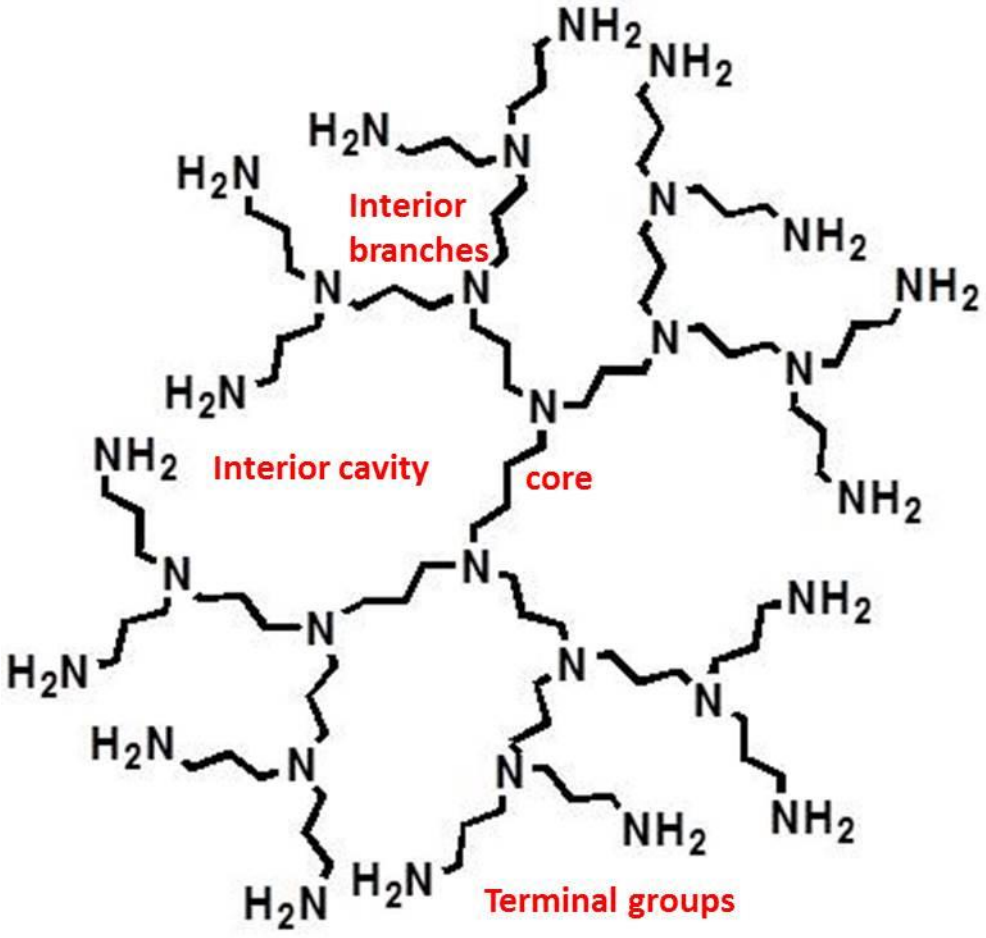

Figure 2.3 Structure of PPI G3 with labeled regions: core; interior branches; interior cavity; and terminal groups.

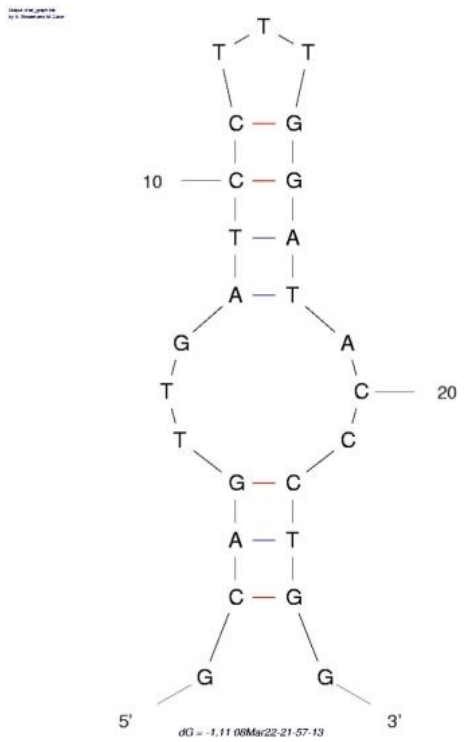

Figure 2.4 Structure of DNA aptamer targeted for MUC1 surface protein. Structure with internal base pairing predicted using mfold software [122, 124].

3 SPECIFIC AIMS

Specific Aim 1: To study siRNA condensation by different generations of cationic PPI dendrimers

The goal of the present investigation is to reveal the role of the Poly(propyleneimine) (PPI) dendrimer structure on the siRNA nanoparticles formation, facilitation of cell internalization, and sequence specific knockdown of targeted genes. It was found that the higher generations of PPI dendrimers (G4 and G5) most effectively initiated the complexation of siRNA into discrete nanoparticles when compared with lower generations of dendrimers (G2 and G3) as determined by tapping mode atomic force microscopy and dynamic light scattering. The formulated siRNA-PPI complexes provided for a dramatic enhancement in siRNA cellular internalization and marked knockdown of targeted mRNA expression in A549 human lung cancer cells. While the size and positive charge density of G5 is much larger than G4 dendrimers, provoking higher toxicity, G4 dendrimer shows the maximum efficacy terms of siRNA nanoparticles formation, intracellular siRNA internalization, and sequence specific gene silencing.

Specific Aim 2: To evaluate siRNA delivery using cooperative condensation agents, PPI G5 dendrimer and SPIO nanoparticle to overcome drug resistance

The ability of Superparamagnetic Iron Oxide (SPIO) nanoparticles and Poly(Propyleneimine) generation 5 dendrimers (PPI G5) to cooperatively provoke siRNA

complexation was investigated in order to develop a targeted, multifunctional siRNA delivery system for cancer therapy. Poly(ethylene glycol) (PEG) coating and cancer specific targeting moiety (LHRH peptide) have been incorporated into SPIO-PPI G5-siRNA complexes to enhance serum stability and selective internalization by cancer cells. Such a modification of siRNA nanoparticles enhanced its internalization into cancer cells and increased the efficiency of targeted gene suppression in vitro. Moreover, the developed siRNA delivery system was capable of sufficiently enhancing in vivo antitumor activity of an anticancer drug (cisplatin). The proposed approach demonstrates potential for the creation of targeted multifunctional nanomedicine platforms with the ability to deliver therapeutic siRNA specifically to cancer cells in order to prevent severe adverse side effects on healthy tissues and in situ monitoring of the therapeutic outcome using clinically relevant imaging techniques.

Specific Aim 3: To develop a mucin receptor-targeted quantum dot-based doxorubicin delivery system

The third aim is devoted to the development of drug delivery system for the chemotherapeutic agent, doxorubicin. I designed and synthesized a novel nanoparticle-based drug delivery system consisting of a tumor-targeted, pH- responsive Quantum Dot-Mucin1 aptamer-Doxorubicin conjugate for combined imaging and chemotherapy. A DNA aptamer specific to over-expressed Mucin 1 receptors was used for targeting to maximize accumulation in cancer cells and minimize systemic exposure and adverse side

effects. In addition, doxorubicin was attached using an acid-labile hydrazone bond, which is stable in plasma and rapidly hydrolyzes in the tumor microenvironment. Doxorubicin conjugation with quantum dots leads to bypassing drug efflux pumps, responsible for multidrug drug resistance. Targeting with Mucin 1 aptamer improves biodistribution, enhances cellular internalization specifically by cancer cells and prevents side effects. The quantum dots utilized in this study emit a fluorescence signal that is quenched by doxorubicin. When the conjugate is formed, it is possible to observe doxorubicin fluorescence, but quantum dots signal is not detected. As the bond hydrolyzes, doxorubicin is released and diffuses away; the quantum dot fluorescence can be detected. The project also achieved high loading capacity of doxorubicin.

Specific Aim 4: To synthesize tumor responsive manganese oxide nanoparticles for magnetic resonance imaging of various cancers and recruitment of nanostructured lipid carriers entrapping vemurafenib to tumor site.

The fourth section includes the design and development of a two part system to allow for combination magnetic resonance imaging (MRI) and targeted cancer therapy. The first system consists of manganese oxide nanoparticles modified with LHRH peptide or melanoma specific monoclonal antibodies for targeting and a biotin modified matrix metalloproteinase 2 (MMP2) cleavable peptide. The LHRH peptide and melanoma antibody will help increase tumor accumulation. Metastatic cancer cells have increased

amounts of MMP2, which would cleave the MMP2-cleavable peptide. The cleaved portion of the peptide contains biotin and acts as a signal.

4 EVALUATION OF THE EFFECT OF DENDRIMER GENERATION ON siRNA CONDENSATION AND GENE SILECING

4.1 Introduction

Novel therapeutic approaches based on RNA interference (RNAi), a post-transcriptional gene silencing mechanism, mediated by small duplex RNA, attract a substantial attention [125-130]. However, similar to other gene therapy strategies, low stability in the bloodstream and poor cell penetration ability of naked small interfering RNA (siRNA) represent main obstacles for the practical use of these methodologies [125-127, 129-131]. Viruses that developed during the evolution the ability to deliver double and single stranded DNA and RNA across the cell membrane. However, the immune response elicited by viral proteins limited the use of viral vectors for delivery of DNA and RNA [132]. Therefore, the development of non-viral systems, which are able to protect siRNA during its journey in the circulation to the site of action and effectively deliver it across the cell membrane to the cytoplasm where it can enter the RNAi pathway and guide the sequence-specific mRNA degradation, is very important in order to exploit their therapeutics potential.

Studies of non-viral gene therapy based on plasmid DNA (pDNA) have being carried out for years to improve systemic delivery and transfection efficiencies of pDNA to the levels required for *in vivo* clinical trials. It has been recognized that a prerequisite for the

facile transport of pDNA through the cell membrane is the condensation (packaging) of the nucleic acids into nanoparticles which can protect pDNA by sterically blocking its degradation by nucleolytic enzymes [60]. pDNA and siRNA are both double-stranded nucleic acids, have anionic phosphodiester backbones with the same negative charge to nucleotide ratio, and can interact electrostatically with cationic agents [125]. Therefore, one can use the knowledge gained from the longer-studied pDNA to develop systems for an effective delivery of siRNA.

However, despite the similarities, pDNA and siRNA are very different from each other in molecular weight and molecular topography with potentially important consequences. The DNA used in gene therapy, is often several kilo base pairs long and possesses a molecular topography, which allows the condensation into small, nanometre size particles when complexed with a cationic agent [40, 125]. Unlike pDNA, the persistence length (the length scale over which the chains behave as rigid rods) of double-stranded RNA is ~70 nm [38] which is about 260 base pairs (bp) based on the value of 2.7Å/bp [133]. Therefore, siRNA with 21 bp essentially should behave as a rigid rod and is difficult to bend. Consequently, the different interactions with cationic agents may result in undesirably large complexes or incomplete encapsulation of siRNA molecules, which thereby may expose siRNA to potential enzymatic or physical degradation in the blood stream prior to the delivery to the targeted cells [40].

Over the years, cationic liposomes and polycations have been explored as nonviral vectors for the delivery of siRNA [128, 134]. An advantage of using polycationic polymers, such as Poly(Ethyleneimine) (PEI), is that they allow for an efficient gene transfer without the need for agents facilitating endosomal escape of the payload. However, such polymers have a wide range of molecular weight distribution and their transfection efficiency and cytotoxicity are dependent on the molecular weight and polydispersity [40, 60, 61, 125]. In contrast, the novel highly branched three-dimensional molecules, called dendrimers, have defined molecular weight and a large number of controllable surface charges and surface functionalities [135]. These properties of dendrimers provide a platform for an effective siRNA intracellular delivery, with potentially less complications from heterogeneity and variable chemistry, commonly seen in other nonviral vectors, such as cationic lipids and Poly(Propyleneimine) (PPI) dendrimers [60, 136, 137]. PPI dendrimers are members of a class of amine-terminated polymers that have been used as efficient gene delivery vectors with low cytotoxicity in a wide range of mammalian cell lines [129, 136, 137]. The multiple functional groups on surface of these dendrimers also allow the design of multifunctional delivery systems containing other active components (*e.g*. targeting moieties, *etc*.) in addition to siRNA [126, 129]. However, most of the synthetic vectors, including dendrimers, usually possess lower efficiency in intracellular nucleic acid delivery [61]. Therefore, fundamental understanding of the molecular structure of nonviral vectors and their function relationship is essential for rational design of nonviral delivery vehicles with the therapeutic effectiveness that can match or be better

than the viral counterpart. Consequently, by linking the chemical structures of cationic vehicles to the morphology and physicochemistry of the respective nucleic acid complexes and their biological properties on cellular and systemic levels is essential for the development of nonviral delivery vehicles with efficiency can match or be better than their viral counterpart. The present work is aimed at studying the properties of nanoparticles formed by the complexation of a model siRNA with PPI dendrimers of different generations, the morphology and cellular toxicity of such complexes and their efficiency to deliver the payload into the cytoplasm and silence the targeted gene.

4.2 Material and Methods

4.2.1 Materials

Dendrimers, poly(propyleneimine) octaamine (DAB Am-8, generation-2, PPI G2), poly(propyleneimine) hexadecaamine (DAB Am-16, generation-3, PPI G3), poly(propyleneimine) dotriacontaamine (DAB Am-32, generation-4, PPI G4), and poly(propyleneimine) tetrahexacontaamine, DAB-Am-64, generation-5, PPI G5) were purchased from Aldrich (Milwaukee, WI), and used without further purification. Ethidium Bromide (EtBr) solution was purchased from Promega (Madison, WI). The sequence of siRNA targeted to BCL2 mRNA (custom synthesized by Ambion, Austin, TX), was 5’-GUGAAGUCAACAUGCCUGC-dTdT-3’ (sense strand) and 5’-GCAGGCAUGUUGACUUCAC-dTdT-3’ (antisense strand). 6-FAM siRNA (SiGLO Green) was

obtained from Applied Biosystems (Ambion, Inc., Foster City, CA). All other chemicals were purchased from Fisher Scientific (Fairlawn, NJ).

4.2.2 Cell Line

Human A549 lung carcinoma cells were obtained from the ATTC (Manassas, VA, USA). Cells were cultured in RPMI 1640 medium (Sigma, St. Louis, MO) supplemented with 10% foetal bovine serum (Fisher Scientific, Fairlawn, NJ). Cells were grown at 37 °C in a humidified atmosphere of 5% CO2 (v/v) in air. All experiments were performed on cells in the exponential growth phase.

4.2.3 Ethidium Bromide Dye Displacement Assay

Fluorescence titration of siRNA-ethidium bromide complexes with different generations of PPI dendrimers were performed as followed. The complexes prepared from siRNA with EtBr intercalated at 4:1 ratio in water and 1 □L aliquots of the dendrimer solutions were sequentially added to 2 μM solution of siRNA in 180 μL of water containing EtBr. After each addition, the mixture was stirred and the fluorescence of the solution was measured (490 nm excitation; 590 nm emission). The total dendrimer amount added to the siRNA solution exceed 5% of the total volume of the mixture, hence sample dilution factors on the measured fluorescence emission intensity was corrected. All fluorescence measurements were performed using a Cary-Eclipse fluorescence spectrophotometer

(Varian, Inc, Palo Alto, CA). The relative fluorescence was based on three independent experiments and calculated using the following equation:

$$\% \text{ Relative Fl.} = \frac{\text{Fl. (obs)} - \text{Fl. (EtBr)}}{\text{Fl. (siRNA + EtBr)} - \text{Fl. (EtBr)}} \times 100$$

where Fl. (obs) - fluorescence of siRNA + ethidium bromide + complexation agent; Fl. (EtBr) - fluorescence of ethidium bromide alone; Fl. (siRNA + EtBr) - fluorescence of siRNA + ethidium bromide.

4.2.4 Formulation of siRNA Complexes

The complexes of siRNA with each generation of PPI dendrimers (G2, G3, G4, and G5) were designed at constant amine/phosphate ratios (N/P ratio) such as 2.4. Briefly, 100 ?M siRNA solutions were mixed with deionized water and an appropriate amount of the dendrimers was added. The final concentration of siRNA in the solution was 4.0 μM, while the concentrations of PPI G2, G3, G4, and G5 dendrimers were 50.4 μM, 25.2 μM, 12.6 μM, and 6.3 μM, respectively. The complexes were stirred and equilibrated for 30 min prior to analysis.

4.2.5 Atomic Force Microscopy (AFM)

In order to obtain AFM images of formulated complexes, 5 μl aliquots of siRNA-dendrimer solutions were deposited on a freshly cleaved mica surface. After 5 min of incubation, the surface was rinsed with several drops of nanopure water, and dried under a flow of dry nitrogen. AFM images were obtained using Nanoscope IIIA AFM (Digital Instruments, Santa Barbara, CA) in tapping mode, operating in ambient atmosphere.

4.2.6 Agarose Gel Retardation Assay

The complexes of siRNA with different generations of PPI dendrimer were prepared in water as already described. Free siRNA was used as the control. Double-stranded RNA ladder (New England Biolabs) with the smallest base pairs at 21 was used as a size reference. The samples were further diluted with water and electrophoresed in 4% agarose gel at 100 mV for 60 min in DPBS buffer and stained with EtBr. The gels were digitally photographed, and scanned using Gel Documentation System 920 (NucleoTech, San Mateo, CA).

4.2.7 Dynamic Light Scattering (DLS)

The DLS studies were performed using the Dawn EOS multi-angle light scattering spectrometer modified with a QELS attachment (Wyatt Technology Corp., Santa

Barbara, CA). Data were collected at an angle of 108° using an avalanche photodiode and an optical fiber and processed with the Wyatt QELS software (regularization analysis). Each light scattering experiment consisted of 5 or more 60 s independent readings.

4.2.8 *In vitro* Cytotoxicity

A modified MTT (3-(4,5-dimethylthiazol-2-yl)-2,5-diphenyltetrazolium bromide) assay was used to assess the cytotoxicity of different generations of PPI dendrimer as previously described [138]. To measure cytotoxicity, human A549 lung carcinoma cells were separately incubated in a microtiter plate with different concentrations of each PPI G2, G3, G4, and G5 dendrimers. Control cells received an equivalent volume of fresh medium. The duration of incubation was 24 h. On the basis of these measurements, cellular viability was calculated for each dendrimer concentration. A decrease in the cellular viability indicated an increase in dendrimer toxicity.

4.2.9 Cellular Internalization

To analyse cellular internalization and intracellular localization of the condensed complexes, 6-FAM labelled siRNA was used as previously described [129, 139]. Prior the visualization, A549 cells were plated (20,000 cells per well) in a 6-well tissue culture plate. The cells were treated within 24 hrs with the siRNA complex prepared with different generations of PPI dendrimer. The treatment of the A549 cells was performed

in such a manner that the final concentration of siRNA was 0.25 μM and the concentrations of PPI G2, G3, G4, and G5 dendrimers were 3.15 μM, 1.58 μM, 0.79 μM, and 0.39 μM, respectively. After 24 hrs of treatment, the cells were washed three times with phosphate buffered saline (PBS) and 1 mL of media was added to each well. Cellular internalization of siRNA-dendrimer complexes were analyzed by fluorescent (Olympus America Inc., Melville, NY) and confocal (Leica Microsystems Inc., Bannockburn, IL) microscopes. To obtain intracellular distribution of siRNA, ten optical sections, known as a z-series, were photographed sequentially, by confocal microscope, along the vertical (z) axis from the top to the bottom of the cell. The obtained fluorescent images were digitally scanned and fluorescence inside cells (that reflects cellular accumulation of labeled siRNAs) was expressed in arbitrary units.

4.2.10 Gene Expression

Quantitative reverse transcription-polymerase chain reaction (RT-PCR) was used for the analysis of expression of genes encoding BCL2 protein and β_2-microglobulin (internal standard) as previously described [140]. RNA was isolated after 24 h incubation of cancer cells with siRNA-dendrimer complexes, using an RNeasy kit (Qiagen, Valencia, CA). First strand cDNA was synthesized by Ready-To-Go You-Prime First-Strand Beads (Amersham Biosciences, Piscataway, NJ) with 4 mg of total cellular RNA and 100 ng of random hexadeoxynucleotide primer (Amersham Bioscience, Piscataway, NJ). After synthesis, the reaction mixture was immediately subjected to PCR, which was carried

out using GenAmp PCR System 2400 (Perkin-Elmer, Shelton, CT). The following pairs of primers were used: *BCL2* – GGA TTG TGG CCT TCT TTG AG (sense), CCA AAC TGA GCA GAG TCT TC (antisense); β_2-*microglobulin* (β_2-*m*) – ACC CCC ACT GAA AAA GAT GA (sense), ATC TTC AAA CCT CCA TGA TG (antisense). PCR products were seperated in 4% NuSieve 3:1 Reliant agarose gels in 1*TBE buffer (0.089 M Tris/Borate, 0.002 M EDTA, pH 8.3; Research Organic Inc., Cleveland OH) by submarine gel electrophoresis. The gels were stained with ethidium bromide, digitally photographed and scanned using Gel Documentation System 920 (NucleoTech, San Mateo, CA). Gene expression was calculated as the ratio of mean band intensity of analyzed RT-PCR product (*BCL2*) to that of the internal standard (β_2-*m*). The value of *BCL2* gene expression for the cells incubated with fresh medium (control) was set as 100%.

4.2.11 Statistical Analysis

Data were analysed using descriptive statistics, single-factor analysis of variance (ANOVA), and presented as mean values ± standard deviation (SD) from four to eight independent measurements. The comparison among groups was performed by the independent sample student's t-test. The difference between variants was considered significant if $P < 0.05$.

4.3 Results

4.3.1 Evaluation of Interaction Between siRNA and PPI Dendrimers of Different Generations by EtBr Displacement Assay

Similarly to pDNA, the complex formation between negatively charged siRNAs and positively charged polycations is primarily driven due to electrostatic interaction. The amount of polycations needed for the complex formation could be estimated by N/P (nitrogen/phosphate) ratios, which refer to the ratio of the positively charged primary amine groups of polycations to negatively charged phosphate groups of siRNA [125]. EtBr intercalates between the base pairs of the DNA double helix, yielding a highly fluorescent DNA-EtBr complex [141]. Upon polycations binding, the DNA double helix structure is distorted and EtBr is expelled from the DNA-EtBr complex, resulting in a decrease of fluorescence [141]. The degree of EtBr displacement thus provides for a measure of the binding affinity, indicating the relative strength of the interaction between DNA and polycations. A similar process was found for siRNA in the present study, as shown in Fig. 4.1A. Although the exact mechanism of EtBr release from siRNA requires an additional detailed study, the differences in the ability of dendrimers to displace EtBr from siRNA provide a comparison of the binding affinities between siRNA and the PPI dendrimers of different generations [142]. Fig. 4.1B shows that fluorescence intensities decreased progressively with increasing N/P ratios up to 0.36, 0.55, 0.74, and 0.92 for PPI G4, G5, G3 and G2, respectively. These ratios, which represent the apparent

end point of complexation for each PPI dendrimer generations, respectively, indicated that the interaction strength between PPI dendrimers and siRNA decreases as follows: G4 > G5 > G3 > G2.

4.3.2 Size and Morphology of Formulated siRNA-Dendrimer Complexes

Tapping mode AFM was used to study the size and morphology of siRNA complexes prepared in the presence of different generation of PPI dendrimers. To ensure a complete siRNA complexation, all the siRNA complexes with different generation dendrimers were formulated at a ratio of 2.4, which is several times higher than the apparent end points of condensation observed by EtBr dye displacement assay. Agarose gel retardation assay was applied to further ensure that this N/P ratio was sufficient for siRNA complex formation (Fig. 4.2A). As shown in Fig. 4.3, fibre- and sphere-shaped nanostructures were formed in the presence of PPI G2 to G5 dendrimers after 30 min of condensation. The lower generations of dendrimers are capable to complex siRNA resulting in the formation of randomly aggregated nanofibers (G2) (Fig. 4.3A), or a mixture of nanofibers and toroids (G3), respectively (Fig. 4.3B). The height of the fiber-like structures was around 1.7 nm with the length varied from 100 nm to several μm, whereas the average height and diameter of toroids were 2.9 ± 0.2 nm and 176.6 ± 12.3 nm, respectively. The relatively weak electrostatic cooperative interaction between siRNA and PPI G2 or PPI G3 may be the reason to form this fiber shaped structures. On the other hand, the products of siRNA condensation with higher generations of PPI

dendrimers appear to be relatively uniform nanoparticles with average diameters 150.3 ± 24.7 nm and 150.1 ± 22.2 nm for PPI G4 and PPI G5, respectively (Fig. 4.3C-D). Whereas the average heights of the siRNA complexes formed in the presence of PPI G4 and PPI G5 were 6.2 ± 0.9 nm and 5.4 ± 0.9 nm, respectively. It is worthy to mention that the height values of spherical gene delivery complexes measured by AFM are almost always lower than their diameters. The major factors contributing to the lower height values are elastic deformation induced by AFM tip-sample interaction and the compression caused by the attractive forces between complexes and the substrate [143]. DLS technique was also used to determine the hydrodynamic size of the siRNA complexes without perturbation by the surface immobilization process and the AFM tip. Similar trend was found with increasing generations of the PPI dendrimer, even though the absolute size of the complexes measured by DLS was relatively small. The hydrodynamic diameter for siRNA complexes formed in the presence of higher generations PPI dendrimers were 96.8 ± 11.3 nm and 101.2 ± 23.8 nm for PPI G4 and PPI G5, respectively. Additionally, the solutions of siRNA-PPI G2 and siRNA-PPI G3 had hydrodynamic diameters of 224.0 ± 58.5nm and 129.8 ± 26.4 nm, which was attributed to the fiber and torus-like constructions (Fig 4.4A).

4.3.3 Cellular Internalization and Intracellular Localization of siRNA-Dendrimer Complexes

To achieve an enhanced gene silencing therapeutic effect, sequence-specific siRNA molecules have to be delivered efficiently into the cytoplasm of cells, where the RNAi machinery is located. To determine whether the PPI dendrimers studied were able to efficiently deliver siRNA into cancer cells, the cellular internalization of the FAM-labelled siRNA (free or complexed) was investigated by fluorescence microscopy after their incubation with A549 human lung cancer cells. The quantitative evaluation of siRNA internalization efficiency based on the emission intensity showed that the intracellular uptake of the complexed and free siRNA was dramatically different and strongly dependent on dendrimer generation (Fig. 4.4B). Whereas free siRNA as well as siRNA-PPI G2 complexes were not internalized by the cells, siRNA complexes formulated in the presence of G3, G4 and G5 dendrimers were capable to facilitate siRNA internalization into the cytoplasm. Overall, the efficiency of the studied complexation agents to provoke siRNA intracellular uptake declines in the following order: PPI G4 > PPI G5 > PPI G3 > PPI G2 (Fig. 4.4B). The result is consistent with the ability of the dendrimers in provoking siRNA condensation into discrete nanoparticles. In the present study, the intracellular distribution of the siRNA-PPI complexes in A549 human lung cancer cells was investigated by confocal microscopy (Fig. 4.5). Analysis of the obtained images demonstrated the fluorescence from 6-FAM labeled siRNA delivered by PPI G3, G4 and G5 dendrimers was localized primarily in the cytoplasm of the cells and was not registered in the nuclei. The siRNA complexes formed with PPI G3-G5 dendrimers were uniformly distributed in the cytoplasm from the top to the bottom of the cells (Fig. 4.5C-E).

4.3.4 Gene Silencing Efficiency of siRNA-Dendrimer Complexes *in vitro*

In order to achieve therapeutic effects by the internalized siRNA, the complex which protects siRNA in extracellular environment has to be able to escape from the endosome and release siRNA in cytoplasm where it can guide sequence specific mRNA degradation. To evaluate the silencing efficacy of the siRNA delivered by PPI dendrimers, the siRNA complexes formulated in the presence of four different generations of PPI dendrimers were incubated with A549 lung cancer cells and the expression of targeted BCL2 mRNA was measured by RT-PCR. Figure 6 shows that siRNA delivered by PPI G5 and G4 dendrimers sufficiently induced degradation of the targeted BCL2 mRNA. PPI G5-siRNA complexes resulted in 75% gene knockdown, while PPI G4-siRNA exhibited almost complete suppression of the targeted BCL2 mRNA in A549 lung cancer cells. On the other hand, siRNA complexed with PPI G3 dendrimer resulted in only a 40% decrease in gene knockdown and the condensed siRNA with PPI G2 dendrimer showed no statistically significant silencing effect. Gene silencing was not observed with naked siRNA and all generations of PPI dendrimer without siRNA (data not shown).

4.3.5 *In vitro* Cytotoxicity of PPI Dendrimers

Cytotoxicity of gene transfection vectors including viral vectors, inorganic nanoparticles, cationic liposomes and polymers is considered as a substantial concern for their clinical applications. In order to examine whether different generations of PPI dendrimers influenced cell viability of A549 human lung cancer cells, the MTT assay was employed

in the current study. Figure 4.2B shows the average data obtained in three independent experiments with increasing concentration of PPI dendrimers with different generations. The cytotoxicity of the dendrimers increased with the generation, following the order of the least to most cytotoxic: G2 < G3 < G4 < G5. The data are correlated with membrane damage effects, implying that the increase in positive charge causes more efficient binding to the negatively charged cell membrane and destabilizing them [144]. In the *in vitro* experiments described here, the concentrations of PPI G2, G3, G4 and G5 dendrimers was 3.15 μM, 1.58 μM, 0.79 μM and 0.39 μM, respectively, which are substantially lower than the threshold of cellular toxicity of the carriers.

4.4 Discussion

In the present study, we evaluated PPI dendrimers of different generations (from 2 to 5) in terms of their ability for intracellular delivery of siRNA. It was found that the structure of dendrimers substantially influences their abilities to form stable complexes with siRNA and to deliver the payload to the cytoplasm. Among the all studied dendrimers, PPI G4 dendrimer is the most suitable for this purpose.

Generally, the binding affinity of polycations to nucleic acids is determined by the number of charges and their density per molecule available for the interaction. With each increasing generation of the PPI dendrimer, the number of surface amine groups, which are most likely to bind siRNA, doubles. Therefore the strength of the bond increases with dendrimer generations, which is largely due to the increase in the

number of primary amino groups in higher generation dendrimers. Additionally, it was reported that DNA binding affinity with dendrimers was largely affected by the size of dendrimers, which increases with each generation [135]. Molecular modelling studies of PPI dendrimers of all 5 generations [145] showed that the PPI G1 appears to bind across the major groove of DNA, PPI G3 is sufficiently large to bind across an entire helical turn, spanning major as well as minor groove. For generation 4 and 5, a significant proportion of the PPI dendrimer molecules were able to interact directly with multiple DNA strands.

We found that PPI G4 was more efficient in terms of complex formation with siRNA, despite the PPI G5 dendrimer contains more primary amino groups (64 vs. 32) and have larger size (the hydrodynamic diameters of G4 and G5 dendrimers in water solutions are about 3.12 and 3.96 nm, respectively [146]. These results are in a good agreement with other studies [137], which demonstrated that PPI G4 dendrimer was the most efficient triplex-forming oligodeoxynucleotide delivery agent for five cancer cell lines. It is also consistent with our previous study on the compaction and delivery of antisense oligonucleotides into breast cancer cells [136].

The better efficiency of PPI G4 dendrimer to provoke siRNA complexation compared to PPI G5 dendrimer could be explained by the difference in the flexibility of the dendrimers, which decreases with an increase in the number of dendrimer generation [147]. It was reported that partially degraded PAMAM dendrimers were more efficient than the intact dendrimers in condensation of DNA and antisense oligonucleotides,

because they are more easily collapsed after the neutralization of the charge with nucleic acid due to the enhanced flexible structures [148].

We found that G4 dendrimer has the highest cooperative electrostatic interaction with the siRNA despite of G5 dendrimer has the highest charge density, possibly the decreased flexibility or steric hindrances of G5 that are resulted in a relatively lower cooperative interaction with the siRNA. Since the flexibility of a transfection vector as well as the size and the amount of protonated primary amines on the outer surface drives its ability to compact nucleic acids tightly, the optimal combination in PPI G4 structures makes it the most efficient complexation agent among all other generations.

The size and morphology of siRNA complexes are an important factor in siRNA internalization and can dramatically influence their transfection efficiency [126, 127, 129, 136]. We found that low generation of dendrimers (G2 and G3) formed with siRNA randomly aggregated nanofibers (G2) or a mixture of nanofibers and toroids (G3). In contrast, higher generations of PPI dendrimers formed well-condensed relatively uniform spherical nanoparticles. At the same time we revealed that complexes of G2 and G3 dendrimers with siRNA were unable to penetrate cellular cytoplasm *in vitro.* Relatively low cellular internalization of siRNA delivered by PPI G2 and PPI G3 dendrimers may be at least partially related to the presence of large aggregated structures (fibers and thin toroids) in the complexes. Furthermore, it was reported that electrostatic interactions between the negatively charged cell membrane and positively

charged particles can enhance their cellular uptake [136]. It was reported that complexation of DNA with PPI dendrimers G1 and G2 led to the formation of electroneutral complexes even at dendrimer:DNA charge ratios > 1 [149]. The higher generations of dendrimers were able to produce charged soluble complexes because of the ability to form overstoichiometric complexes with a net positive charge. Recently we also found that all five generations of PPI dendrimers could provoke nanoparticles formation with antisense oligonucleotides (ASO) targeted to the c-myc oncogene [136]. However, only generation 4 and 5 dendrimers could deliver ASO to cell nuclei as determined from a confocal microscopic study. Zeta potential measurement of the ASO-PPI complexes formed with dendrimers of different generations shows that the complexes formed from higher generation PPI dendrimers had much higher positive zeta potentials than the lower generation dendrimers. Even though agarose gel retardation assay demonstrated that the siRNA-PPI dendrimer complexes formed from all five generations were retarded, the complexes with lower generation dendrimers may also have lower positive charges, similar to the situation with ASO-dendrimer complexes. Additionally, it was found [150] that large DNA aggregates formed under noncooperative conditions could not be internalized into cells, and only the fully compacted DNA nanoparticles formed from cooperative binding were able to penetrate through the cellular plasma membrane. Since PPI G5 dendrimer has less cooperative electrostatic interaction with siRNA when compared with G4, we hypothesize that the siRNA nanoparticles formed from these two generations may have different physical chemical properties, which may influence the cell uptake. It is also possible that the

amount of siRNA nanoparticles formed with PPI G5 dendrimers via cooperative electrostatic binding was less than that in G4 dendrimers. In addition, we have recently demonstrated [129] that siRNA-PPI G5 nanoparticles showed aggregation in cell medium, which could prevent some portion of siRNA from the cellular internalization. Although further more detailed studies are required for the investigation of detailed mechanisms of the phenomenon, one can conclude that generation 3 dendrimers provide the most efficient intracellular delivery of complexated siRNA.

In the present study, we found that delivered by dendrimers siRNA located mainly in the cellular cytoplasm but not in nuclei. Since siRNA functions by binding to RNA-induced silencing complex in the cytoplasm, the delivery of siRNA by PPI dendrimers to the cytoplasm but not to nucleus may have the advantage of increasing siRNA gene silencing activity and avoiding toxicity to the nucleus. It has been previously reported that efficiency of RNAi activity was depended on the siRNA localization in different intracellular compartments [151]. Most of the reports show that siRNA delivered by both liposome and cationic polymers is localized in cytoplasm and not in the nucleus even after extended periods of time [40, 128, 134, 152]. However, it was reported that PAMAM dendrimers have a tendency to alter siRNA subcellular localization pattern, which is concentration dependent [151]. Using higher concentration of PAMAM, they observed that the internalized siRNA was localized in both nucleus and cytoplasm. The authors believe that such distribution correlates with the observed lower RNAi activity [151]. Overall, the present study showed that the targeted gene silencing ability of the

siRNA-dendrimer complex depends on the dendrimer generation, following the same trend as the ability of PPI dendrimer in provoking siRNA complexation and facilitating cellular internalization.

It was showed that PPI dendrimers can be used for the delivery of a plasmid DNA [145]. The greater conformational mobility of the long DNA molecules may facilitate its interaction with the extended structure of lower generation dendrimers more efficiently than the interaction of these dendrimers with the 21 bp siRNA in this study. They also found that the number of binding sites between DNA and the dendrimer increased with molecular weight. It is possible that for a long DNA molecule, sufficient binding sites may be achieved with lower generation dendrimers compared with small siRNA. This is consistent with the reports showing that short DNA molecules were more difficult to condense into well-defined nanoparticles [145, 153]. Due to physicochemical and structural differences, conditions for transfection of plasmid DNA could be different from conditions for transfection of siRNA. The conditions may be more comparable to the short antisense and triplexing forming oligonucleotides [145, 153].

Among all dendritic vectors, PAMAM are the most extensively used carriers for plasmid DNA and antisense oligonucleotides [126, 127, 131]. It was also demonstrated that non-degradable PAMAM dendrimers are efficient for siRNA delivery and induce potent endogenous gene silencing, which was dependent on the dendrimer generation [130]. On the contrary, it was reported that PAMAM dendrimers have a moderate efficiency

for the delivery of oligonucleotides and are relatively less effective for delivery of siRNA especially in multidrug resistant cancer cells which overexpress P-glycoprotein [131]. In contrast, it was reported that PAMAM dendrimers are efficient for siRNA delivery, while the best generation is G7 [130]. Moreover, the gene silencing ability of the siRNA-PPI dendrimer complex was also dependent on the dendrimer generations. Similarly to the PAMAM dendrimers, siRNA delivered by the dendrimers with higher generation demonstrated more efficient gene silencing. We found that the optimal generation of PPI dendrimer is G4, which is much lower when compared with PAMAM dendrimers. It was also reported that the best gene silencing results were obtained with G7 dendrimers at a N/P ratio of 10-20 [130], while only weak gene silencing was observed when PAMAM G5 was used [131]. PAMAM dendrimers have relatively larger size compared to PPI dendrimers, which should be more efficient in complexation of siRNA to form compacted structures. However, on the other hand, PPI dendrimers contain 100% protonable nitrogen [154]. The existence of multiple amide nitrogen in the inter structure of the PAMAM, which are nonbasic due to the delocalization of their lone electron pairs with the carbonyl group, siRNA binding and proton – sponge capacity of the PAMAM might be compromised compared to PPI dendrimers.

4.5 Conclusions

It was demonstrated that the molecular structure of a nanocarrier, including its charge, size, and flexibility coherently determines siRNA condensation efficiency and the

physicochemical properties of the formed siRNA complexes, which in turn controls cellular uptake of the siRNA and the silencing efficiency of the internalized siRNA. PPI dendrimers can be effectively used for packaging and delivering of siRNA into cancer cells. Quantitative evaluation of the efficiency of PPI dendrimers to provoke 21-bp siRNA condensation revealed that all four generations of PPI dendrimers are capable of siRNA packaging. However, PPI G4 was the most efficient in siRNA complexation compared to other studied generations, including PPI G5 dendrimers. Atomic force microscope studies demonstrated that the lower generations of dendrimers were capable to partially condensate siRNA to randomly aggregated nanofibers (G2), or a mixture of nanofibers and thin toroids (G3). In contrast, the products of siRNA condensation with higher generations of PPI dendrimers (G4 and G5) appear to be uniform discrete nanoparticles with average size of 150 nm. Furthermore, siRNA-PPI G2 complexes did not provide for an efficient internalization of siRNA by cancer cells. In contrast PPI G3, G4 and G5 dendrimers were capable to facilitate siRNA internalization into cytoplasm and silence the targeted mRNA. The silencing efficacy also highly depended on the generations of the PPI dendrimers, with the following trend: PPI G4 > G5 > G3 > G2.

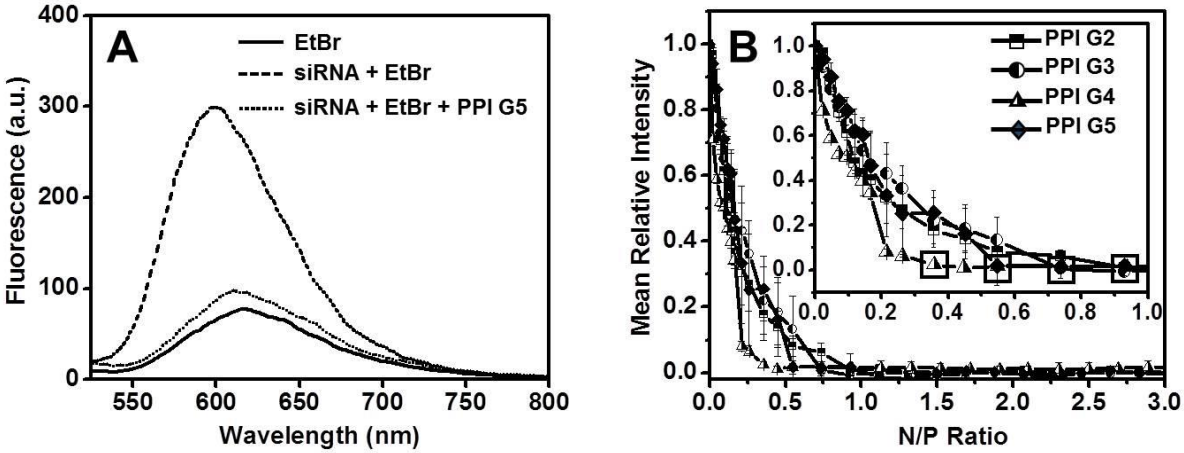

Figure 4.1 Ethidium bromide dye assay for binding affinity A)Representative fluorescence spectra of EtBr alone, EtBr after complexation with siRNA, and EtBR displacement from siRNA by PPI G5 (N/P = 2.4). B) EtBr dye displacement assay by PPI dendrimers. (Inset) Enlargement of the graphs in the vicinity of N/P ratios which represent the apparent ends of complexation. The highlights areas on the graphs demonstrate the N/P ratios, which correspond to the apparent end of siRNA complexation by PPI G2, PPI G3, PPI G4, and PPI G5. Means +/- SD are shown.

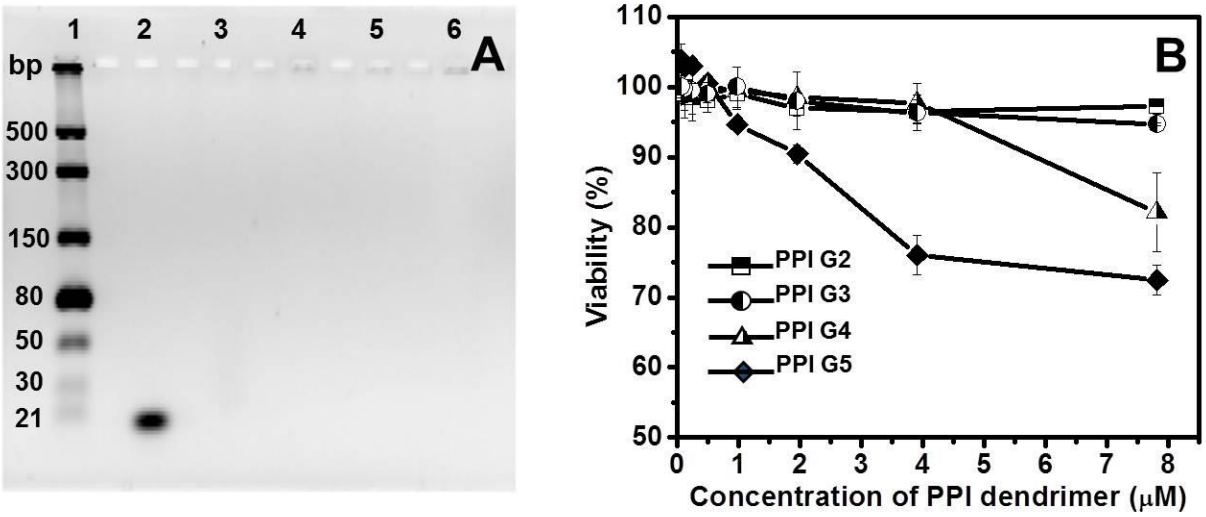

Figure 4.2 A) Evaluation of the siRNA complexion with PPI dendrimers by gel retardation assay (1) RNA size ladder (2) naked siRNA (3) siRNA + PPI G2 (4) siRNA + PPI G3 (5) siRNA + PPI G4 (6) siRNA + PPI G5. B) Viability profile of A549 human lung cancer cells incubated for 24 h with PPI dendrimers of different generations (Means $\pm$ SD are shown).

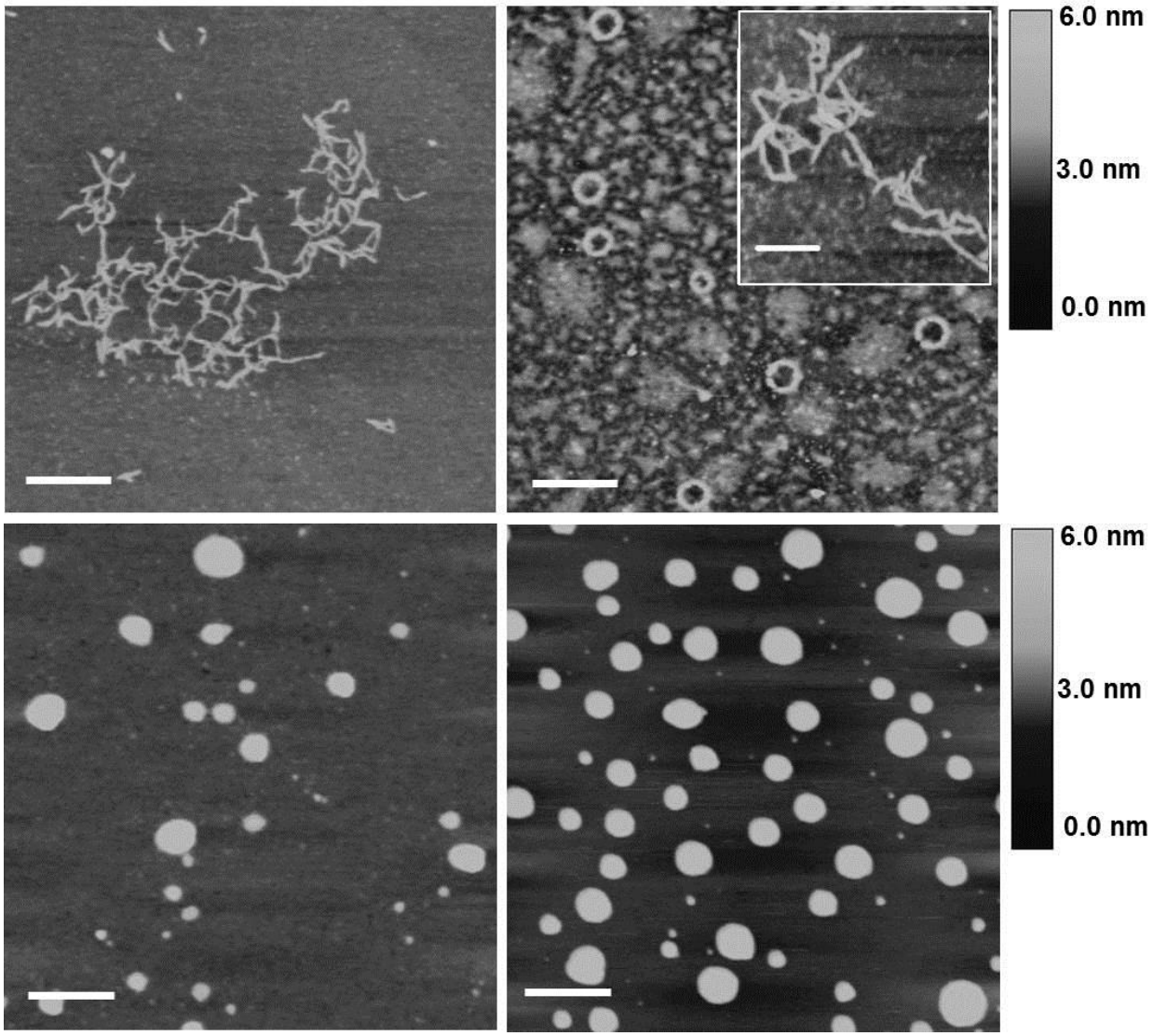

Figure 4.3 Representative AFM images of complexes formed by siRNA in the presence of (A) PPI G2 (B) PPI G3 (C) PPI G4 (D) PPI G5 dendrimers after 30 min of complexation. The bar represents 400 nm in (A), (B), (C), (D) and 200 nm (Inset)

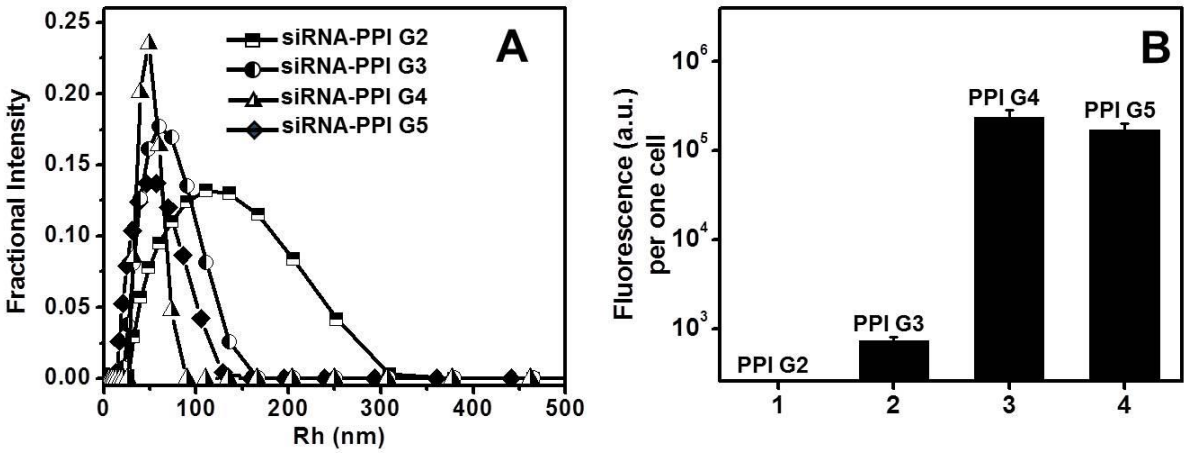

Figure 4.4 A)Representative curves demonstrate the size distribution of siRNA-PPI G2, siRNA-PPI G3, siRNA-PPI G4, and siRNA-PPI G5 complexes measured by DLS. Rh is the hydrodynamic radius. B) Internalization of siRNA complexed with (1) PPI G2 (2) PPI G3 (3) PPI G4 (4) PPI G5 dendrimers by A549 human lung cancer cells. Intracellular fluorescence intensity of FAM-labeled siRNA was estimated based on fluorescence microscopy images recorded under the same experimental conditions.

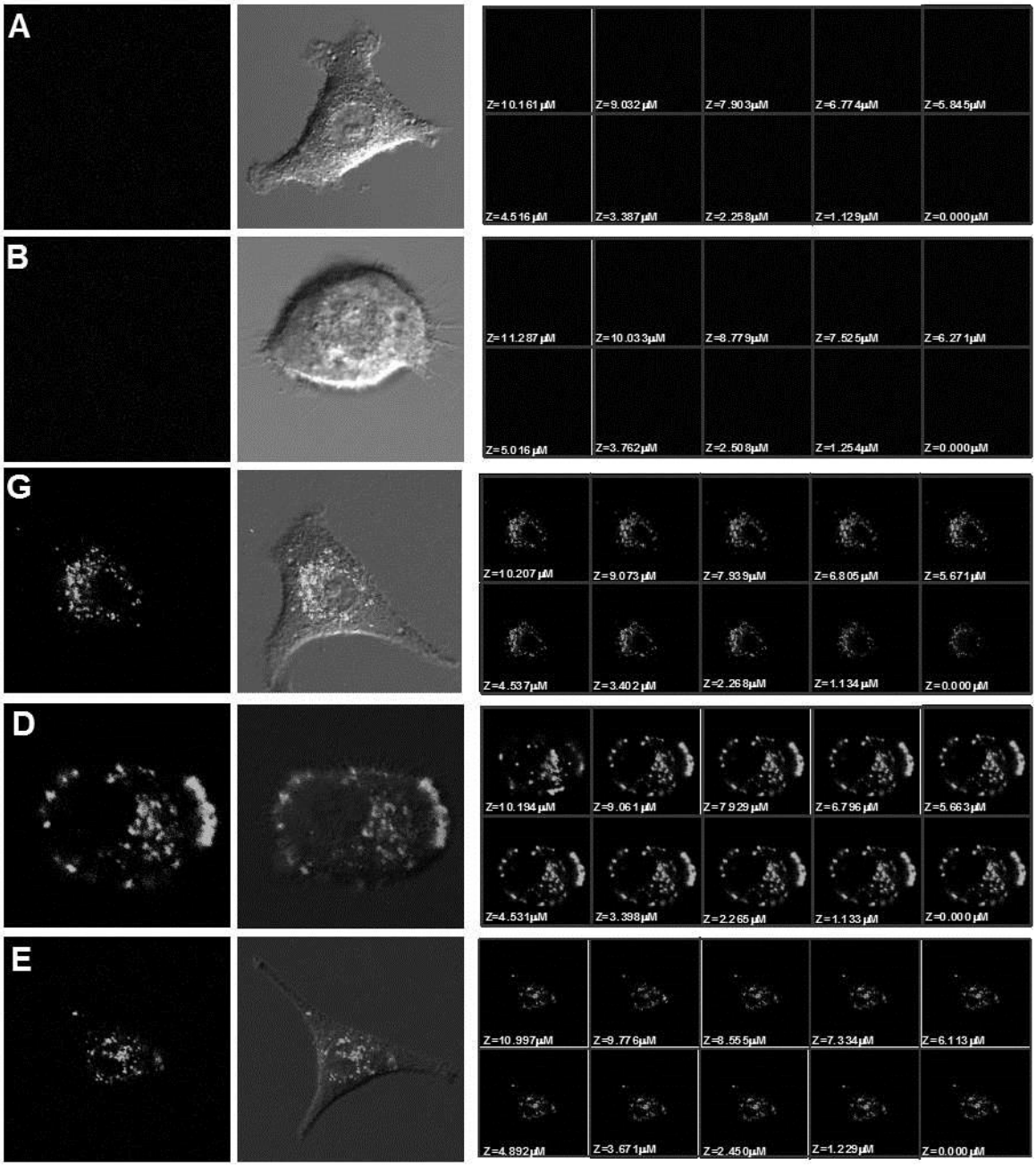

Figure 4.5 Confocal microscopy images (from left to right: fluorescence, superimposed light and fluorescence, z-series) of A549 human lung cancer cells incubated for 24 hrs with (A) naked siRNA; (B) siRNA-PPI G2; (C) siRNA-PPI G3; (D) siRNA-PPI G4; (E) siRNA-PPI G5. Z-series represent fluorescence images from top to the bottom of cells.

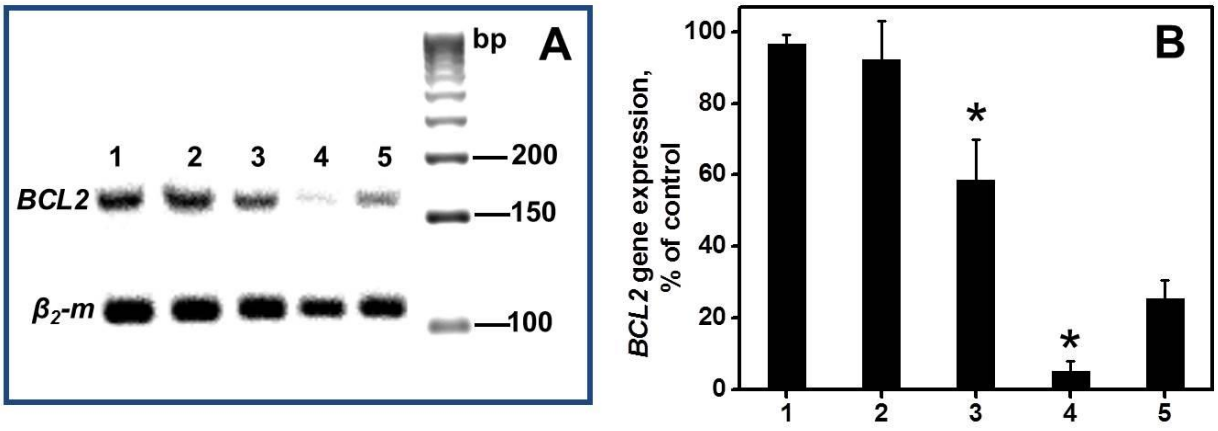

Figure 4.6 The effect of incubation of A549 human lung cancer cells with (1) medium (control); (2) siRNA-PPI G2; (3) siRNA-PPI G3; (4) siRNA-PPI G4; (5) siRNA-PPI G5 on the expression of BCL2 mRNA. Panel A- typical image of RT-PCR products. Panel B- gene expression calculated as the ratio of BCL2 RT-PCR product to the internal standard (β2-m). Means +/- SD are shown. *P < 0.05 when compared with control

5 MULTIFUNCTIONAL NANOMEDICINE PLATFORM FOR CANCER SPECIFIC DELIVERY OF siRNA BY SUPERPARAMAGNETIC IRON OXIDE NANOPARTICLES-DENDRIMER COMPLEXES

5.1 Introduction

Short interfering RNA (siRNA) has been proven to be a versatile tool for silencing genes associated with numerous disease states such as cancer [50, 155-158]. Compared to gene therapy and double stranded RNA (dsRNA), siRNA therapy has significantly higher specificity, higher potency, and a wider range of targetable genes [33, 159]. However, the low penetration ability of naked siRNA into the cellular cytoplasm to induce sequence-specific mRNA degradation represents a primary obstacle limiting the success of siRNA therapy [45, 159-162].

Viruses have been studied as gene delivery vectors; however, the immune response elicited by viral capsid proteins represents a major challenge limiting the wide use of this approach [163]. Viruses are notorious carriers of RNA and DNA and possess the capability to transfect mammalian cells. Therefore, it is sensible to utilize and modify them to deliver genes of interest. The biggest drawback of this approach is the rapid immune recognition and response that render viral-based delivery to be ineffective. Despite extensive research, an efficient, nontoxic gene delivery approach has not yet been developed. It is recognized that the delivery of the nucleic acid by nanocarriers

facilitates the cellular uptake of DNA/siRNA and increases their gene silencing ability [51, 164, 165]. Consequently, considerable interest to the development of non-viral gene delivery vehicles has been generated. In order to provide effective gene silencing, two controversial requirements for such delivery systems should be satisfied: (1) stability of siRNA carrier complex during its journey in the systemic circulation toward the targeted cells and the protection of the payload against the aggressive biological environment and (2) intracellular availability of the nucleic acids in order to permit desired therapeutic effects within the cells [45, 52, 166, 167].

Over the years, cationic liposomes and polycations have been explored as non-viral vectors for the delivery of siRNA [128, 134]. An advantage of using polycationic polymers, such as Poly(Ethyleneimine) (PEI), is that they allow for an efficient gene transfer without the need for agents facilitating endosomal escape of the payload. However, such polymers have a wide range of molecular weight distribution and their transfection efficiency and cytotoxicity are dependent on the molecular weight and polydispersity [40, 60, 61, 125]. In contrast, the novel highly branched three-dimensional molecules, called dendrimers, have defined molecular weight and a large number of controllable surface charges and surface functionalities [135]. These properties of dendrimers provide a platform for an effective siRNA intracellular delivery, with potentially less complications from heterogeneity and variable chemistry, commonly seen in other non-viral vectors, such as cationic lipids and poly(propyleneimine) (PPI) dendrimers [60, 136, 137]. PPI dendrimers are members of a

class of amine-terminated polymers that have been used as efficient gene delivery vectors with low cytotoxicity in a wide range of mammalian cell lines [129, 136, 137]. The multiple functional groups on surface of these dendrimers also allow the design of multifunctional delivery systems containing other active components (*e.g*. targeting moieties, *etc*.) in addition to siRNA [126, 129]. However, most of the synthetic vectors, including dendrimers, usually possess lower efficiency in intracellular nucleic acid delivery [61]. Therefore, fundamental understanding of the molecular structure of non-viral vectors and their function relationship is essential for rational design of non-viral delivery vehicles with the therapeutic effectiveness that can match or be better than the viral counterpart. Consequently, by linking the chemical structures of cationic vehicles to the morphology and physicochemistry of the respective nucleic acid complexes and their biological properties on cellular and systemic levels is essential for the development of non-viral delivery vehicles with efficiency can match or be better than their viral counterpart. The present work is aimed at studying the properties of nanoparticles formed by the complexation of a model siRNA with PPI dendrimers of different generations, the morphology and cellular toxicity of such complexes and their efficiency to deliver the payload into the cytoplasm and silence the targeted gene.

In order to optimize the delivery of siRNA and enhance the efficiency of the treatment, it is highly desirable to employ clinically relevant imaging approaches for *in-situ* monitoring of the disease progression and therapeutic responses [164]. Magnetic Resonance Imaging (MRI) is a powerful tool for non-invasive *in vivo* monitoring due to

its high resolution and lack of ionizing radiation [168, 169]. Superparamagnetic Iron Oxide (SPIO) nanoparticles have been widely investigated as MRI contrast agents to enhance images of biological molecules [170, 171]. Moreover, several approaches have been reported for both siRNA and DNA delivery based on SPIO nanoparticles to timely monitor the delivery process and also to evaluate the therapeutic effects [164, 172, 173]. However, these methods have various shortcomings and do not allow a balanced optimization of siRNA compaction, endosomal escape, and dissociation from the nanoparticles. For example, Medarova *et al.* [164] covalently linked siRNA molecules to the SPIO surface and demonstrated the feasibility of using SPIO nanoparticles as MRI enhancers for *in vivo* tracking of tumor uptake and silencing effects of the siRNA. However, siRNA molecules in this study are tethered to the nanoparticles through chemical bonds between the siRNA and SPIO nanoparticles. Consequently, it is highly possible that such chemical conjugations might potentially compromise the silencing effects of siRNA. Moreover, a chemical conjugation might also limit the siRNA loading capacity of the SPIO nanoparticles. In addition, cellular uptake of existing SPIO-siRNA complexes is not limited only to the targeted cells. Consequently, such non-targeted complexes can be internalized by virtually any cells in the body. This nonspecific delivery of siRNA can result in serious adverse side effects on healthy tissues and limit clinical applications of this approach [160, 174, 175]. In particular, delivery of anticancer drugs, genes, and imaging agents specifically to primary tumor and distant metastases requires the use of a ligand specific to receptors that are overexpressed in cancer cells [52, 160, 174-176].

Previously, we have shown that many cancer cells overexpress receptors to Luteinizing Hormone-Releasing Hormone (LHRH) [113, 177]. A combination of anticancer drugs and LHRH peptide in one delivery system enhanced the efficacy of chemotherapy and decreased the adverse side effects of treatment to healthy organs [114, 178, 179].

In the present study, we focus on development and characterization of a complex tumor-targeted Drug Delivery System (DDS) for the simultaneous delivery of siRNA and MRI contrast agents (SPIO) specifically to cancer cells. We utilize the ability of small SPIO nanoparticles (5 and 10 nm) to cooperatively form complexes of siRNA with Polypropyleneimine Generation 5 (PPI G5) dendrimers [52]. To integrate tumor-specific targeting moiety and increase steric stability, the formulated siRNA nanoparticles were modified with heterobifunctional Poly(ethylene glycol) (PEG). The distal end of PEG was coupled with a synthetic analog of LHRH decapeptide as a targeting agent.

5.2 Materials and Methods

5.2.1 Materials

Poly(propyleneimine) tetrahexacontaamine dendrimer generation 5 (PPI G5), 2,4,6-Trinitrobenzenesulphonic Acid (TNBSA), oleic acid, 1-octadecene, Poly (Maleic Anhydride- *alt*-1-Octadecene) (PMAO, MW=30,000–50,000 Da), Poly (Diallyldimethylammonium chloride) (PDDA, MW 120,000 Da), microsized iron (III) oxide, Sodium Dodecyl Sulfate (SDS), and (4-(2-Hydroxyethyl)-1-

Piperazineethanesulfonic acid) (HEPES) were obtained from Sigma-Aldrich(Milwaukee, WI) and used without further purification. Ethidium Bromide (EtBr) solution and α-Maleimide-ω-N-hydroxysuccinimide ester Poly(ethylene glycol) (MAL-PEG-NHS) were purchased from Promega (Madison, WI) and NOF Corporation (White Plains, NY), respectively. The sequence of antisense of siRNA targeted to BCL2 mRNA (obtained from Ambion, Austin, TX), was 5'-GUGAAGUCAACAUGCCUGC-dTdT- 3' (sense strand) and 5'-GCAGGCAUGUUGACUUCAC-dTdT-3' (antisense strand). The non-targeted mock siRNA (negative control) (5'-CCUCGGGCUGUGCUCUUUU-dTdT-3' sense strand and 5'-AAAAGAGCACAGCCCGAGG -dTdT-3' antisense strand), 5 carboxyfluorescein (FAM) labeled siRNA were obtained from Applied Biosystems (Ambion, Inc., Foster City, CA). A synthetic analog of LHRH, Lys6–des-Gly10–Pro9-ethylamide (Gln–His–Trp–Ser–Tyr–DLys(DCys)–Leu–Arg–Pro–NH–Et) peptide was synthesized according to our design [114, 177-179] American Peptide Co. (Sunnyvale, CA). All other chemicals were purchased from Fisher Scientific (Fairlawn, NJ). Cisplatin (CIS) was purchased from Sigma (St. Louis, MO).

5.2.2 Superparamagnetic Iron Oxide (SPIO) Nanoparticles Preparation

Iron oxide nanocrystals of 5 nm in diameter were synthesized in organic solvents at high temperature. Typically, microsized iron oxide was mixed with oleic acid, 1-octadecene, and then heated to 320˚C for a certain time to produce monodisperse (5–10% size distribution) iron oxide nanocrystals. The size of nanoparticles was controlled by

reaction time, temperature, and the iron oxide and oleic acid concentrations. After the reaction was completed, the mixture was cooled and the iron oxide nanocrystals were precipitated out of 1-octadecene by chloroform/acetone, and then redispersed in chloroform. These nanocrystals were highly crystalline and uniform but were not soluble in water due to the hydrophobic oleic acid capping layer. For solubilization of iron oxide nanoparticles in water, we employed a modified previously published method based on forming micelles through amphiphilic polymers (PMAO) for transferring iron oxide nanocrystals from organic solvents into water [180, 181].

The excess of PMAO amphiphilic polymers was removed through ultracentrifugation (600,000 g for 45 min). 5 mg of the PMAO modified iron oxide nanoparticles was added to 20 mL of 10 mg/mL PDDA aqueous solution in 20 mM Tris buffer. The PDDA was allowed to absorb for 20 min under stirring. The formed nanoparticles were purified by the method described above and used for further studies.

5.2.3 Ethidium Bromide Dye Displacement Assay

Fluorescence titration of siRNA/EtBr with the complexation agents were performed as previously described [52]. The complexes were prepared by the intercalation of siRNA with EtBr at 4:1 ratio (siRNA base pairs to EtBr) in water. 1µL aliquots of complexation agents were sequentially added to 2 µM solution of siRNA in 180 µL water containing EtBr.

After each addition, the mixture was stirred and the fluorescence of the solution was measured (490 nm excitation; 590 nm emission). Binding of the complexation agents caused a displacement of bound EtBr, resulting in a decrease in the fluorescence emission intensity. The total amount of complexation agents added to the siRNA solution exceeded 5% of the total volume of the mixture, hence sample dilution factors on the measured fluorescence emission intensity was corrected. All fluorescence measurements were performed using a Cary-Eclipse fluorescence spectrophotometer (Varian, Inc, Palo Alto, CA). The relative fluorescence was based on three independent experiments and calculated using the following equation:

$$\%\ \text{Relative Fl.} = \frac{\text{Fl. (obs)} - \text{Fl. (EtBr)}}{\text{Fl. (siRNA + EtBr)} - \text{Fl. (EtBr)}} \times 100$$

where Fl. (obs) - fluorescence of siRNA + ethidium bromide + complexation agent; Fl. (EtBr) - fluorescence of ethidium bromide alone; Fl. (siRNA + EtBr) - fluorescence of siRNA + ethidium bromide.

5.2.4 Preparation of SPIO-PPI G5-siRNA Complexes

Prior to the cooperative complexations of siRNA with SPIO nanoparticles and PPI G5, the stock solutions of the mixtures were prepared by adding PPI G5 dendrimer to SPIO nanoparticle solutions with the ratio of primary to the quaternary amines equal to 5:1. The complexes of siRNA with mixture of SPIO and PPI G5 dendrimer were prepared at amine/phosphate ratio (N/P ratio) equal to 0.73. Briefly, siRNA solution was mixed with HEPES buffer (5 mM, pH 7.2) and an appropriate amount of the complexation agents was added. For *in vitro* studies, the final concentration of siRNA in the solution was 4.0 µM. For *in vitro* and *in vivo* studies the final concentrations of siRNA in the solutions were 60 µM and 30 µM, respectively. The samples were vortexed briefly, and the solutions were then incubated at room temperature for 30 min to ensure complex formation.

5.2.5 Modification of SPIO-PPI G5-siRNA Complexes with PEG and LHRH

In order to modify the SPIO-PPI G5-siRNA complexes, NHS-PEG-MAL was reacted with primary amines on the surfaces of the particles in 5 mM HEPES buffer (pH 7.2). The ratio of primary amines to PEG was 10:1. The reaction was carried out for 1 hr at room temperature. PEGylated SPIO-PPI G5-siRNA complexes were then mixed with LHRH peptide dissolved in a HEPES buffer and incubated overnight at 4 ºC. The ration of PEG-MAL:LHRH in the reaction mixture was 1:2. The resulting product was dialyzed against

deionized water using a Spectra/Pore dialysis membrane with the molecular weight cutoff of 10,000 Da obtained from Spectrum Laboratories, Inc. (Rancho Dominguez, CA).

5.2.6 Degree of PEGylation

The percentage of amino groups available for PEGylation as well as the decrease in their concentration after the reaction was determined by modified TNBSA assay [52]. Briefly, 180 µL solution of either non-modified or PEGylated SPIO-PPI G5-siRNA complexes was mixed with 4 µL of TNBSA solution (0.03M in water). Absorbance at 420 nm was measured after 30 min incubation at room temperature. All absorption measurements were performed using a Cary-500 fluorescence spectrophotometer (Varian, Inc, Palo Alto, CA). The final concentration of primary amines was calculated using standard curves. Standard curves were prepared by plotting the average blank corrected absorption at 420 nm reading for each standard vs. its concentration in µM.

5.2.7 Agarose Gel Retardation Assay

The complexes of siRNA with mixtures of complexation agents containing SPIO nanoparticles and PPI G5 were prepared as described above. Free siRNA was used as the control. Double-stranded RNA ladder (New England Biolabs Inc., Ipswich, MA) with the smallest base pairs (bp) at 21 bp was used as a size reference. The samples were further diluted with water and electrophoresed in 4 % agarose gel at 100 mV for 60 min in DPBS and stained with EtBr. The gels were digitally photographed and scanned using the Gel

Documentation System 920 (Nucleo-Tech, San Mateo, CA). Complexation of siRNA prevented staining of siRNA by EtBr and led to the disappearance of the siRNA band. Therefore, the fluorescent intensity of the 21 base pair band on the gel disappeared when siRNA was complexed with SPIO nanoparticles and dendrimers.

5.2.8 Evaluation of LHRH Peptide Reaction with SPIO-PPI G5-siRNA Complexes

Determination of the presence of LHRH peptide on the surface of SPIO-PPI G5-siRNA complexes was performed using Bicinchoninic Acid (BCA) protein assay (Pierce, Rockford, IL). The BCA method employs the reduction of Cu^{+2} to Cu^{+1} by protein in an alkaline medium. The combination of Bicinchoninic acid and Cu+1 creates a purple-colored product that absorbs at 562 nm. The amount of product formed is dependent upon the amount of protein in the sample.

The spectra of the product corresponding to free LHRH and SPIO-PPI G5-siRNA-PEG-LHRH complexes have well defined absorbance maximum around 560 nm corresponding to the absorbance of the BCA/copper complex. These complexes are formed as a result of the reaction of BCA reagent with the cuprous cation produced from the reduction of Cu^{+2} to Cu^{+1} by the LHRH peptide [52, 127]. The absorbance maximum was absent in the assay spectra of the non-targeted complexes that are not modified with LHRH. Briefly, 20 µL of the test solution was mixed with 200 µL of working reagent and left to react for 30 min at 37˚C. The solution then was incubated at room temperature for 10 min and the absorbance was measured at 562 nm.

5.2.9 Dynamic Light Scattering

Dynamic Light Scattering (DLS) studies were performed using the Dawn EOS multi-angle light scattering spectrometer modified with a QELS attachment (Wyatt Technology Corp., Santa Barbara, CA). Data were collected at an angle of 108° using an avalanche photodiode and an optical fiber and processed with the Wyatt QELS software (regularization analysis). The duration of each DLS measurement was 60 s. Each light scattering experiment consisted of a minimum of 5 measurements.

5.2.10 Atomic Force Microscopy

In order to obtain Atomic Force Microscope (AFM) images of formulated complexes, 5 µl aliquots of SPIO-PPI G5-siRNA solutions were deposited on a freshly cleaved mica surface. After 5 min of incubation, the surface was rinsed with several drops of nanopure water (Barnstead), and dried under a flow of dry nitrogen. AFM images were obtained using Nanoscope IIIA AFM (Digital Instruments, Santa Barbara, CA) in a tapping mode, operating in ambient air. A 125 µm long rectangular silicon cantilever/tip assembly was used with a spring constant of 40 Nm^{-1}, resonance frequency of 315–352 kHz, and tip radius of 5–10 nm. The applied frequency was set on the lower side of the resonance frequency. The image was generated by a change in amplitude of the free oscillation of the cantilever as it interacted with the sample. The height differences on the surface are indicated by the color code, lighter regions indicating an increase in the

height of the complexes. The height and outer diameter of formulated complexes were measured using the Nanoscope software.

5.2.11 Cell Lines

Two cancer cell lines with a different level of expression of LHRH receptors were used. Human LHRH positive A549 lung carcinoma cells and SKOV-3 LHRH negative ovarian cancer cells were obtained from the ATTC (Manassas, VA, USA). In addition, A549 human lung adenocarcinoma epithelial cell line transfected with luciferase was purchased from Xenogen Bioscience, (Cranbury, NJ). Cells were cultured in RPMI 1640 medium (Sigma Chemical Co., Louis, MO) supplemented with 10% fetal bovine serum (Fisher Chemicals, Fairlawn, NJ). Cells were grown at 37˚C in a humidified atmosphere of 5% CO2 (v/v) in air. All of the experiments were performed on the cells in exponential growth phase.

5.2.12 Cellular Internalization of siRNA

Cellular internalization of FAM-labeled siRNA complexes were analyzed by fluorescence (Olympus America Inc., Melville, NY) and confocal (Leica Microsystems Inc., Bannockburn, IL) microscopes as previously described [50, 52, 127]. To assess cellular internalization and localization of siRNA, ten optical sections, known as a z-series, were scanned sequentially by a confocal microscope along the vertical (z) axis from the top to the bottom of the cell. Prior to the visualization, A549 and SKOV-3 cells were plated

(20,000 cells/well) in 6-well tissue culture plate. The cells were treated with different formulations for 24 hrs. The concentration of siRNA was 0.25 μM. To assess the influence of PPI dendrimer generation on siRNA internalization, the concentrations of PPI G2, G3, G4, and G5 dendrimers were 3.15 μM, 1.58 μM, 0.79 μM, and 0.39 μM, respectively. After 24 hrs of treatment cells were washed three times with phosphate buffered saline (PBS) and 1 mL of fresh medium was added to each well.

5.2.13 *In vitro* Cytotoxicity

The cellular cytotoxicity of the formulated siRNA complexes was assessed using a modified MTT (3-(4,5-dimethylthiazol-2-yl)-2,5-diphenyltetrazolium bromide) assay as described previously [21, 52, 138, 165]. Briefly, A549 cells were separately incubated in 96-well plate with different concentrations of the studied formulations, which resulted in a total of seven separate series of experiments: (1) Control (fresh media); (2) Mixture of 5 nm SPIO nanoparticles and PPI G5 dendrimers; (3) 5 nm SPIO-PPI G5-siRNA complexes; (4) 5 nm SPIO-PPI G5-siRNA-PEG-LHRH complexes; (5) CIS; (6) Mixture of CIS and 5 nm SPIO-PPI G5-siRNA complexes and (7) Mixture of CIS and 5 nm SPIO-PPI G5-siRNA-PEG-LHRH complexes. Control cells received an equivalent volume of fresh media. The duration of incubation was 24 hrs. On the basis of these measurements, cellular viability was calculated for each formulation concentration.

5.2.14 Gene Expression

Quantitative reverse transcription-polymerase chain reaction (RT-PCR) was used for the analysis of the expression of genes encoding BCL2 protein and β2-microglobulin (internal standard) as previously described [21, 140, 182]. RNA was isolated after 24 h incubation of cancer cells with siRNA-dendrimer complexes and modified and non-modified SPIO-PPI G5-siRNA complexes using an RNeasy kit (Qiagen, Valencia, CA). First strand cDNA was synthesized by Ready-To-Go You-Prime First-Strand Beads (Amersham Biosciences, Piscataway, NJ) with 4 mg of total cellular RNA and 100 ng of random hexadeoxynucleotide primer (Amersham Bioscience, Piscataway, NJ). After synthesis, the reaction mixture was immediately subjected to polymerase chain reaction, which was carried out using the GenAmp PCR System 2400 (Perkin-Elmer, Shelton, CT). The following pairs of primers were used: *BCL2* – GGA TTG TGG CCT TCT TTG AG (sense), CCA AAC TGA GCA GAG TCT TC (antisense); β2-microglobulin (β2-m, internal standard) – ACC CCC ACT GAA AAA GAT GA (sense), ATC TTC AAA CCT CCA TGA TG (antisense). PCR products were separated in 4% NuSieve 3:1 Reliant agarose gels in 1X TBE buffer (0.089 M Tris/Borate, 0.002 M EDTA, pH 8.3; Research Organic Inc., Cleveland OH) by submarine gel electrophoresis. The gels were stained with EtBr, digitally photographed, and scanned using the Gel Documentation System 920 (NucleoTech, San Mateo, CA). Gene expression was calculated as the ratio of mean band intensity of analyzed RT-PCR product (*BCL2*) to that of the internal standard (β2-m). The value of *BCL2* gene expression for the cells incubated with fresh medium (control) was set as 100%.

5.2.15 *In vivo* Study

NCR nude mice (female, 6 weeks, 20 g) were purchased from Taconic Farms, Inc. (Germantown, NY). We used a previously described animal model of human cancer xenografts [52, 114, 178]. Briefly, A549 human cancer cells transfected with luciferase (5 x 106) were subcutaneously transplanted into the flanks of female athymic *nu/nu* mice. According to the approved institutional animal use protocol, the tumors were measured by a caliper every other day and their volumes were calculated as d^2 x $D/2$ where d and D are the shortest and longest diameter of the tumor in mm, respectively. When the tumor reached a mean size of 50 mm^3, mice were divided into seven groups and injected intratumorally 3 times within 10 days with 150 µL of the following formulations: (1) saline (control); (2) free non-bound LHRH; (3) free non-bound siRNA; (4) free non-bound CIS; (5) Mixture of CIS and SPIO-PPI G5; (6) Mixture of CIS and SPIO-PPI G5-siRNA; and (7) Mixture of CIS and SPIO-PPI G5-siRNA-PEG-LHRH complexes. The concentrations of CIS and siRNA in the formulations were 2.5 mg/kg and 30 µM, respectively. Changes in tumor size were monitored by real-time bioluminescence in anesthetized animals by IVIS imaging system (Xenogen Bioscience, Cranbury, NJ).

5.2.16 Statistical Analysis

Data were analyzed using descriptive statistics, single factor analysis of variance (ANOVA), and presented as mean values ± standard deviation (SD). Four to eight independent measurements were used for in vitro experiments. Ten animals were used

in each group of *in vivo* experiments. The comparison among groups was performed by the independent sample Student's t-test. The difference between variants was considered significant if $P < 0.05$.

5.3 Results

5.3.1 Mixture of SPIO Nanoparticles and PPI G5 as a Carrier for siRNA Delivery

siRNA complexes were prepared with a mixture of SPIO nanoparticles and PPI G5 dendrimers, which introduced functional primary amino groups on the surfaces of formulated siRNA complexes for their further modification Fig. 5.1. PPI dendrimers were covered with PEG polymers and LHRH peptide as a targeting moiety specific to cancer cells was conjugated to the distal end of the polymer. The efficiency of 5 nm and 10 nm SPIO nanoparticles to cooperatively provoke siRNA complexation with PPI G5 was studied by ethidium bromide dye displacement assay. The ratio of free amines (nitrogen) on PPI dendrimers and SPIO nanoparticles to phosphate on the siRNA (N/P ratio) was employed to quantify the efficacy of cooperative siRNA condensation. Quantitative analysis of the mixture's complexation efficiency reveals that the mixture of 5 nm SPIO and PPI G5 is more effective in provoking siRNA complexation (the apparent end point of complexation of N/P ratio = 0.73) than PPI G5 dendrimer alone (N/P ratio =1.13) and 10 nm SPIO with PPI G5 (N/P ratio =1.3) Fig. 5.2A end points of complexation are denoted as circles in the insert. Therefore, the mixture of 5 nm SPIO and PPI G5 was the most effective complexation agent and was employed for the

development of multifunctional nanomedicine platform for cancer specific delivery of siRNA. Agarose gel retardation assay was additionally involved to confirm the formation of 5 nm SPIO-PPI G5-siRNA complexes formed at N/P ratio which represented the apparent complexation end point obtained from ethidium bromide dye displacement assay. It was found that a complete binding of siRNA (without the presence of a trailing band) with the mixtures of 5 nm SPIO and PPI G5 dendrimers was observed in comparison to free siRNA Fig. 5.2B.

5.3.2 Characterization of siRNA Complexes

DLS measurements at a 108° scattering angle were used to estimate the apparent hydrodynamic diameters of the resulting siRNA complexes. The results of DLS measurements demonstrate that the average diameter of 5 nm SPIO-PPI G5- siRNA complexes was 169.8 ± 28.4 nm Fig. 5.3A. In addition to DLS measurement, the formation of nanosized siRNA complexes has further been confirmed by AFM Fig. 5.3B.

AFM analysis verified that 5 nm SPIO nanoparticles cooperatively with PPI G5 dendrimers could effectively produce complexes with siRNA leading to the formation of discrete particles with an average diameter of 214.3 ± 53.1 nm. The differences in the size of nanoparticles probably reflect the differences in a sample preparation for the size measurements by two different methods. DLS was performed on nanoparticles in a fully hydrated state in solution, whereas AFM studies were carried out on samples dried to

the mica surface, which resulted in flattering of the nanoparticles on the mica surface during the drying process [183].

5.3.3 PEGylation and *in vitro* Transfection of siRNA Complexes

The PEGylation of SPIO-PPI G5-siRNA complexes was carried out by coupling of linear MAL-PEG-NHS to the amino groups on the surface of the complexes, which were introduced by PPI G5 dendrimers. The availability of the primary amines in the structure of the prepared siRNA complexes before PEGylation as well as the decrease in their concentration after PEGylation has been estimated by the TNBSA assay. The result reveals that the degree of PEGylation was 70% for SPIO-PPI G5-siRNA complexes.

To examine the influence of nanoparticles coating on their cellular uptake, PEGylated and non-PEGylated siRNA complexes were incubated with A549 cancer cells in a fresh medium. Fluorescence microscopy studies revealed the fact that PEG modification of SPIO-PPI G5-siRNA complexes enhance their sterical stability and prevent the aggregation of complexes that was abundant in non-PEGylated complexes Fig. 4 (compare panels **A** and **B**). On the other hand, non-PEGylated complexes provided for an effective delivery of labeled siRNA into the cells Fig. 5.4A. As expected, PEGylation of the siRNA complexes decreased their internalization by cancer cells.

In order to evaluate the biological activity of the delivered siRNA, the siRNA targeted to BCL2 mRNA was used in the present study. Fig. 5.5 shows the expression of the *BCL2*

gene in A549 and SKOV-3 human cancer cells treated with siRNA delivered by different SPIO-PPI G5 complexes.

The suppression of BCL2 mRNA by the PEGylated complexes was substantially lower when compared with the corresponding non-PEGylated system (lines 2 and 3). The sufficient decrease in gene silencing activity of the PEGylated complexes corroborates with cellular internalization data. To exclude nonspecific effects on gene expression by SPIO-PPI G5 complexes alone without bound siRNA, we examined whether the mixtures of SPIO nanoparticles with dendrimers could impact the *BCL2* gene expression. RT-PCR analysis demonstrated that the employed siRNA delivery systems did not induce statistically significant changes in the expression of BCL2 mRNA in A549 cancer cells at the studied concentrations Fig. 5.5 (line **5**). Similarly, a mocked siRNA duplex with a scrambled sequence having no significant homology to any known gene sequences was used in this series of the experiments as a negative control. RT-PCR data demonstrated that complexes with such mocked siRNA did not show any statistically significant inhibition of BCL2 mRNA expression confirming the specificity of BCL2 mRNA functional knock-down Fig. 5.5 (line **6**).

5.3.4 Specific Targeting of SPIO-PPI G5-siRNA Complexes to Cancer Cells by LHRH Peptide

In order to conjugate a targeting moiety (LHRH decapeptide) to the siRNA nanoparticles, the maleimide group at the distal end of the PEG-chain was coupled to thiol group

presented by cysteine residue in modified LHRH sequence. The presence of LHRH peptide on the complex surface was confirmed by Bicinchoninic Acid (BCA) protein assay (Thermo Fisher Scientific Inc., Rockford, IL) according to manufacture protocol (data not shown). As shown in Fig. 5.3A, DLS measurements reveal that the diameter of modified SPIO-PPI G5-siRNA complexes was 212.0 ± 35.6 nm, respectively. The increase in the size of the modified siRNA complexes compared to nonmodified ones could be explained by the presence of the polymer layer on the surface of siRNA complexes [52].

In vitro studies were performed to characterize the influence of LHRH peptide as a targeting moiety on the uptake and intracellular activity of the entrapped siRNA. The fluorescence microscopy images demonstrated a sufficient increase in the intracellular internalization of LHRH-targeted complexes by A549 cancer cells which overexpress LHRH receptors Fig. 5.4 (C and D). In contrast, cellular uptake of tumor targeted siRNA complex in LHRH negative SKOV-3 cells was substantially less when compared with non-targeted complexes Fig. 5.4D. These experiments confirmed that the targeted shielded nanoparticles indeed delivered the siRNA specifically to the cancer cells, which overexpress the targeting receptors.

Theoretically, the formulated siRNA complexes could adhere to the surface of LHRH-positive cancer cells and erroneously be visualized on microscopic images as internalized within the cell. To exclude such errors, we analyzed the distribution of LHRH targeted siRNA complexes in different cellular layers from the upper to the lower surfaces of the

cell using confocal fluorescent microscopy. In these experiments, the formulated complexes with FAM labeled siRNA were incubated with human A549 cancer cells. The cells were subjected to confocal microscopy. The z-section of single cells transfected with the modified complexes, formed by complexation of siRNA with the mixture of SPIO nanoparticles and PPI G5 dendrimer, and showed their homogeneous and uniform distribution in all layers of the cell from the top surface to the bottom Fig. 5.6.

To assess the ability of LHRH targeted complexes not only to deliver siRNA but knockdown targeted gene expression, we prepared complexes with BCL2-specific siRNA. In this series of the experiments, both LHRH positive (A549) and negative (SKOV-3) cancer cells were treated with the prepared siRNA complexes for 24 hrs. The RT-PCR data obtained revealed that the LHRH modification of siRNA complexes restore the knockdown activity for siRNA complexes, which was decreased after PEGylation Fig. 5.5 (line **4**). On the other hand, the silencing effect of the BCL2-targeted siRNA was not significant in LHRH-negative cancer cells Fig. 5.5 (line **7**), which is in good agreement with the siRNA cellular internalization result represented in Fig. 5.4.

Therefore, as expected, LHRH peptide proved its capability to target effectively the siRNA complexes to the specific receptors in the plasma membrane of cancer cells.

5.3.5 *In vitro* Cytotoxicity of siRNA Complexes

The influence of the formulated siRNA delivery systems on cell viability was investigated in A549 human lung cancer cell line by the MTT assay. Fig. 5.7A shows the average data from three different experiments with increasing concentration of the complexes. One can see that over 95% average cell viability was observed for both 5 nm SPIO-PPI G5 and 5nm SPIO-PPI G5-siRNA delivery systems at the concentrations used for *in vitro* and *in vivo* experiments of the present study. At a maximum available concentration, the mean cell viabilities for the targeted SPIO-PPI G5-PEG-LHRH complex was 85% compared with that of the control, respectively.

5.3.6 Co-Delivery of siRNA and an Anticancer Drug

The ability of the developed siRNA delivery system to enhance efficiency of a chemotherapeutic drug such as CIS was evaluated in the current study both *in vitro* and *in vivo*. The cellular cytotoxicity of Cisplatin alone and in combination with non-targeted SPIO-PPI G5-siRNA or targeted SPIO-PPI G5-siRNA-PEG-LHRH delivery systems was assessed using a modified MTT assay. Data in Fig. 5.7B shows that cytotoxicity of CIS against multidrug resistant human cancer cells was sufficiently enhanced in the presence of non-targeted or LHRH targeted siRNA delivery vectors. The maximum enhancement of anticancer activity of CIS

5.3.7 Antitumor Activity

Antitumor activities of the proposed formulations with corresponding controls were studied *in vivo* using subcutaneous xenograft model of human cancer. The progression of tumor growth was monitored by an IVIS imaging system and by measuring the tumor volume Fig. 5.8 upper and bottom panels, respectively. It was found that free LHRH and nonconjugated naked siRNA did not significantly influence the growth of the tumor Fig. 5.8 (bottom panel, curves 2-3). Free CIS limited the growth of the tumor at the last day of the treatment on 36.2 % when compared with untreated control Fig. 5.8 (image 4, curve 4). Simultaneous delivery of CIS and SPIO-PPI-G5 dendrimer complex slightly increased the antitumor activity of the drug Fig. 5.8 (image 5, curve 5). The suppression of cellular antiapoptotic defense by siRNA targeted to BCL2 mRNA, delivered by SPIO-PPI G5-siRNA complex simultaneously with CIS significantly enhanced the antitumor activity of the drug. In fact, the tumor volume decreased on 67.5 % after the combinatorial treatment when compared with untreated control Fig. 5.8 (image 6, curve 6).

Targeting of siRNA complexes specifically to the tumor by LHRH peptide led to the further enhancement of the antitumor activity of CIS. The tumor volume decreased on 75.5% when compared with untreated control Fig. 5.8 (image 7, curve 7).

5.4 Discussion

Previously, we developed multifunctional non-viral vector for siRNA delivery based on SPIO nanoparticles modified with PDDA and PMAO, which contain quaternary ammonium and carboxylic functional groups on the periphery for siRNA condensation and endosomal release. These SPIO nanoparticles demonstrated high efficiency to form complexes with siRNA and to facilitate their internalization by the cancer cells. Cellular uptake of such SPIO-siRNA complexes most probably occurred by adsorptive-mediated endocytosis, which is triggered by electrostatic interactions between the negatively charged plasma membrane and the positively charged complexes. Targeting of the SPIO-siRNA complexes specifically to cancer cells by incorporating a ligand to the receptors overexpressed in the plasma membrane of cancer cells can offer at least three advantages. First, it switches the mechanism of cellular internalization toward more efficient receptor-mediated endocytosis. Second, specific targeting to cancer cells prevents rapid clearance of the siRNA cationic complexes by liver, spleen, and kidney after systemic administration [52, 184]. Third, the delivery of therapeutic payload specifically to cancer cells limits adverse side effects of the treatment on healthy organs by changing its organ distribution toward the preferential accumulation in the tumors [52, 114, 178]. Consequently, in the present study we developed and characterized tumor-targeted superparamagnetic iron oxide nanoparticles-dendrimer complexes for simultaneous delivery specifically to tumor cells of siRNA and MRI-contrast agents. Therefore, the proposed complex multifunctional drug delivery platform can be used for

simultaneous suppression of cellular resistance by siRNA and MRI imaging of the system itself, and primary tumor or metastases. Experimental data show the following advantages of the proposed delivery system.

It is well-known that siRNA complexes should have an optimal size and proper shape for effective gene delivery because that often governs the transfection efficiency, cytotoxicity, and tissue targeting of an entire system *in vivo* [184].

Generally, in order to enable its effective penetration into tissue, the size of gene delivery vehicles should not exceed 250 nm [185], although the optimal size of the particles is still under debate. Direct measurements by several independent approaches determined that the size of complexes developed in the present study was approximately 200 nm (with complexated siRNA). The nanoparticles were compact and close to spherical shape. Consequently, based on our previous data, one could expect that such dendrimer-based systems will provide for an efficient delivery of its payload into cancer cells [51, 52, 127]. Further investigations confirmed this suggestion.

Cytotoxicity of gene transfection vectors including viral vectors, inorganic nanoparticles, cationic liposomes, and polymeric cations is a major barrier for their efficient use for the delivery of therapeutic genes [163]. Recently, Omidi *et al.* [186] demonstrated that PPI dendrimers can intrinsically alter the expression of many endogenous genes, the nature and extent of which were dependent on the dendrimer generation, and cell type. Although cytotoxicity of a nanocarrier itself is not an issue for the delivery of anticancer

drugs with much more higher cytotoxicity, we found that the proposed targeted and nontargeted SPIO-PPI G5 vehicles alone and in combination with siRNA possessed low cytotoxicity. Moreover, a mixture of SPIO with PPI G5 dendrimers alone without siRNA did not influence the expression of the targeted *BCL2* gene. Such low toxicity of the modified siRNA complexes makes them attractive for *in vivo* delivery of nontoxic compounds. Consequently, similar drug delivery systems can be used for applications other than cancer chemotherapy.

It is known that siRNA complexes are usually easily opsonized and removed from the circulation long prior to completion of their main function [187, 188]. Chemical modification of siRNA delivery vector with certain synthetic polymers, such as PEG, is the most frequent way to increase the *in vivo* longevity in the systemic circulation of siRNA delivery vectors. The layer of hydrophilic polymer (in most cases PEG) sterically hinders interactions of blood components with the positively charged surface of siRNA complexes and enhances their stability in the blood stream [52, 189, 190]. However, simultaneously while improving the pharmacokinetics, PEGylation usually limits cellular internalization *in vivo* (stealth effect) [52]. It is known that neutral surface charge of PEGylated siRNA complexes limits their interactions with a negatively charged cell membrane when compared with positively charged non-modified siRNA complexes [52]. To overcome these obstacles, the modification of sterically stabilized siRNA delivery carriers with cell targeting ligands is usually used in order to enhance its transfection activity [52, 127]. The different targeting moieties including, galactose, folate, RGD-

peptide and antibodies were examined for the delivery of DNA and siRNA [160, 189]. Recently, we found that the receptor for LHRH is overexpressed in many types of human cancer cells and was not detectably expressed in healthy human visceral organs [113, 177]. Furthermore, our previous findings show that the use of the LHRH peptide for the targeting of a polymeric anticancer drug delivery system to cancer cells substantially limits its adverse side effects on healthy tissues and significantly enhances the antitumor efficacy of the anticancer drug [114]. Therefore, based on these results we selected the synthetic analog of LHRH peptide as a targeting moiety to enhance the internalization of the developed siRNA delivery system specifically by cancer cells. The results of the *in vitro* and *in vivo* experiments of this tumor-targeted system showed that an incorporation of LHRH peptide substantially improved cellular internalization of siRNA, increased its transfection efficiency, and enhanced the antitumor activity of drug.

Our data clearly show that the combinatorial delivery of siRNA with anticancer drug substantially enhanced the efficiency of chemotherapy leading to the more significant limitation of the tumor growth. Therefore, it is important to deliver siRNA inside tumor cells simultaneously with an anticancer drug. The delivery of siRNA requires an appropriate carrier because naked siRNA is unstable in the blood stream and poorly penetrates cells. The proposed in the present research delivery system significantly improves the stability of siRNA in plasma and provides for its efficient cellular internalization.

In addition, an incorporation of a tumor-targeting moiety (LHRH peptide) into the DDS permits the delivery of siRNA specifically into tumor cells further enhancing antitumor effects of the drug and limiting adverse side effects of the treatment on healthy organs [114, 178, 179].

5.5 Conclusions

In summary, the designed siRNA delivery vector based on SPIO nanoparticles modified with PPI G5 dendrimers and PEG combines the cell-targeted selectivity with the specificity of siRNA. The modular chemical design of the proposed system allows for the substitution of used cancer targeting moiety with other ligands, or combinations of ligands, to selectively target other type of cancer cells. The results obtained open new perspectives for the development of targeted multifunctional siRNA delivery vectors capable of *in situ* monitoring of therapeutic responses of the RNA interference.

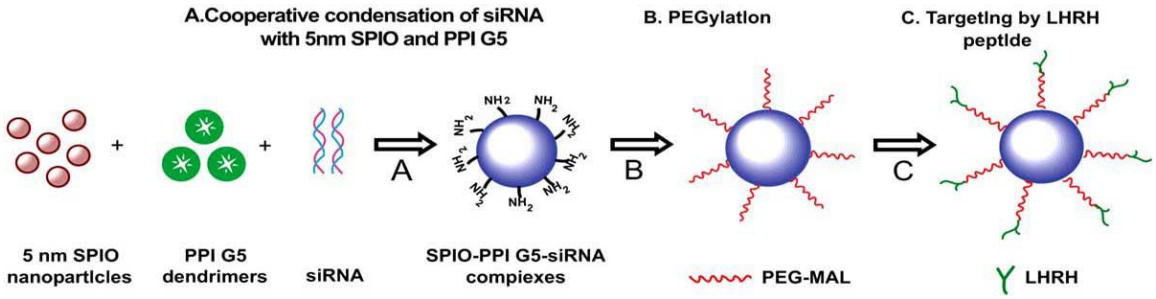

Figure 5.1 The preparation of tumor-targeted, stable siRNA nanoparticles. (**A**) Cooperative condensation of siRNA with 5 nm SPIO nanoparticles and PPI G5 dendrimers. (**B**) PEGylation. (**C**) Conjugation of LHRH peptide to the distal end of the PEG layer.

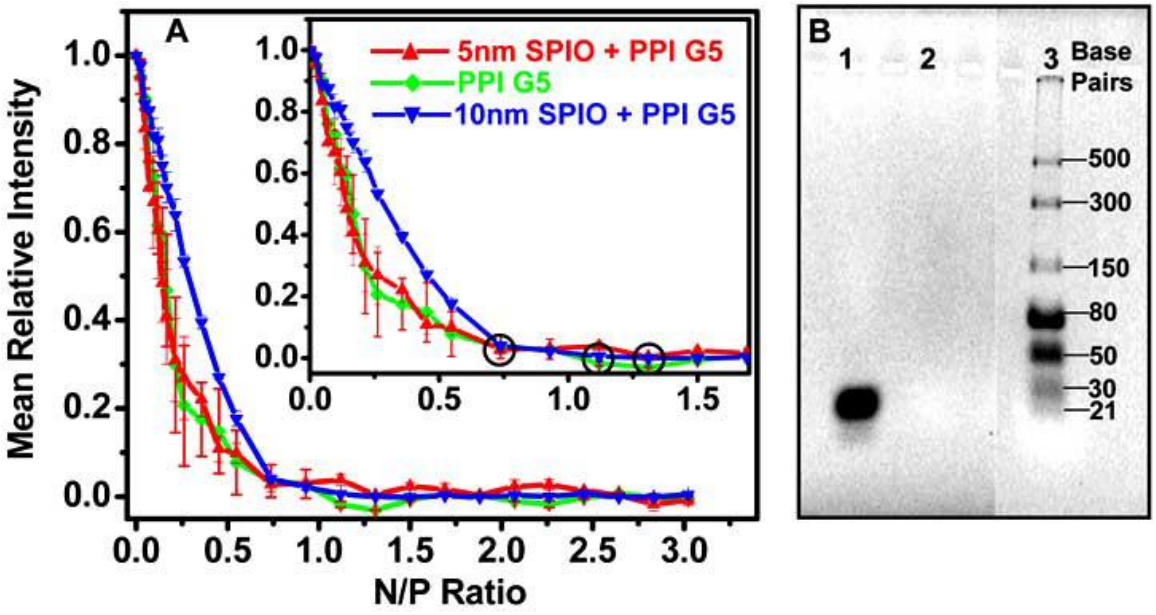

Figure 5.2 (**A**) siRNA complexation efficiency of SPIO nanoparticles and PPI G5 dendrimer evaluated by the ethidium bromide dye displacement assay. Figure inset shows enlarged portions of the curves in the vicinity of N/P ratios which represent the apparent ends of complexation. The circles in the enlarged curves highlight the N/P ratios corresponding to the apparent end of siRNA complexation by different complexation agents. Means ± SD are shown. (**B**) Typical agarose gel electrophoresis image representing siRNA complexation efficiency by mixture of 5 nm SPIO nanoparticles and PPI G5. The gel was stained with ethidium bromide. (1) Free siRNA (control); (2) Mixture of 5 nm SPIO with PPI G5 and (3) Double stranded RNA ladder.

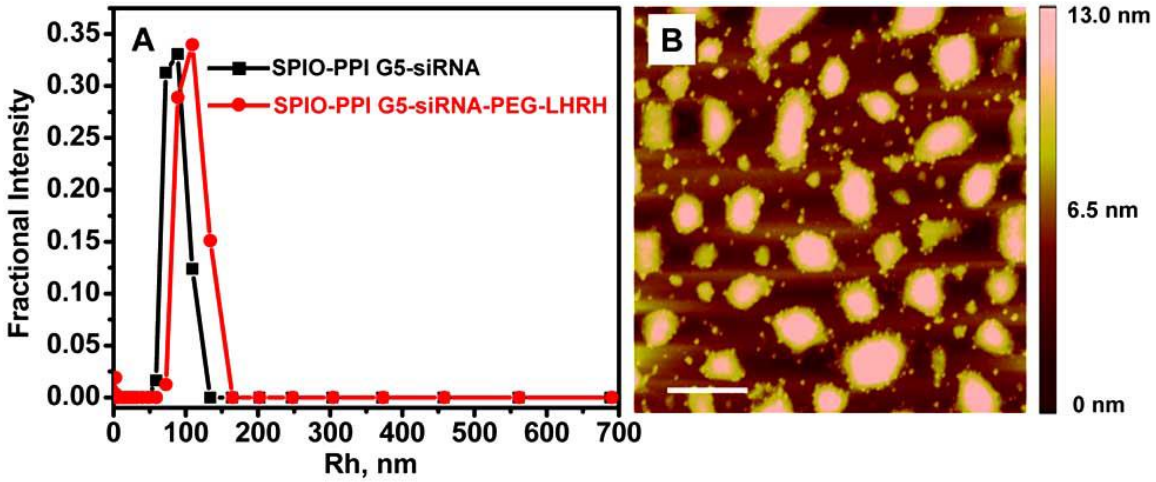

Figure 5.3 (**A**) The representative curves of the size distribution of 5 nm SPIO-PPI G5-siRNA complexes prior and after modification with PEG and targeting LHRH peptide measured by DLS. Rh is hydrodynamic radius. (**B**) Representative atomic force microscope image of the nanoparticles formed as the result of siRNA complexation with mixture of SPIO and PPI G5. Scale bar is equal to 400 nm.

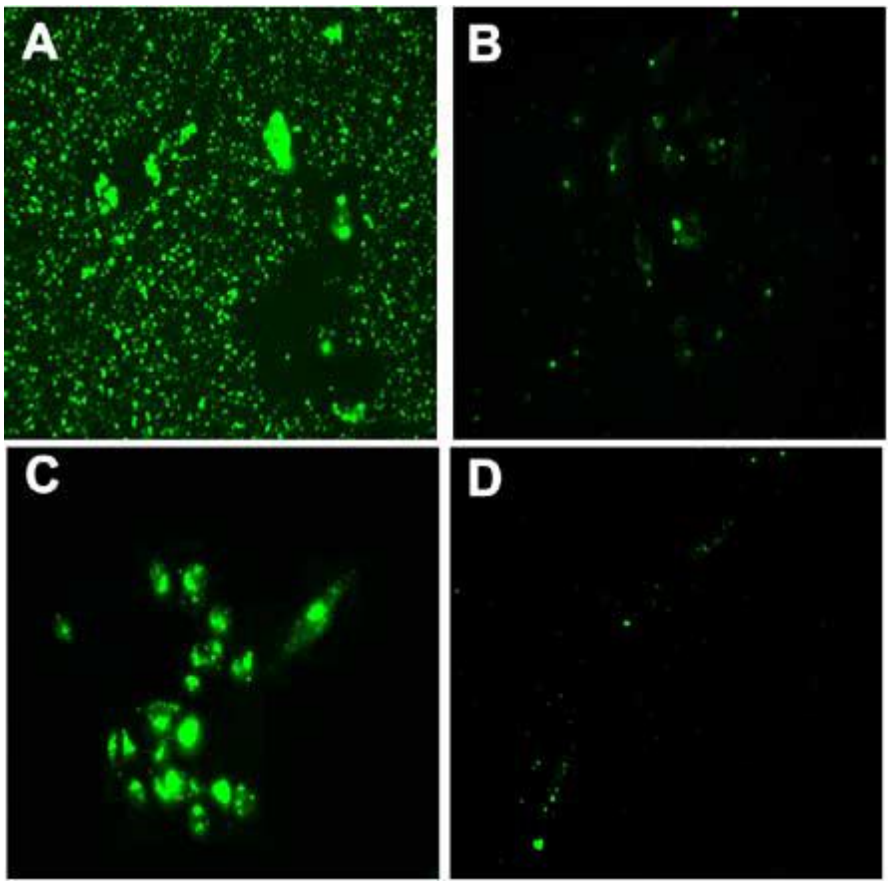

Figure 5.4 Representative fluorescence microscopic images of (**A**) SPIO-PPI G5-siRNA; (**B**) SPIO-PPI G5-siRNA-PEG and (**C, D**) SPIO-PPI G5-siRNA-PEG-LHRH complexes after 24 h of incubation with LHRH-positive A549 (**A-C**) and LHRH-negative SKOV-3 (**D**) cancer cells. siRNA was labeled with 6-FAM Green.

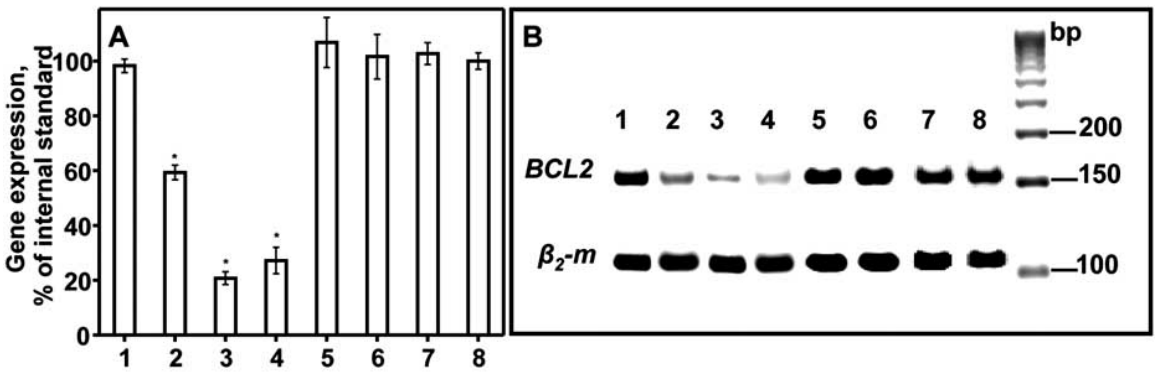

Figure 5.5 Typical image of RT-PCR products and expression of the *BCL2* gene in human A549 (1-6) and SKOV-3 (7, 8) cancer cells. A549 cells were treated with (1) medium (control); (2) SPIO-PPI G5-siRNA-PEG; (3) SPIO-PPI G5-siRNA; (4) SPIO-PPI G5-siRNA-PEGLHRH; (5) SPIO-PPI G5; (6) SPIO-PPI G5-siRNA (scrambled). SKOV-3 cancer cells were treated with (7) SPIO-PPI G5-siRNA-PEGLHRH and (8) medium (control). Gene expression was calculated as a ratio of band intensity of studied gene to that in internal standard (β*2- m,* β*2-microglobulin*). Means ± SD are shown.

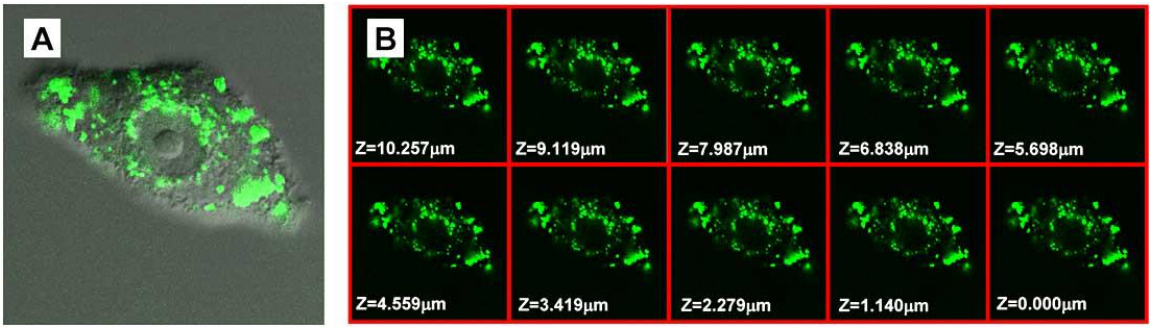

Figure 5.6 Representative confocal microscopy images (light + fluorescence) of A549 human cancer cells incubated for 24 h with SPIO-PPI G5-siRNA-PEG-LHRH (**A**) and z-series from the top (z=10.257 µm) to the bottom (z=0 µm) of the single cell (**B**).

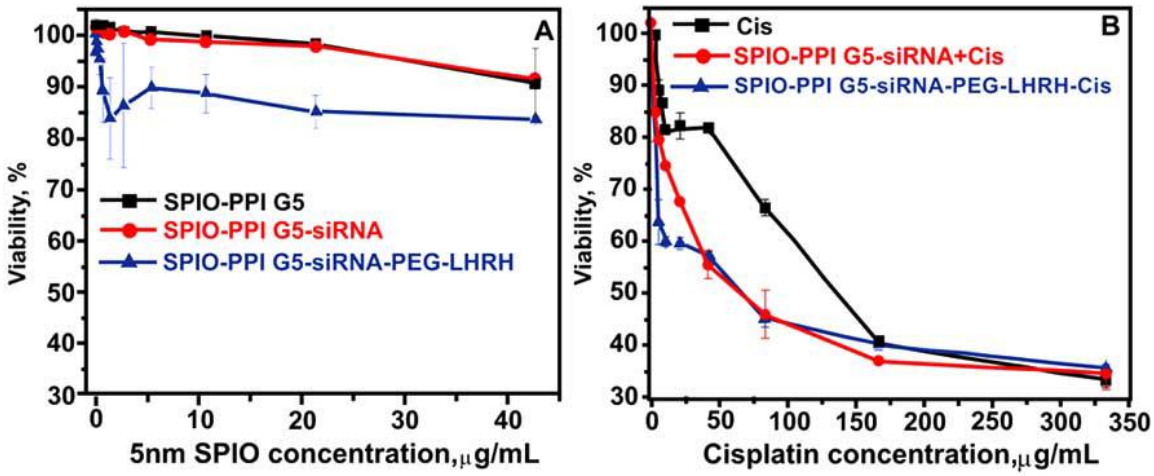

Figure 5.7 Cytotoxicity of (**A**) SPIO-PPI G5; SPIO-PPI G5-siRNA; SPIO-PPI G5-siRNA-PEG-LHRH complexes and (**B**) Cisplatin; SPIO-PPI G5-siRNA + CIS; SPIO-PPI G5-siRNA-PEG-LHRH + CIS against A549 human cancer cells. Means ± SD are shown.

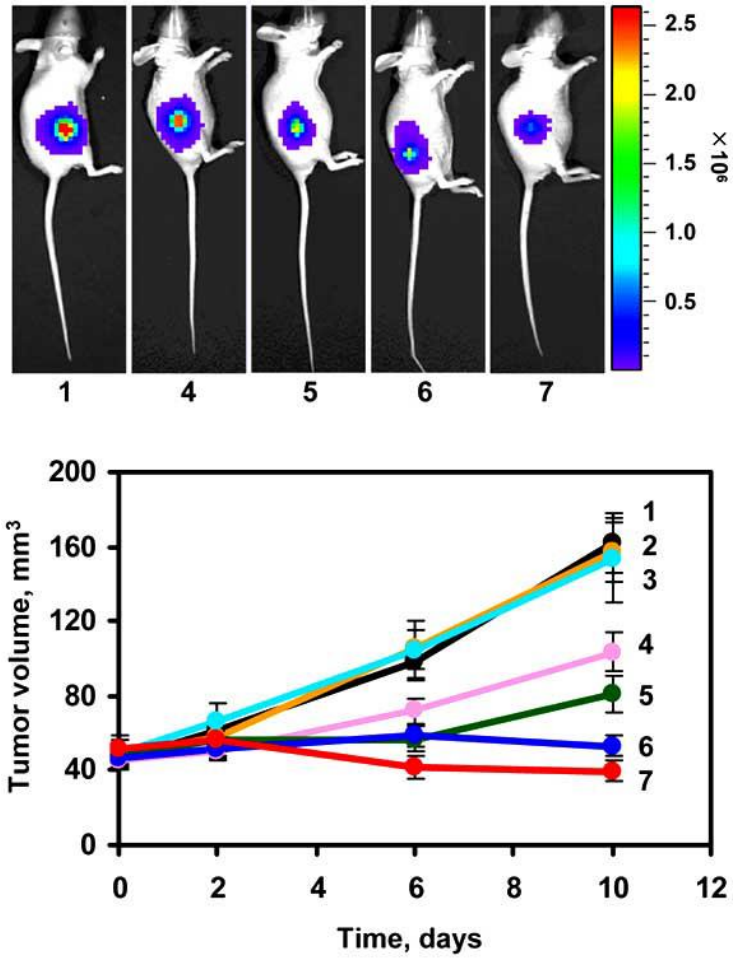

Figure 5.8 Antitumor activity of different formulations. Upper panel: typical bioluminescent images of mice bearing subcutaneous tumor xenografts of human A549 cancer cells transfected with luciferase. Images were taken using the IVIS imaging system (Xenogen) in anesthetized animals at the end of the experiment. Bottom panel: Changes of tumor volume during the treatment. Mice were treated 3 times within 10 days with the following formulations: (1) Control (saline); (2) LHRH; (3) siRNA; (4) CIS; (5) SPIO-PPI-G5 + CIS; (6) SPIO-PPI-G5-siRNA + CIS; (7) LHRH-PEG-SPIO-PPI-siRNA + CIS. Means ± SD are shown.

6 TUMOR TARGETED QUANTUM DOT-MUCIN 1 APTAMER-DOXORUBICIN CONJUGATE FOR IMAGING AND TREATMENT OF CANCER

6.1 Introduction

Ovarian cancer is one of the most common gynecological malignancies in industrialized nations. The lifetime risk for American women is 1.7%. Ninety percent of ovarian cancer is of epithelial origin. Eighty to ninety percent of cases occur in patient older than age forty [191, 192].

Deaths from ovarian cancer account for over half of cancer deaths in women between ages fifty-five and seventy-four. The five year survival rate is 94.6% for women with localized disease, 79% for those with regional disease, and 28.2% for patients with distant stage disease. The overall five year survival rate is about 50%. This prognosis is correlated with the stage at the time of diagnosis [191].

The etiology of ovarian cancer has not been fully deciphered. Possible links include the environment, diet, reproduction, endocrine, viral, and hereditary. Although most cases of ovarian cancer develop sporadically, 10-20% of cases have genetic components [193]. Certain genetic patterns and chromosomal abnormalities are the strongest risk factors for ovarian cancer to date [191, 193]. There is increased risk for ovarian cancer if two or more first degree relatives have ovarian cancer [191]. Women with *BRCA1* tumor suppressor mutations have increased incidence ovarian cancer [191, 193, 194]. *BRCA1*

mutation is found in 90% of genetically related ovarian cancer and in 10% of sporadic ovarian cancers. *BRCA2* is also involved in the development of ovarian cancer, but is not as prevalent as *BRCA1*.

There is strong evidence that the use of oral contraceptives and pregnancies can reduce the incidence of ovarian cancer. These two factors show a correlation between decreased risk of ovarian cancer and decreases ovulation [193]. Hormone replacement therapy has not been shown to decrease the risk of ovarian cancer.

Ovarian cancer patients typically have vague signs and symptoms leading to delayed diagnosis [194]. Symptoms include abdominal or pelvic discomfort, nausea, dyspepsia, difficulty eating, quick satiety, urinary frequency, diarrhea or constipation, and bloating. The signs of ovarian cancer are palpable abdominal or pelvic mass, lymphadenopathy, irregular vaginal bleeding, and ascites.

The aim of screening tests is to diagnose the disease when it is at a localized and curable stage thereby increasing patient survival [191, 194]. Because the prognosis of ovarian cancer is correlated with the stage at diagnosis, screening tests have a valuable role in early detection. Current screening tests are physical examination, cancer antigen 125 (CA 125) measurement, and transvaginal ultrasound. Physical examination is of limited value in asymptomatic women. Its sensitivity and selectivity is not well documented. CA 125 if a high molecular weight epitope on a mucin protein shed by malignant cells. Over 85% of patients have a CA 125 level greater than 35 units/mL. However, 6% of

normal women have CA 125 level over 35 units/mL. Despite this figure, high CA 125 levels continue to be associated with increased incidence of ovarian cancer. Transvaginal ultrasound is a safe, efficient, and acceptable screening test for patients. Complex or solid patterns are of concern when performing transvaginal ultrasound whereas hypoechogenic or cystic patterns are of no concern. It is vital to consider that during the menstrual cycle, there are cyclic changes in ovary size. It is necessary to repeat an abnormal ultrasound.

In a recent study by Visintin *et al.* [195], six biomarkers were used to screen for ovarian cancer. The researchers used the following biomarkers: leptin; prolactin; osteopontin (OPN); insulin-like growth factor 1 (IGF-1); macrophage migration inhibitory factor (MIF); and CA-125. This research was spurred because CA-125 screening has a sensitivity of less than 60% in early ovarian cancer. It is possible to have higher cure rates if women are screened and ovarian cancer is found in the earliest stages when it is curable. Screening of these six biomarkers yielded a sensitivity of 95.3% and a specificity of 99.4%. This is a significant improvement over the current CA-125 ovarian cancer screening test.

Standard treatment of ovarian carcinoma involves aggressive surgery followed by chemotherapy. Micronodular and floating tumor colonies, which are spread within the peritoneal cavity, cannot be adequately treated by surgery or radiation and require extensive chemotherapy.

In most cases, the first step to treating ovarian cancer is surgery (Fig. 6.1). Stage I is a low level cancer in which the tumor is limited to the ovaries. Patients with Stage I disease are usually cured; however, due to lack of symptoms, most patients are not diagnosed at this stage.

Cytoreductive surgery is performed for stage II, III, and IV cancers. The goal is to remove as much of the tumor as possible. This is followed by chemotherapy to kill any remaining tumor cells and possible metastases. The first line chemotherapy is a combination of a taxane and carboplatin. Carboplatin is a drug that is classified as a platinum agent. Platinum agents are the drugs of choice in treating ovarian cancer. Stage I patients may or may not receive chemotherapy; this is based on the clinician's decision about whether the cancer is likely to return. The chemotherapy regimen is longer for patients with stage II-IV disease. Chemotherapy typically is given for 6-8 cycles.

Neoadjuvant therapy is used for patients with bulky stage III or IV disease. Chemotherapy is given prior to and after surgery. Chemotherapy prior to surgery helps to reduce the size of tumor by killing a large number of tumor cells. This allows the tumor to be more easily resectable. Chemotherapy is then administered again to kill any remaining cancer cells.

Radiation therapy was widely used for treatment of ovarian cancer in the past. Due to severe adverse side effects such as high incidence of nausea and diarrhea, bone marrow

suppression, and toxicities to normal organs and tissues, and equal efficacy of chemotherapy, radiation therapy fell out of favor for use in ovarian cancer patients. There has been renewed interest in utilizing radiation therapy in ovarian cancer due to the high rate of recurrence. Researchers believe that radiation therapy as consolidation after optimal debulking surgery and chemotherapy may decrease ovarian cancer recurrence.

Several approaches are being used for chemotherapy of ovarian cancer including the treatment with platinum derivatives [196, 197] and doxorubicin (DOX) delivered by different nanocarriers, such as liposomes (Doxil) [198-200], polymers [197, 201], gold nanoparticles [202], mesoporous silica films [203], and dendrimers [204]. Although most patients respond effectively to initial therapy, the efficiency of the treatment usually rapidly decreases because of the development of cancer cellular resistance against chemotherapy. The development of such resistance and high recurrence rates of ovarian carcinoma represent a challenge for the treatment of this disease. Ovarian cancer patients that do not respond to initial chemotherapy or relapse after achieving a response are generally incurable [205]. In order to enhance the drug uptake by resistant ovarian cancer cells, increase the efficiency of treatment and substantially limit adverse side effects of high dose chemotherapy, a targeting of anticancer drug(s) specifically to tumor cells can be employed [206]. Consequently, the development of novel drug delivery vehicles capable to deliver an anticancer drug specifically to ovarian cancer cells

and to effectively penetrate inside resistant tumor cells releasing their payload is an important task in enhancing the treatment of ovarian carcinoma.

Quantum dots (QD) are newer nanoparticles that have garnered extensive investigation as potential drug delivery vehicles. QD represent nanometer size semiconductor particles that are gaining popularity as fluorescent markers and delivery vehicles. QD inherently possess numerous advantages over traditional fluorescent dyes such as increased photostability, higher brightness, and narrow fluorescence spectra [91, 96]. QD can be designed to have emission peaks at different wavelengths by adjusting their size. This customization allows QD to be produced for specific functions such as Fluorescence Resonance Energy Transfer (FRET), in which a specific emission wavelength can transfer energy to drug molecules or photosensitizers. Consequently, FRET phenomenon can be potentially used for the development of novel therapeutic approaches for cancer treatment [207]. Furthermore, functionalized QD are versatile and can be modified with biomolecules such as antibodies, small molecules, peptides, and aptamers [91, 96]. Due to these properties, QD can be utilized to design multifunctional systems for simultaneous imaging and delivery of therapeutic agents, a task that represents a substantial challenge for other types of nanocarriers. Recent reports showed that QD can be used in photodynamic and radiation therapy [97], which would make QD a prospective therapeutic drug carrier since radiation therapy is employed as an adjunct for the treatment of many types of cancers. In addition,

quenching of fluorescence of QD by a cargo due to FRET would allow for monitoring the attachment and release of QD payload.

Mucin 1 (MUC1) cell surface associated mucin is mutated and overexpressed on the surface of many cancer cells [116]. Aberrant forms of MUC1 are overexpressed in more than 90% of late stage epithelial ovarian cancers and associated metastatic lesions [119]. Consequently, specific targeting of drug delivery system to this mutated mucin has a potential to improve internalization of an anticancer drug by resistant ovarian cancer cells and limit adverse side effects of chemotherapy on healthy organs. The design and characterization of a DNA aptamer, an oligonucleotide, specific for MUC1 was previously reported [122]. The authors demonstrated that the aptamer had a higher binding affinity for extracellular mutated mucin and lower immunogenicity than monoclonal antibodies. Therefore, it is logical to assume that the use of such aptamer as a targeting moiety and penetration enhancer specific to ovarian cancer cells may improve the efficacy of treatment and imaging of both primary and metastatic ovarian tumors.

Besides the specific tumor targeting, a cancer specific drug delivery system should protect an anticancer drug from degradation during its journey in the systemic circulation and provide for an effective release of its payload inside the cancer cells. A pH-sensitive hydrazone bond is often being used to conjugate a delivered substance with a vehicle to achieve required stability of payload in mildly basic or neutral

extracellular environment and its release under acidic conditions inside endo- or lysosomes after the internalization of an entire system by cancer cells [208-212].

Based on the aforementioned consideration, we hypothesize that a drug delivery system that consists of (1) QD as a carrier, (2) DOX as an anticancer drug conjugated to QD via a pH-sensitive hydrazone bond and (3) aptamer targeted to mutated MUC1 mucin as a targeting moiety/penetration enhancer will be exceptionally effective for imaging and treatment of drug resistant ovarian malignances. Such system can form the basis for a multi-pronged attack on resistant ovarian cancer and metastases by simultaneously fulfilling the following tasks: (1) increasing penetration of anticancer drug into ovarian cancer cells; (2) preventing adverse side effects of chemotherapy by targeting the entire system specifically to primary ovarian cancer cells; (3) effective imaging of primary and metastatic cancer cells; (4) protection of drug in systemic circulation and release inside cancer cells; and (5) monitoring drug release in targeted ovarian cancer cells. The present study is aimed at testing this hypothesis.

6.2 Materials and Methods

6.2.1 Materials

Carboxyl terminated quantum dots were purchased from eBioscience (San diego, CA). The custom, mucin 1 receptor specific aptamer with the sequence, 5’-GCA-GTT-GAT-CCT-TTG-GAT-ACC-CTG-G-3’, was synthesized by Invitrogen (Carlsbad, CA). Doxorubicin

hydrochloride, 1-ethyl-3-(3-dimethylaminopropyl) carbodiimide (EDC),*N*-hydroxysuccinimide (NHS), hydrazine monohydrate, RPMI 1640 medium, and penicillin/streptomycin antibiotics were ordered from Sigma-Aldrich (St. Louis, MO). Fetal bovine serum was purchased from Fisher Chemicals (Fairlawn, NJ). Dimethy sulfoxide was purchased from Acros Organics (Morris Plains, NJ). Dulbecco's phosphate buffered saline (DPBS) was purchased from Lonza, Inc. (Mapleton, IL).

6.2.2 Synthesis of Quantum Dot-MUC1 Aptamer Conjugates

Carboxyl terminated quantum dots (QD-COOH) with an emission peak at 490 nm (eBioscience, Inc., San Diego, CA) were used as carriers. One nanomole of QD-COOH was added to 1225 µL of 10 mM borate buffer (pH = 7.4) and mixed well by stirring. After this, 200 µL of 500 µM 5'-amine terminated MUC1 DNA aptamer (Invitrogen, Carlsbad, CA) were added to the reaction mixture under continued stirring. Further, 50 µL of 50 mM 1-ethyl-3-(3-dimethylaminopropyl) carbodiimide (EDC) (Sigma-Aldrich, St. Louis, MO) and 25 µL of 25 mM *N*-hydroxysuccinimide (NHS) (Sigma-Aldrich, St. Louis, MO) were added to the reaction mixture and incubated with gentle stirring for 2 h at room temperature protected from light. After the incubation, the mixture was centrifuged using Microcon YM-30 Centrifugal Filter Unit (Millipore, Billerica, MA) with molecular weight cutoff of 30 kDa for 10 min at 13,000 rpm for 5 buffer exchanges using 50 mM borate buffer (pH = 8.3) and reconstituted in 1 mL H_2O.

6.2.3 Synthesis of Quantum Dot-MUC1 Aptamer-Doxorubicin Conjugates

After the purification of the quantum dot-MUC1 conjugate by centrifugation, the solution was concentrated to 500 µL. Afterwards, 500 µL anhydrous dimethyl sulfoxide (Acros Organics, Morris Plains, NJ), 50 µL of 50 mM EDC, 25 µL of 25 mM NHS, 40 µL hydrazine monohydrate (Sigma-Aldrich, St. Louis, MO, 64% v/v) were added to the reaction mixture and incubated for 3 h at room temperature with gentle stirring. After the incubation, the reaction solution was diluted to 3 mL with H_2O and dialyzed by the centrifugation as described above for 10 min at 13,000 rpm for 3 exchanges with H_2O. The retentate was concentrated to 500 µL using anhydrous dimethyl sulfoxide (DMSO, Acros Organics, Morris Plains, NJ). Then, 100 µL of doxorubicin hydrochloride (10 mg/mL, Sigma-Aldrich, St. Louis, MO) and 600 µL anhydrous DMSO were added and allowed to react for 48 h at room temperature under gentle stirring after adding a few drops of acetic acid (Fisher Scientific, Pittsburg, PA) to act as a catalyst. At the end of the incubation, the reaction solution was diluted to 3 mL using H_2O, centrifuged as described above and concentrated to 1 mL using H_2O.

6.2.4 Synthesis of Quantum Dot-Doxorubicin Conjugates

One nanomole of QD-COOH was added to 875 µL of anhydrous dimethyl sulfoxide, 50 µL of 50 mM EDC, 25 µL of 25 mM NHS, and 40 µL of hydrazine monohydrate (64% v/v) and was allowed to react for 3 h at room temperature with gentle stirring and diluted to 3 mL using H_2O. The solution was dialyzed by the centrifugation as described above for

10 min at 13,000 rpm for 3 exchanges of H_2O and concentrated to 500 µL. After this, 100 µL of DOX (10 mg/mL) and 600 µL of anhydrous DMSO were added to the solution; a few drops of acetic acid were added as a catalyst and allowed to react for 48 h at room temperature under gentle stirring. The reaction mixture was diluted to 3 mL with H_2O, dialyzed by the centrifugation as described above for 3 exchanges of H_2O and concentrated to 1 mL with H_2O.

6.2.5 Determination of Doxorubicin Loading

After removal of free DOX by a centrifugation dialysis, the absorbance of the QD-MUC1-DOX conjugate at 492 nm was measured using a microplate reader (GENios, Tecan US, Inc., Durham, NC). QD-MUC1 solution with the same concentration of QD as in the QD-MUC1-DOX conjugate was used as a reference. DOX concentration in the conjugate was calculated from a standard curve of DOX absorbance created by measuring the absorbance of several predefined DOX concentrations.

6.2.6 Hydrolytic Release of Doxorubicin

In order to determine the rate of DOX release from QD conjugates, the conjugate was incubated in an acidic environment. To this end, a quantum dot-doxorubicin conjugate was dissolved in Dulbecco's phosphate buffered saline (DPBS, Lonza, Inc., Mapleton, IL) with pH adjusted to 5. At pre-determined time intervals, small samples were taken from the bulk solution. Released free DOX was eliminated by a centrifugation dialysis using

Microcon YM-30 Centrifugal Filter Unit with molecular weight cutoff of 30 kDa for 10 min at 13,000 rpm for 3 exchanges of H_2O. The remaining concentration of DOX in the sample was determined by measuring the absorbance at 492 nm using the standard curve and the amount of DOX released from the samples was determined by comparing DOX concentration in the sample with an initial concentration in the intact conjugate.

6.2.7 Cell Line

The A2780/AD multidrug resistant human ovarian carcinoma cell line was obtained from T. C. Hamilton (Fox Chase Cancer Center, Philadelphia, PA). Cells were cultured in RPMI 1640 medium (Sigma, St. Louis, MO) supplemented with 10% fetal bovine serum (Fisher Chemicals, Fairlawn, NJ) and 1.2 mL/100 mL penicillin–streptomycin (Sigma, St. Louis, MO). Cells were grown at 37°C in a humidified atmosphere of 5% CO_2 (v/v) in air. All experiments were performed on cells in the exponential growth phase.

6.2.8 Cytotoxicity Assay

The cellular cytotoxicity of QD, MUC1 aptamer-QD, free DOX and all drug-QD-aptamer conjugates were accessed using a modified MTT (3-(4,5-dimethylthiazol-2-yl)-2,5-diphenyltetrazolium bromide) assay as previously described [138, 182, 213].

6.2.9 Cellular Internalization and Localization

Cellular uptake of non-modified QD, MUC1 aptamer-QD conjugate and QD-MUC1-DOX conjugates was studied by a confocal microscopy. To assess intracellular distribution of the substances, 12 optical sections, known as a z-series, were scanned sequentially along the vertical (z) axis from the top to the bottom of the cell.

6.2.10 Animal Tumor Model, *in vivo* Imaging and Organ Distribution

An animal model of human ovarian carcinoma xenografts was used as previously described [21, 114, 178, 179]. Briefly, A2780/AD multidrug resistant human ovarian carcinoma cells (2×10^6) were subcutaneously transplanted into the flanks of female athymic nu/nu mice. When the tumors reached a size of about 0.2–0.3 cm^3 (15–20 days after transplantation), mice were treated intravenously with non-modified QD and tumor-targeted by MUC1 aptamer QD conjugate (QD-MUC1). Animals were anesthetized with isoflurane using the XGI-8 Gas Anesthesia System (Xenogen, Alameda, CA). Fluorescence of injected QD was visualized using IVIS imaging system (Xenogen, Alameda, CA) 24 h after the treatment. Visible light and fluorescence images were taken and overlaid using the manufactures software to obtain composite images.

6.2.11 Statistical Analysis

Data obtained were analyzed using descriptive statistics, single factor analysis of variance (ANOVA) and presented as mean value ± the standard deviation (SD) from four to eight independent measurements in separate experiments. The comparison among

groups was performed by the independent sample Student's *t*-tests. The difference between variants is considered significant if $P < 0.05$.

6.3 Results

Carboxyl-terminated QD were conjugated with MUC1 aptamer and DOX (Fig. 6.2). The MUC1 aptamer was modified with a 5'- primary amine which was conjugated to the carboxyl groups on the surface of QD forming an amide bond. Conjugation of aptamer onto QD was confirmed using gel electrophoresis (results not shown). Approximately five aptamers per quantum dot were attached. On the next step, DOX was loaded onto the QD-aptamer conjugate. In order to provide the release of DOX in the acidic environment inside cancer cells, the drug was attached to the QD using an acid labile hydrazone bond [214]. DOX absorbance was used to calculate loading the drug onto QD. Using a standard concentration curve, we calculated that approximately 46 DOX molecules were bound per one QD molecule in the QD-MUC1-DOX conjugate.

The absorbance spectrum of DOX and fluorescence emission spectrum of used QD were measured. As can be seen from Fig. 6.3A, normalized DOX absorbance and QD emission spectra overlap. This creates precondition for so called Fluorescence Resonance Energy Transfer (FRET) between QD and DOX and for quenching of QD fluorescence. A direct measurement of fluorescence of naked QD and QD-DOX conjugates under the 360 nm excitation (Fig. 6.3B) confirms quenching of QD fluorescence by FRET mechanism. The release of DOX from QD-DOX conjugate in an acidic environment was studied. A direct

measurement showed that about 35% of bound DOX was released from QD-DOX conjugate after five hours of incubation in an acidic environment (Fig. 6.3C).

Cellular uptake studies were performed and the results were evaluated using confocal microscopy. A minimal uptake of unmodified quantum dots by A2780/AD cells was found (Fig. 6.4). Modification of QD with tumor targeting moiety/penetration enhancer MUC1 aptamer led to the more substantial uptake of QD-MUC1 conjugate by resistant cancer cells. Similarly, strong fluorescent signal was registered inside cancer cells after incubation with QD-MUC1-DOX conjugate. Furthermore, the fluorescence intensity of targeted conjugate containing DOX was even more pronounced when compared with QD-MUC1 conjugate. This fact clearly not only shows enhanced uptake of tumor targeted conjugates but also confirms DOX release from the conjugate inside cancer cells, separation of QD and DOX, restoration of QD fluorescence as a result of stopping fluorescence quenching by FRET after the separation and doubling of fluorescence intensity by simultaneous fluorescence of QD and DOX.

The cytotoxicity of unmodified and modified quantum dots were analyzed by modified MTT (3-(4,5-dimethylthiazol-2-yl)-2,5-diphenyl tetrasodium bromide) assay in DOX-resistant A2780-AD human ovarian cancer cells. The results show no apparent cytotoxicity of unmodified QD and MUC1 aptamer-QD conjugate at tested concentrations (Fig. 6.5). The measurement of IC_{50} dose of free DOX resulted in the relatively high value (~ 4 μM) comparable to that measured more than 10 years ago in

the same cell line [213]. This in turn shows that A2780/AD human ovarian carcinoma cells did not lose their resistance to doxorubicin. Surprisingly, we did not find a statistically significant increase in cytotoxicity after conjugation of low molecular weight DOX to high molecular weight QD. Targeting QD-DOX conjugates specifically to cancer cells led to the statistically significant increase in toxicity and decrease in IC_{50} value. These data correlate well with the results of cellular uptake study.

In vivo organ distribution of targeted and non-targeted QD was carried out in nude mice model of tumor xenografts. Multidrug resistant human ovarian cancer cells, A2780/AD, were implanted subcutaneously above the right hind leg of the mice and allowed to grow. Unmodified quantum dots and tumor targeted quantum dots (QD-MUC1) were injected intraperitoneally. The whole body fluorescent images taken by IVIS system one hour after injection show higher accumulation of the targeted conjugate (QD-MUC1) in the tumor and lower accumulation in other studied organs when compared with the unmodified quantum dot (Fig. 6.6).

6.4 Discussion

In the present study we constructed and evaluated *in vitro* and *in vivo* non-targeted and tumor targeted quantum dot-doxorubicin conjugates. DOX was attached to the QD using an acid labile hydrazone bond [214]. The hydrazone bond is being widely used for the attachment of doxorubicin to structurally and chemically different types of delivery vehicles [214, 215]. However, the specific type of hydrazone bond utilized may have

dramatic effects on the doxorubicin activity. Lee et al. [215] studied acyl hydrazone linkages and hydrazone carboxylate linkages. The hydrazone carboxylate linkages released a derivative of doxorubicin due to an intramolecular cyclization reaction. This derivative did not retain the activity of DOX. In addition, the hydrazone carboxylate linkage was not sufficiently stable at physiological pH. The authors discovered that in the case of acyl hydrazone bonds, DOX is released without any chemical modifications and that the linkage is stable at neutral pH. Based on these findings we used an acyl hydrazone bond to conjugate DOX to quantum dots. Our results show a relatively higher doxorubicin loading efficiency of QD via this bond. It was found that around 46 molecules of DOX were bound per one QD molecule. Using molecular weight of QD and DOX reported by the manufacturers (~ 150 kDa and ~ 580 Da, respectively), one can calculate the loading level equal to 17 wt.%. This demonstrates a relatively high loading capacity of quantum dots comparable with the loading capacity of other carriers. For instance, Prabaharan et al. [202] used gold nanoparticles to deliver doxorubicin and reported a DOX loading level of 17 wt.%. A loading capacity of 14 wt.% was achieved using superparamagnetic iron oxide nanoparticles [79]. Using N-(2-hydroxypropyl)methacrylamide (HPMA) copolymers, Etrych et al. [214] achieved 12 wt.% loading capacity of DOX bound to the polymer via an acid labile hydrazone bond.

The results of fluorescence studies demonstrated quenching of QD fluorescence by FRET between doxorubicin and QD. Fluorescence measurements revealed that QD used in the

present study absorbs light with a wavelength of 390 nm and emits at 490 nm. DOX absorbance spectrum showed that DOX can absorb light with this wavelength. Due to the proximity of DOX and QD in a conjugate, the fluorescence signal of QD is absorbed by DOX, which then can emit a signal at 560 nm. Based on the measured fluorescence spectrum, it is clear that attachment of doxorubicin quenches the QD fluorescence signal. According to the literature data, eight DOX molecules are required to fully quench the fluorescence of one quantum dot [96]. Based on DOX loading registered in the present study, synthesized QD-DOX conjugates exceed this requirement and demonstrated complete quenching of QD fluorescence. It is known that when the molecules that emit and absorb light are separated beyond 10 nm, FRET no longer can occur [216]. Consequently, the release of DOX from the conjugates and its diffusion beyond 10 nm from QD should discontinue FRET and one would be able to register an increase in QD fluorescence and probably a certain decrease in DOX fluorescence. This would allow monitoring of DOX release *in vitro* and *in-vivo* using fluorescent imaging techniques. This in turn increases the significance of the constructed QD-DOX conjugates for both mechanistic studies and monitoring QD-DOX accumulation and internalization in the targeted sites during chemotherapy.

The data obtained in the present study confirmed an efficient release of DOX from QD-DOX conjugates when nearly 35% of loaded drug was released after five hours of incubation of conjugates *in vitro* in an acidic environment. This release rate can be considered as relatively high when compared with that previously measured for a

similar type of hydrazone bond [217]. In that study, approximately 45% of the DOX loaded into polymeric micelles and bound by pH-sensitive hydrazone bonds was released after 24 h of incubation of micelles in acidic conditions. Several factors can potentially be responsible for the registered high rate of DOX release from constructed QD-DOX conjugates. In our system, DOX was attached on the periphery of the conjugates. This may lead to the more favorable exposure of the hydrazone bond to the acidic environment when compared with micelles used in the cited work [217]. Second, the micelles used by the authors were much larger than QD employed in the present study. This may have also hindered the exposure to the acidic environment. It would be premature to transfer these results onto intracellular release of DOX from the conjugates because the conditions in the endosomes and tumor microenvironment are different from simple *in vitro* incubation settings. Nonetheless, the results provide a foundation for an effective delivery of DOX by QD to the tumor and release inside cancer cells. It should also be stressed that the handling and processing of the sample for measurements may have had an insignificant impact on the results because the hydrazone linkage is quite stable in neutral pH and should not have been disturbed by the short centrifugation process. Moreover, our *in vitro* and *in vivo* data clearly confirmed that DOX delivered by tumor targeted QD-MUC1-DOX conjugates accumulated predominately in the tumor and effectively released inside cancer cells. These results also allow us to hypothesize that the release of DOX from the conjugates most probably occurred in an acidic environment inside lysosomes after the

internalization of conjugates by endocytosis and fusion of lysosomes with conjugate-containing endosomes.

Due to the presence in QD cadmium and selenium, which have shown to be toxic when accumulated, toxicity of QD remains a primary concern in their clinical applications. The results show no apparent cytotoxicity of unmodified QD at tested concentrations. The presence of the zinc sulfide shell and polymer or lipid coating dramatically reduced exposure to the toxic quantum dot core [88]. Currently there are no studies evaluating long term toxicities of quantum dots. Studies on short term toxicities (up to 72 h of exposure) have yielded different results. The majority of the studies show that CdSe/ZnS quantum dots have no toxic effects [88]. Although, the low toxicity of drug carriers is not very important for their use in cancer chemotherapy when the carrier is conjugated with highly toxic anticancer drug, our data showed that QD employed in the present study were not toxic in the concentrations used. This forms a basis for their possible applications for the delivery of relatively low toxic drugs for clinical use other than chemotherapy.

Based on our previous data on HPMA copolymer-bound DOX that showed significantly (more than six-folds) lower cytotoxicity of high molecular weight conjugated DOX when compared with low molecular weight free DOX [213], we expected a substantial increase in the IC_{50} dose (decrease in cytotoxicity) for QD-DOX conjugates. Moreover, because QD have substantially higher molecular weight (~ 150 KDa for QD versus

~ 20 KDa for the studied polymeric conjugate) the expected decrease in the toxicity could be even more pronounced. However, no statistically significant difference was found in the present study between the IC_{50} doses for free DOX and QD-DOX conjugates. Such discrepancy between our expectations and the reality confirms higher penetration ability of non-targeted QD-DOX conjugates in multidrug resistant cancer cells and effective DOX release in the intracellular environment. It also suggests that QD-DOX conjugates were internalized by multidrug resistant cancer cells via a pathway different from diffusion (probably by endocytosis) allowing to overcome existing drug efflux pumps overexpressed in these cells [213, 218]. Targeting of QD-DOX conjugates to cancer cells by MUC1 aptamer further increased their cytotoxicity showing a remarkable potential of tumor targeted QD as delivery vehicles for anticancer drugs.

A comparison of *in vivo* images reflecting the biodistribution of non-targeted and tumor targeted QD-DOX conjugates show that both passive and active tumor targeting mechanisms [206] are involved in quantum accumulation within the tumor. The Enhanced Permeation and Retention (EPR) effect is likely the phenomenon responsible for passive targeting of QD-DOX conjugates to tumor. The active targeting was achieved by incorporating the MUC1 specific aptamer into QD-DOX conjugates. Although this aptamer is not well validated, it does enhance the accumulation of QD within the tumor and cancer cells as evidenced by *in vivo* IVIS and *in vitro* confocal imaging. The present experimental data clearly showed that MUC1 aptamer as a tumor-targeting moiety is responsible for a preferential accumulation of QD-MUC1-DOX conjugates in the ovarian

tumor, their effective internalization by cancer cells and release of the drug inside the cells.

6.5 Conclusions

We have demonstrated the design and functionality of tumor targeted quantum dot-based anticancer drug delivery system. The system demonstrated the ability to preferentially target ovarian cancer cells, efficiently released doxorubicin in acidic pH, and had higher toxicity in ovarian cancer cells when compared with free doxorubicin. We also showed that quantum dots have potential as carriers of drugs and as *in vivo* imaging agents. Furthermore, the data confirmed that the MUC1 aptamer may be an effective alternative to conventional targeting agents such as peptides and antibodies.

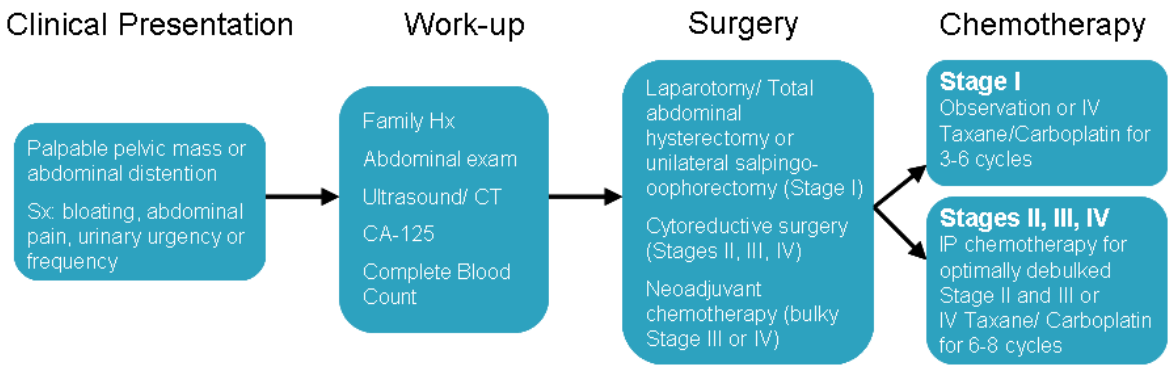

Figure 6.1 Diagnosis, surgery and chemotherapy in treatment of ovarian cancer. This is the typical protocol followed for women who present with ovarian cancer.

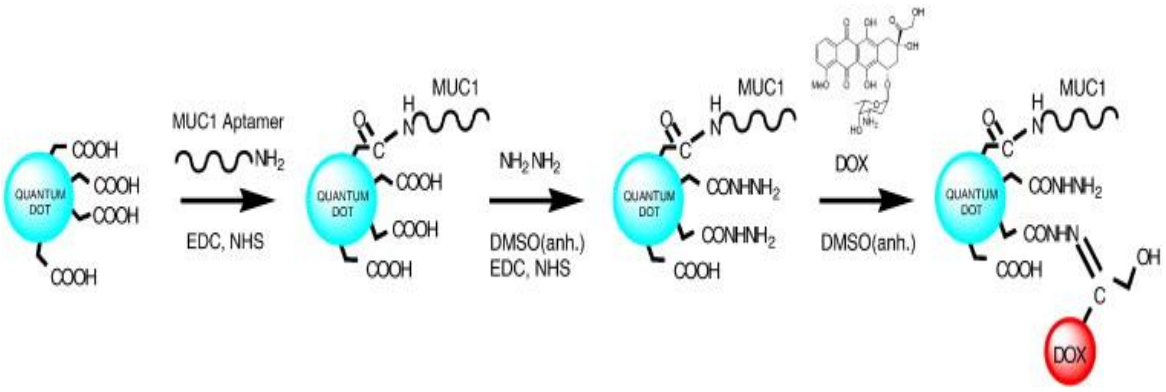

Figure 6.2 Synthesis of quantum dot-MUC1 aptamer doxorubicin (QD-MUC1-DOX) conjugate.

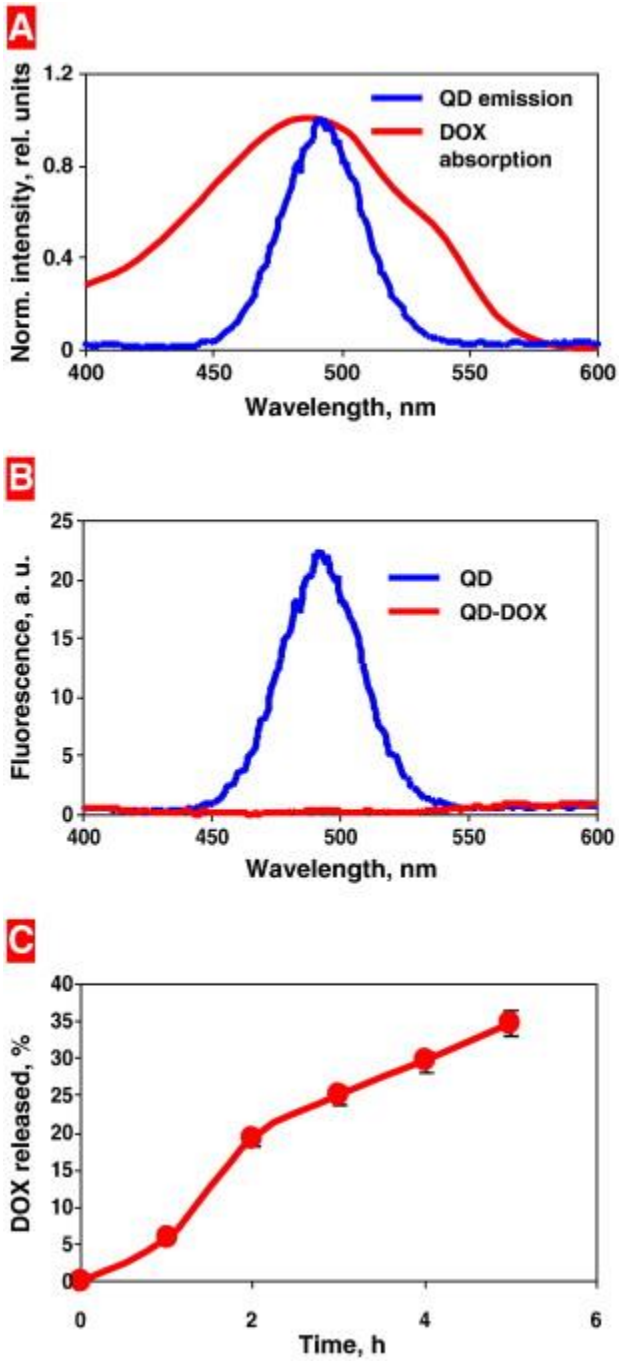

Figure 6.3 Characterization of non-modified quantum dots (QD)-doxorubicin (DOX) conjugates. (A) Overlap of QD fluorescence (blue curve) and DOX absorbance (red curve); (B) quenching of QD fluorescence by DOX; (C) release of DOX from QD-DOX conjugate in an acidic environment. Means ± S.D. are shown.

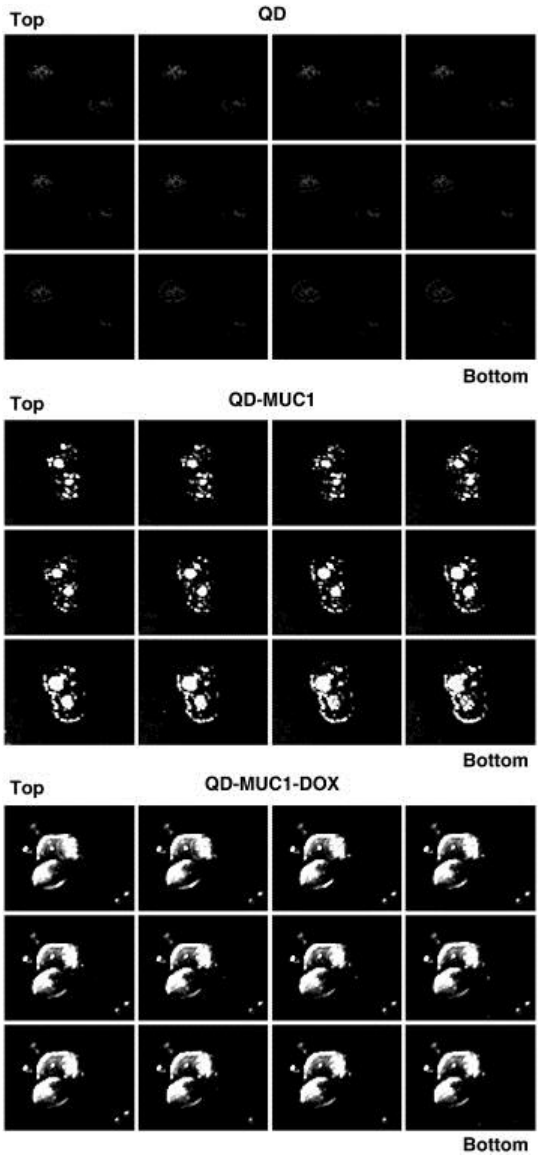

Figure 6.4 Intracellular localization of non-modified quantum dots (QD), cancer cell targeted by MUC1 aptamer QD (QD-MUC1), and MUC1 aptamer QD-DOX (QD-MUC1-DOX) conjugates in multidrug resistant A2780/AD human ovarian carcinoma cells. Representative confocal microscope images of cells incubated for 24 h with substances indicated (z-series, from the top of the cell to the bottom).

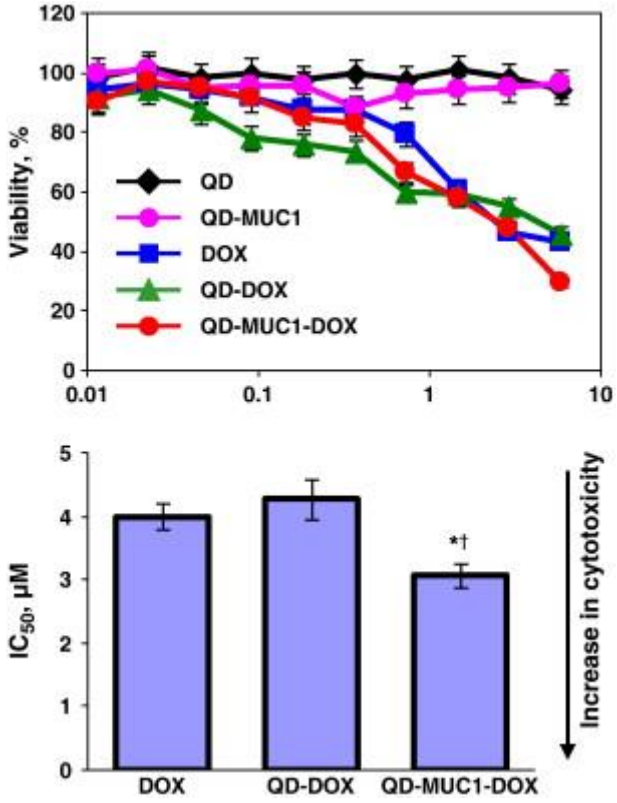

Figure 6.5 Cytotoxicity of different formulations of quantum dots (QD). Multidrug resistant A2780/AD human ovarian carcinoma cell were incubated with the indicated formulations. Upper panel: cellular viability of formulations with and without DOX. Bottom panel: IC_{50} doses of formulations that contain DOX. Means ± SD are shown. *$P < 0.05$ when compared with free DOX.$^{\dagger}P < 0.05$ when compared with free QD-DOX.

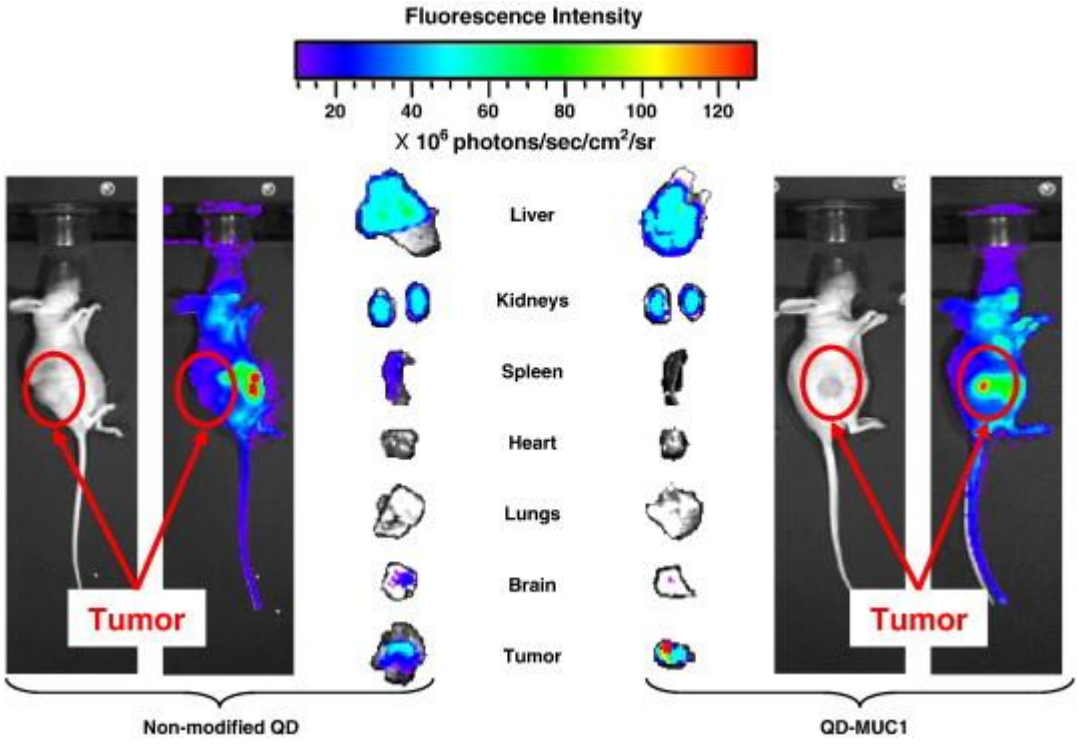

Figure 6.6 Organ and tumor content of non-modified quantum dots (QD) and tumor-targeted by MUC1 aptamer QD (QD-MUC1) conjugate. Multidrug resistant A2780/AD human ovarian carcinoma cells were transplanted subcutaneously into the flanks of nude mice. QD and QD-MUC1 were injected intravenously into mice. The distribution of QD in tumor and other organs was analyzed in live anesthetized animals 24 h after injection using IVIS imaging system. The intensity of fluorescence is expressed by different colors with blue color reflecting the lowest intensity and red color reflecting the highest intensity. After measuring the fluorescence in the entire animal, mice were euthanized and tumor and organs were excised and their fluorescence was registered and processed by the imaging system.

7 TUMOR-TARGETED RESPONSIVE NANOPARTICLE-BASED SYSTEMS FOR MAGNETIC RESONANCE IMAGING AND THERAPY

7.1 Introduction

Theragnostics is an emerging field in medical research that can potentially improve overall patient therapy and outcome by combining diagnostic and specific therapeutic properties [219]. Numerous research groups use various nanotechnology approaches for developing theragnostic agents. Although nanoparticles allow for distinct advantages in the field of therapy of different diseases, a combination of both diagnostic and therapeutic modalities in a single nanoparticle may be associated with certain difficulties. While nanoparticle properties can be fine-tuned in regards to the size, surface groups, and surface charge, synthesis of such a particle will be challenging due to the sheer number of modification steps involved. In addition, a single particle with both diagnostic and therapeutic capabilities may result in unnecessary treatment of false-positive tissues. Therefore, it may be ideal to develop a separated, but integrated multi-particle system for theragnostics.

Medical imaging procedures such as computed tomography (CT), X-ray, positron emission tomography (PET) and magnetic resonance imaging (MRI) are very commonly utilized in the clinic for the diagnosis and prognosis of various diseases. Designing nanoparticle contrast agents for these imaging modalities is an attractive and important

goal. Each imaging modality has its strengths and limitations and the use of several type of imaging agents in combination may gain additional benefits in terms of revealing hidden details and improving the reliability of a diagnosis. MR imaging often represents the preferred modality for its cost efficacy and the non-invasive and non-ionizing nature [11]. In addition, MRI provides anatomical images at high resolutions [12] thus making it an attractive imaging approach for the detection of small tumors and metastases.

Resolution of target structure or tissue can be enhanced by the use of MRI contrast agents, which are sub-divided into either T1-positive (paramagnetic) or T2-negative (superparamagnetic) agents [13]. Gadolinium chelates have been FDA approved for use as contrast agents for MRI. However, possible induction of nephrogenic systemic fibrosis is a concern with these agents. In addition, the small size of the chelate imaging agents results in short circulation times [14]. This may result in insufficient concentrations accumulated at spots of interests. It was concluded that a circulation half-life of two to six hours would allow for adequate accumulation at target sites and therefore increased contrast [73]. Nanoparticles have been extensively investigated for the delivery of small molecules and nucleic acids and as well as for imaging purposes [220]. In addition, many types of nanoparticles have been investigated as optical imaging probes. Although optical imaging works well for small animals, its utilization for larger animals and humans represent certain difficulties. In addition, optical approach is not ideal for imaging of deeper anatomical structures [221]. Moreover, instruments for optical imaging have yet to be fully developed for humans. Consequently, MRI especially in

combination with nanoparticle-based contrast agents represents the most valuable approach for the detection of primary tumors and metastases.

It is known that nanoparticles coated with polyethylene glycol (PEG) polymer chains (PEGylated) may achieve circulation times up to several days [73]. With the customizable nature of properties of such nanoparticles, nanocarriers for contrast enhancing agents with an optimal circulation time can be designed for imaging. In addition, the surface of such long-circulating nanocarriers can be modified with targeting ligands to improve targeting of imaging moieties specifically to cells and tissues of interest, *e.g.* primary localized and spreading tumors as well as metastases. Previously we have shown that many types of cancer cells overexpress luteinizing hormone releasing hormone (LHRH) receptors and LHRH peptide was successfully used in our laboratory as a targeting moiety for delivering drugs to tumors [52, 114, 115, 179, 222-226]. Most imaging nanoparticles contain metal oxides and the cores of these particles are frequently synthesized at high temperatures and in inert atmospheres [86]. Superparamagnetic iron oxide nanoparticles (SPIONs) are often employed as T2-negative contrast agents. However, the utilization of SPIONs as MRI contrast enhancers is hindered due to their negative contrast effect and tendency to include artifacts in the images [98]. Recently, manganese oxide nanoparticles have begun to be investigated as positive MRI contrast agents [11, 78, 98, 105, 227, 228]. However, manganese-based contrast agents are not as well-studied as SPIONs.

Nanoparticle-based contrast agents are endowed with their imaging capabilities primarily due to the properties of their cores. Since the nanocrystal cores of such nanoparticles are not water soluble, a coating layer is required in order to provide for intravascular injection or oral delivery and transport of the nanoparticles in the systemic circulation. The most common coatings for manganese-based contrast agents are silica shells [12, 13] and lipid-PEG molecules [105, 106]. In the form of coated nanoparticles, manganese atoms have a little contact with water and therefore bulk arrangement of atoms as in nanoparticles have low molar relaxivities and result in low positive contrast [78]. When Mn^{2+} ions are released from the bulk nanocrystal structure inside cells after endocytosis (mainly under the action of low pH in endosomes), the ability of magnesium compounds to increase the relaxation rates of the surrounding water proton spins and therefore molar relaxivity may increase 10-fold.

Once the disease is diagnosed, it is important to deliver therapeutic agents to treat or cure the disease. Cytotoxic drugs are widely used for therapy of many types of cancers. Despite improvements in drug design and chemotherapy combinations, several challenges still limit the efficiency of the treatment. Conventional small molecule chemotherapeutic drugs lack specificity, possess high toxicity, and frequently induce drug resistance. Improvements in genetic analysis of cancers and computation have led to design of more selective and more potent drugs. Yet, the challenges faced by conventional chemotherapeutics have not been completely overcome, by only mitigated in part.

Nanoparticle-based delivery of chemotherapeutics has become a widely spreading area of research. Polymers, dendrimers, liposomes, emulsions, and inorganic nanoparticles have been extensively studied for the delivery of small molecules [52, 224, 229-235]. More recently, solid lipid nanoparticles (SLNs) and nanostructured lipid carriers (NLCs) have begun to be increasingly investigated to overcome problems associated with other nanoparticle carriers [65, 225, 236, 237]. The most of novel and potent chemotherapeutic drugs tend to have very poor water solubility; therefore, entrapment in a lipid-based carrier may substantially improve their bioavailability and enhance the treatment efficacy. Although emulsions and liposomes are typically synthesized with well-studied excipients and can be produced on large scales, they have a limited ability to protect and modulate release of loaded drugs [238]. Whereas SLNs are colloids consisting of solid lipids, NLCs contain liquid lipid entrapped within the voids of a spatially different solid lipid matrix [239]. The liquid lipid appears not to affect the crystal structure of the solid lipid [69]. Lipophilic drugs are solubilized in the liquid lipid and thus entrapped within the solid lipid matrix. Therefore, the loading capacity and effective drug release of NLCs is better when compared with SLNs [65, 69].

In the present study, we have designed and tested biocompatible manganese oxide nanocrystals, which are capable of enhancing diagnosis and imaging of melanoma, ovarian and lung cancers using monoclonal antibodies or peptide cancer targeting moieties. We also demonstrated the ability to specifically target primary and metastatic tumors and diagnose them with efficient positive contrast ability. In addition, a

cleavable peptide was conjugated onto the surface of the developed nanoparticles to act as a potential chemotactic messenger. Once deposited at tumor sites, matrix metalloproteinases can cleave a fragment off of the attached peptide. The detached peptide containing biotin modification can diffuse away from the tumor site and into the systemic circulation. A concentration gradient of cleaved peptide fragments can be established, higher in proximity to the tumor site and lower farther away from tumor. Therapeutic nanoparticles modified with avidin can bind to the biotin molecule on the cleaved fragment and potentially be recruited to the tumor site. This presents a novel paradigm in targeted delivery whereby the target is not a cell-surface receptor on cancer cells, but rather a messenger molecule. A chemotherapeutic agent, vemurafenib, was furthermore entrapped in NLCs in order to effectively reach sites of melanoma tumors and metastases.

7.2 Materials and Methods

7.2.1 Materials

Manganese (II) chloride, oleic acid, N-hydroxysuccimide (NHS), 3,3',5,5'-tetramethylbenzidine (TMB), oleylamine, phosphoric acid ($\geq$ 85 % wt.), calcium chloride, ethylenediaminetetraacetic acid (anhydrous, Sigma grade, approx. 99% titration, EDTA), 4-(2-hydroxyethyl)-1-piperazineethanesulfonic acid (HEPES), sodium chloride, hydrochloric acid (molecular biology grade, 36.5-38.0%), hydroxylamine hydrochloride (ReagentPlus®, 99%), Tween® 80, and S-acetylthioglycolic acid N-hydroxysuccinimide

ester (SATA, ≥ 95% TLC) were purchased from Sigma-Aldrich (St. Louis, MO). Chloroform (HPLC grade), dimethyl sulfoxide (DMSO), reagent alcohol, xylenes, sodium dodecyl sulfate (SDS), N,N-dimethylformamide (DMF), sodium hydroxide (10N solution, 30% w/w), 1X phosphate buffered saline (PBS) were purchased from Fisher Scientific (Fair Lawn, NJ). Pierce® Avidin, 1-ethyl-3-[3-dimethylaminopropyl]carbodiimide hydrochloride (EDC) were purchased from Thermo Scientific (Rockford, IL). SYBR® Gold nucleic acid gel stain was purchased from Life Technologies (Carlsbad, CA). Isopropyl myristate (96%) was purchased from Acros Organics. Cy5.5 Mono NHS-Ester was supplied from GE Healthcare Life Sciences (Piscataway, NJ). 1,2-distearoyl-*sn*-glycero-3-phosphoethanolamine-N-[Maleimide(Polyethylene Glycol) 2000] ammonium salt (DSPE-PEG-MAL), 1,2-distearoyl-*sn*-glycero-3-phosphoethanolamine-N-[Amino(Polyethylene Glycol) 2000] ammonium salt (DSPE-PEG-NH_2), soy L-α-phosphatidylcholine (soy PC), and 1,2-dioleolyl-3-trimethylammonium-propane chloride salt (DOTAP) were purchased from Avanti Polar Lipids (Alabaster, AL). Anti-Melanoma antibody cocktail (ab733) was purchased from Abcam (Cambridge, MA). Precirol® ATO 5 was a kind gift from Gattefosse (Paramus, NJ). Vemurafenib was purchased from Selleckchem (Houston, TX). Custom luteinizing hormone releasing hormone (LHRH) and cleavable by matrix metalloproteinase 2 (MMP2) peptides were manufactured by American Peptide Company (Sunnyvale, CA) according to our design. The LHRH targeting peptide had the amino acid sequence of Gln-His-Trp-Ser-Tyr-D-Lys(D-Cys)-Leu-Arg-Pro-NHEt. A custom MMP2 peptide contained the sequence of Biotin-Gly-Pro-Leu-Gly-Ile-Ala-Gly-Gln.

Human active, recombinant MMP2 enzyme (MW 66 kDa) was purchased from EMD Millipore (Darmstadt, Germany).

7.2.2 Synthesis of Mn_3O_4 Hydrophobic Cores

Manganese oxide (Mn_3O_4) hydrophobic cores were synthesized according to the published protocol [106]. Briefly, one mmol of manganese (II) chloride, two mmol of oleic acid, and ten mmol of oleylamine were dissolved in 15 mL of xylenes at atmospheric conditions. The solution was heated and once it reached 90 ºC, 3 mL of deionized water was added. The reaction was allowed to age at 90 ºC for 3 h. The hydrophobic cores were precipitated with the addition of reagent alcohol and isolated by centrifugation. The dry cores were waxy and weighed before being dispersed in chloroform.

7.2.3 Synthesis of Water Soluble Mn_3O_4 Nanoparticles (NH_2/MAL Mn_3O_4 NPs)

Hydrophobic Mn_3O_4 cores (10 mg), 20 mg of DSPE-PEG-NH_2 and 5 mg of DSPE-PEG-MAL were mixed in 2 mL chloroform. After proper mixing, the reaction mixture was heated to 60 ºC and 8 mL of DMSO was slowly added. The reaction was stopped after all of the chloroform had evaporated. The dispersion could be used for further modification or dialyzed against water. The used solvent exchange method is more appropriate when compared with other coating methods such as thin film hydration because the resulting hydrophilic particles are more uniform and stable.

7.2.4 Conjugation of MMP2 Cleavable Peptide (MMP2/MAL Mn_3O_4 NPs)

A custom peptide (biotin-Gly-Pro-Leu-Gly-Ile-Ala-Gly-Gln) that is cleaved specifically by MMP2 enzyme [240] was attached to NH_2/MAL Mn_3O_4 NPs using amide bond. The carboxy terminal of the MMP2 cleavable peptide would react with the surface free amines on the NH_2/MAL Mn_3O_4 NPs. The free carboxyl on the MMP2 cleavable peptide was activated using EDC and NHS cross linkers. After 15 min, NH_2/MAL Mn_3O_4 NPs were added. The reaction was allowed to continue for 24 h. The resultant conjugate was dialyzed against deionized water.

For *in vivo* biodistribution studies and peptide cleavage study, the MMP2 cleavable peptide without biotin (Gly-Pro-Leu-Gly-Ile-Ala-Gly-Gln) was reacted with Cy5.5-NHS ester. After 24 hour of allowing for conjugation, the resulting Cy5.5-MMP2 was conjugated onto NH_2/MAL Mn_3O_4 NPs as described above to yield Cy5.5-MMP2/MAL Mn_3O_4 NPs.

7.2.5 Attachment of LHRH Targeting Moiety (MMP2/LHRH Mn_3O_4 NPs)

Previous studies have shown the ability of LHRH peptide (Gln-His-Trp-Ser-Tyr-DLys(DCys)-Leu-Arg-Pro-NHEt) to target various delivery systems specifically to different cancer cells [114, 115, 223]. After attaching the MMP2 cleavable peptide, a thioether linkage was synthesized using the maleimide moiety on the MMP2/MAL Mn_3O_4 NP and the cysteine residue on LHRH peptide. In 100 mM phosphate buffer, 10 mg of custom

LHRH peptide was reacted with previously synthesized MMP2/MAL Mn_3O_4 NPs. The reaction was performed at 4 ºC overnight. The resultant conjugate was dialyzed against deionized water. The presence and amount of attached peptide was confirmed and measured using the Pierce® Bicinchoninic Acid (BCA) Protein Assay Kit (Thermo Scientific, Rockford, IL).

7.2.6 Attachment of Anti-Melanoma Antibody (MMP2/ab733 Mn_3O_4 NPs)

The antibody modification and attachment protocol was adapted from Na *et al.* [105]. An anti-melanoma antibody cocktail was purchased from Abcam (Cambridge, MA). The mixture is able to target neuraminidase-sensitive side chain in immature melanosomes (HMB45 antibody), melanoma antigen recognized by T cells (MART-1, DT101 and BC199 antibodies), and tyrosinase (T311 antibody). Briefly, ab733 Anti-Melanoma antibodies in 0.5 mL PBS was reacted with 60 µL of SATA in DMSO (1.5 mg/mL) for 30 min. Afterwards, 120 µL hydroxylamine (0.5 M in PBS) was added and the reaction was allowed for 2 h at room temperature. The modified antibody was purified using Amicon® centrifugal device (MWCO 30 kDa, Millipore, Billerica, MA). The purified product was added to MMP2/MAL Mn_3O_4 NPs in 100 mM phosphate buffer. The reaction was performed at 4 ºC overnight. The resultant conjugate was dialyzed against deionized water.

7.2.7 Quantification of Manganese Content in Mn_3O_4 NP Formulations

Manganese concentration in the NP formulation was assessed using a colorimetric assay. The original assay, developed for photosynthetic membranes [241], was adapted for assessing the manganese content of NPs. Briefly, conjugates were digested using concentrated hydrochloric acid. After the particles were disintegrated, the solution was diluted with deionized water and concentrated sodium hydroxide solution was added to create a basic pH solution. 3,3',5,5'-tetramethylbenzidine (TMB) dissolved in 0.1 M hydrochloric acid was added and a precipitate was formed. Addition of 5.3 M phosphoric acid dissolved the crystals. The absorbance of the solution was measured at 450 nm wavelength. The manganese concentration was calculated based on a calibration curve.

7.2.8 MMP2 Gene Expression

RNA was isolated from ovarian cancer cell lines using RNeasy kit (Qiagen, Frederick, MA) following the manufacturer's protocol. Ready-To-Go You-Prime First Strand Beads (Amersham Biosciences, Piscataway, NJ) was mixed with 1 µg of total RNA and 100 ng of random hexadeoxynucleotide primer (Amersham Biosciences, Piscataway, NJ) to synthesize cDNA. The reaction mixture was subjected to quantitative polymerase chain reaction (qPCR) using SYBR® Green Master Mix as a detection agent. Qiagen (Frederick, MA) software was used to calculate difference in MMP2 gene expression between the

cell lines by first normalizing the MMP2 gene expression in each cell line with that of β-actin, a housekeeping gene.

7.2.9 Digestion of MMP2-Cleavable Peptide

The protocol was adapted from a previous study [240]. A small amount of Cy5.5-MMP2/LHRH Mn_3O_4 NPs and 1 mg/mL of human MMP2 enzyme was mixed in HEPES buffered saline. At selected time intervals, a small amount was removed and centrifuged using Amicon® centrifugal device (MWCO 30kDa, Millipore, Billerica, MA). The retentate was re-dissolved in buffer and the fluorescence signal was measured for Cy5.5 (λ_{ex} = 670 nm, λ_{em} = 690 nm). Cy5.5 dye was conjugated to the terminal end of the MMP2 cleavable peptide. Therefore, when the peptide is cleaved between glycine and isoleucine, the portion of Cy5.5-Gly-Pro-Leu-Gly is no longer attached to the surface of the nanoparticles and thus can be removed by centrifugal filtration.

7.2.10 Synthesis of Nanostructured Lipid Carriers (NLCs)

A previously published protocol from our group was adapted for this project [225]. Briefly, a melted ultrasonic dispersion method was utilized to synthesize vemurafenib (Vem) containing NLCs. Vemurafenib dissolved in DMSO was mixed into a hot lipid phase, which consisted of 100 mg Precirol ATO 5 (Gattefossé USA, Paramus, NJ), 100 mg isopropyl myristate, and 5 mg soy PC. The aqueous phase was composed of 250 mg Tween® 80, 10 mg DSPE-PEG-NH_2, and 25 mg DOTAP in 10 mL deionized water. Both

phases were heated to 80 ºC in a silicone oil bath. After 15 min, the lipid phase was added to the aqueous phase while homogenizing at 12,000 rpm for 5 min using a high-speed homogenizer (PRO Scientific Inc., Oxford, CT). The emulsion was subject to ultrasonication (Model 120 Sonic Dismembrator, Fisher Scientific, Fairlawn, NJ) for 5 min at 3 W. The resulting emulsion was cooled to 4 ºC in ice while being magnetically stirred. The NLC emulsion was dialyzed against deionized water using a membrane (MWCO 15 kDa) at 4 ºC overnight. The dialyzed emulsion was stored at 4 ºC. Empty NLCs were prepared in the same manner with equal volume of DMSO instead of vemurafenib.

7.2.11 Vemurafenib HPLC Calibration Curve

Previously, a published protocol was modified for measuring vemurafenib concentration by HPLC [242]. The chromatography system consisted of a Waters 1525 with a Binary pump, Waters 2487 Dual wavelength absorbance detector, Waters 717 plus autosampler, and Breeze workstation (Waters Corp, Milford, USA). The stationary phase consisted of a C8 Xterra® MS (250mm x 4.6mm, 5µm; Waters Corp, Milford, USA) column with a guard column and a mixture of 100 mM glycine buffer (pH 9.00) and acetonitrile (45:55, v/v) was used for the mobile phase. Each sample was subjected to a 15 min run at a flow rate of 0.9 mL/min at 30 ºC. The UV detector was used to detect vemurafenib at a wavelength of 249 nm.

7.2.12 Vemurafenib Entrapment Efficiency and Loading in NLCs

Due to the high hydrophobicity of vemurafenib, the concentration of free drug dissolved in the water phase is negligible. In order to measure the concentration of bound drug, the NLC-vemurafenib conjugates were disrupted by mixing with 4X volume of methanol. Then, the mixture was sonicated for 10 min and centrifuged at 3,500 rpm for 15 min. The supernatant was collected and analyzed using described above HPLC protocol.

7.2.13 NLC Drug Entrapment Stability

The entrapment stability of vemurafenib in NLC formulation was studied using dialysis. A small volume of Vem-NLC dispersion was loaded in a dialysis membrane (Spectra/Por® Biotech RC dialysis membrane, MWCO 15 kDa, Spectrum Laboratories Inc., Houston, TX) and placed in phosphate buffered saline containing 15 % ethanol and stirred with a magnetic stirrer at 37 ºC. At pre-determined time intervals, a small amount of Vem-NLC dispersion was removed from the membrane as well as the medium. The Vem-NLC sample was disrupted as above and both samples (Vem-NLC and medium) were run on HPLC to assess vemurafenib concentration.

7.2.14 Size Distribution and Cytotoxicity

The size distributions of MMP2/LHRH Mn_3O_4 NPs and Vem-NLC formulations were measured using Malvern ZetaSizer NanoSeries (Malvern Instruments, Malvern, UK)

according to the manufacturer's recommendations. Measurements were performed at 25 ºC. The sizes were measured five times, and average values were calculated. The cytotoxicity of MMP2/LHRH Mn_3O_4 NPs and empty NLCs were assessed using a modified MTT (3-(4,5-dimethylthiazol-2-yl)-2,5-diphenyltetrazolium bromide) assay as previously described [243]. Briefly, CHO-K1 cells (a model for normal cells) were plated in a 96 well plate at a density of 10,000 cells/well. Twenty-four hours after seeding, different concentrations MMP2/LHRH Mn_3O_4 NP conjugates were added to the cells. Control cells were treated with an equal volume of fresh medium. The cells were treated for 24 h. The liquid was removed and replaced with fresh medium and MTT solution. After further 3 h incubation, a solubilizing solution was added and the plates were stored overnight. The absorbance intensity was measured the following day. The cytotoxicity of drug-containing formulations was measured using metastatic melanoma cell line, COLO 829 (ATCC® CRL-1974), which expressed the V600E mutation. The following formulations were assessed: free non-conjugated vemurafenib (Vem) and vemurafenib entrapped in NLCs (Vem-NLC).

7.2.15 Genotoxicity

The genotoxicity of MMP2/LHRH Mn_3O_4 NPs and NLCs was assessed using the CometAssay® HT kit from Trevigen (Gaithersburg, MD). Approximately 300,000 CHO-K1 cells were plated in a 25 cm^2 cell culture flasks and incubated for 24 h prior to treatment. Cell culture medium was replaced with either fresh medium (negative

control), medium containing 100 μM of hydrogen peroxide (positive control), non-cytotoxic concentration of MMP2/LHRH Mn_3O_4 NP (7.1 mg/l Mn^{2+}) or empty NLCs (80 mg/l lipid concentration) for 24 h. After the treatment, the cells were pelleted and suspended in ice-cold PBS buffer at a concentration of 1×10^5 cells/ml. The cell suspension was mixed with molten COMET Agarose at a ratio of 1:10 (v/v). A small aliquot was pipetted onto the surface of a COMET slide. After solidification, the slides were immersed in lysis solution at 4 ºC for 30 min and then in alkaline unwinding solution for 60 min at room temperature. The slides were placed in a horizontal electrophoresis apparatus containing enough 1X TBE buffer to cover the samples. Minimal voltage was applied for 45 min. Afterwards, the slides were rinsed with deionized water and 70 % ethanol. Samples were air dried to bring all cells into a single plane. DNA was stained with SYBR Gold (Life Technologies, Carlsbad, CA) for 30 min. The samples were rinsed with deionized water, dried, and viewed using a fluorescence microscope. DNA damage was assessed by calculating the percent of DNA in the comet tail using CometScore™ (TriTek Corp., Sumerduck, VA) software.

7.2.16 Cancer Cells

Human lung (A549), ovarian (A2780), melanoma (COLO 829) cancer cells and Chinese hamster ovary cells (CHO-K1) were purchased from ATCC (Manassas, VA). A549 cells expressing luciferase enzyme were purchased from Xenogen Bioscience (Cranbury, NJ). The ascitic fluid with cancer cells was obtained from the peritoneum area of the patients

with ovarian cancer provided by the Cancer Institute of New Jersey. The samples were centrifuged for 20 min at 2000 g; the supernatant was discarded and cell pellets were consequently re-suspended. The re-suspended cells were cultured in RPMI 1640 media with L-glutamine (Lonza, Walkersvile, MD) supplemented with 15% fetal bovine serum (Invitrogen, Carlsbad, CA), 2.5 μg/ml insulin (Sigma, St. Louis, MO) and 1.2 mL/100 mL penicillin-streptomycin (Gibco, Grand Island, NY). A549, A2780, and COLO 829 cells were grown in RPMI 1640 medium (Lonza, Walkersville, MD) supplemented with 10% fetal bovine serum (Life Technologies, Carlsbad, CA) and 1.2 mL/100 mL penicillin-streptomycin (Life Technologies, Carlsbad, CA). CHO-K1 cells were grown in F12-K medium supplemented with 10% fetal bovine serum (Life Technologies, Carlsbad, CA). All cells were grown in a humidified atmosphere of 5% CO_2 (v/v) at 37 ˚C. All experiments were performed on the cells in the exponential growth phase.

7.2.17 Animal Cancer Models

The current research adhered to the ''Principles of Laboratory Animal Care'' of NIH and was carried out according to the protocols approved by the Institutional Animal Care and Use Committee (IACUC). Nude mice were inoculated with human lung (A549) and ovarian (A2780) cancer cells or cells isolated from malignant ascites obtained from patients with ovarian carcinoma. All cancer cells were transfected with luciferase. Orthotopic lung cancer mouse model was created by intratracheal instillation of A549 lung cancer cells as previously described [225, 244, 245]. Both orthotopic

(intraperitoneal) and xenograft (subcutaneous) ovarian cancer models were created using A2780 or malignant ascites cells as previously described [222, 224, 226]. Luciferase transfected cancer cells were visualized in live anesthetized animals using *in-vivo* bioluminescence IVIS system (Xenogen, Alameda, CA). Luciferin (150 mg/kg) was intraperitoneally administered 10-15 minutes before imaging. According to the IACUC policy, the size of subcutaneous tumor was measured daily using a caliper and the volume was calculated as $d^2 \times D/2$ where d and D are the shortest and longest diameters (in millimeters) of the tumor, respectively. Once the tumor volume reached 200- 300 mm^3, MMP2/LHRH Mn_3O_4 nanoparticles were injected intraperitoneally in the volume of 0.1 μL into the mice. For melanoma imaging studies, metabotropic glutamate receptor 1 (grm-1) transgenic mouse model was developed as previously described [246, 247]. The hallmark of the grm-1 transgenic mice is the spontaneous development of pigmented cutaneous melanomas. The melanoma development simulates that seen in humans where cancer first develops on the ears, then eyelids and then perianal region.

7.2.18 In vivo Optical and Magnetic Resonance Imaging

Mice were anesthetized with isoflurane (4 % for induction of anesthesia and 1–2 % for maintenance) using XGI-8 Gas Anesthesia System (Xenogen, Alameda, CA) for all imaging procedures. MRI was performed using a 1 T M2™ whole body scanner (Aspect Imaging, Shoham, Israel). Images (repetition time 2607 ms, echo time 44 ms) were

recorded in Fast Spin Echo sequence. At a spatial resolution of 312 μm, the tumors were coronal imaged in a single section through the mouse body using an image matrix of 256 × 256, a field of view of 80 mm^2, and 4 excitation. MR signal was calculated using Vivoquant 1.21 software (Invicro, Boston, MA). For MRI studies, mice were treated with 2 mg Mn^{2+} per kg body mass administered intraperitoneal [11] either in a free form or as the nanoparticle formulation.

7.2.19 Statistical Analysis

Data were analyzed using descriptive statistics and single-factor ANOVA, and are presented as a mean ± SD from five to ten independent measurements. Ten animals were used in each experimental group. The power analysis (alpha=0.05; power=80%) based on the preliminary results showed that ten mice per group are needed for statistical analysis to determine a 15% difference between the groups. We analyzed data sets for significance with Student's *t* test and considered *P* values of less than 0.05 as statistically significant.

7.3 Results

7.3.1 Synthesis and Characterization of Water Soluble Manganese Oxide Nanoparticles

Uniform hydrophobic Mn_3O_4 were synthesized at a low temperature and normal atmospheric conditions. The reaction yielded an average of approximately 150 mg of these hydrophobic cores. The reaction time allowed for control of crystal growth. Longer aging time led to synthesis of a larger nanocrystal. The three hour aging time in this reaction yielded cores with an average diameter of 6.17 nm. Previous investigation assessed the X-ray diffraction pattern of the nanocrystal synthesized using this procedure and identified the crystal as having a tetragonal (hausmannite) structure [106].

These manganese oxide cores are very hydrophobic and must be coated for clinical use. In addition to imparting water solubility, the polymer coating protects the particles from aggregation, limits hydrophobic interactions with cells especially immune cells, helps to improve pharmacokinetics and allows for further surface modification [248, 249]. Using a dual solvent exchange method, the hydrophobic cores were coated with lipid-PEG molecules to make them water soluble and allow for further modification.

When the core was coated with DSPE-PEG molecules, the average size increased to 42.17 $\pm$ 5.36 (mean $\pm$ SD) nm from 6.17 $\pm$ 0.76 (mean $\pm$ SD) nm ($P < 0.05$, Table 7.1). The

PEGylated Mn_3O_4 NPs displayed narrow size distribution and when stored at 4˚C, they had excellent stability properties. At 164 days of storage, there were no significant changes in mean particle size or particle size distribution (Fig. 7.1A).

The resulting NH_2/MAL Mn_3O_4 NPs were then modified first with a MMP2 cleavable peptide (Fig. 7.1B) and then with luteinizing hormone-release hormone (LHRH) receptor targeting peptide (Figure 1C; please note a thioether linkage of maleimide moiety on DSPE-PEG molecule with a cysteine residue on the LHRH peptide) to enable active targeting to ovarian and lung cancers [115]. Attachment of LHRH peptide was confirmed using BCA protein assay (Thermo Fisher Scientific Inc., Rockford, IL) according to manufacturer's protocol. The results of the BCA Assay indicated that in average 1.52 $\pm$ 0.33 (mean $\pm$ SD) mg LHRH peptide was attached onto the surface of 10 mg of MMP2/LHRH Mn_3O_4 NPs. The concentration of MMP2 cleavable peptide was below the sensitivity level of the BCA Assay.

The MMP2/LHRH Mn_3O_4 NPs were digested with hydrochloric acid and purified to obtain a solution containing manganese ions. A protocol used for determination of manganese concentration in water and plants was modified for our purpose. Based on our standard curve ($MnCl_2$ solution in deionized water), the Mn^{2+} concentration in the formulated MMP2/LHRH Mn_3O_4 NPs was 48.28 $\pm$ 7.59 (mean $\pm$ SD) mg/L. This concentration was used for manganese content in other experiments and was used for *in vivo* dosing (2 mg Mn^{2+} per kg mouse body weight).

Matrix metalloproteinases are extracellular enzymes involved in a variety of functions including modification of the extracellular matrix. They are present is almost all cell types and are seen in increased quantity and activity in a variety of pathologies including cancers including ovarian and lung cancers and melanoma [250]. Our results on two different ovarian cancer cell lines show that MMP2 is expressed nearly 5-6 folds higher in cells isolated from malignant ascites (*in vitro* cell culture and *ex vivo* tumor xenograft) obtained from patients with advanced ovarian carcinoma when compared with A2780 ovarian cancer cells (Fig. 7.2A).

The MMP2 peptide cleavage experiment showed that the fluorescence signal from the peptide labelled with Cy5.5 near infrared fluorescence dye decreased as the peptide was cleaved and the cleaved fragment removed (Fig. 7.2B). The cleavage between the glycine and isoleucine amino acids led to the dissociation of Cy5.5-Gly-Pro-Leu-Gly fragment, which was easily removed from the solution by centrifugal filtration. The data show that almost all peptide was cleaved from the NPs after 24 h.

7.3.2 Synthesis and Characterization of Vem-NLCs

The average particle size of Vem-NLCs was 174.51 $\pm$ 31.76 (mean $\pm$ SD) nm. The entrapment of vemurafenib within the NLCs was quantified based on the equations below. Based on the HPLC calibration curve, our formulation was able to entrap 6.23 $\pm$ 1.09 (mean $\pm$ SD) mg of the 10 mg of vemurafenib used in the synthesis yielding an entrapment efficiency of 62.3%. The drug loading percentage was 3.04%.

$$EE\% = \left(\frac{Wloaded}{Wtotal}\right) \times 100\%$$

$$DL\% = \left(\frac{Wloaded}{Wlipid}\right) \times 100\%$$

EE%-entrapment efficiency, DL%- drug loading, W_{total}- weight of vemurafenib added during preparation, W_{lipid}- weight of lipids used during preparation (Precirol ATO 5, Isopropyl myristate, Soy PC), W_{loaded}- weight of vemurafenib entrapped in Vem-NLC

One of the primary advantages of entrapping chemotherapeutics in nanoparticles is the reduction of free drug exposure in the plasma and off-target organs and tissues. An ideal nanocarrier would not release any drug in the blood circulation. Accumulation in tumor tissue by active targeting or enhanced permeation and retention (EPR) effect can allow for degradation of the nanocarrier and release of entrapped drug molecule. We examined by HPLC drug leakage and retention in the NPs in PBS buffer (pH = 7.4) within 72 h. The HPLC measurements did not reveal a measurable amount of vemurafenib in the dialysis buffer in these conditions. In contrast, the amount of vemurafenib still entrapped in NLCs did not change statistically significantly in the same conditions. Therefore, we concluded that the NLCs can retain vemurafenib in plasma with normal pH for at least 72 h.

7.3.3 Cytotoxicity and Genotoxicity of Nanoparticle Formulations

Cytotoxicity of MMP2/LHRH Mn_3O_4 NPs and NLCs were assessed using CHO-K1 cells, which we used as a model for normal healthy tissue. The results show that MMP2/LHRH Mn_3O_4 NPs and empty NLCs are non-cytotoxic at concentrations used in other experiments (Fig. 7.3A). In addition, genotoxicity study was performed using the commercially available CometAssay®, which demonstrated that empty MMP2/LHRH Mn_3O_4 NPs are not likely to induce DNA damage (Fig. 7.4). Negative (fresh medium) and positive (hydrogen peroxide) controls were used as references. The assay also revealed that empty NLCs do not cause appreciable DNA damage. Cytotoxicity of free vemurafenib and encapsulated vemurafenib was assessed using COLO 829 melanoma cells, which contain the BRAF V600E mutation. It was found that encapsulation of vemurafenib within NLCs significantly increased its cytotoxicity (Fig. 7.3B).

7.3.4 *In vivo* Animal Magnetic Resonance Imaging

The Mn_3O_4 NPs were tested as imaging agents in various mouse models of cancer. The development of lung and intraperitoneal tumors *in vivo* was confirmed by the detection of bioluminescence of cancer cells using IVIS imaging system in anesthetized animals (Fig. 7.5A). The administration of MMP2/LHRH Mn_3O_4 NPs to the mice with orthotopic lung cancer model substantially improved the visualization of the cancer mass in the lungs. Prior to contrast administration, only a small mass is detected in the lower lobe of the right lung (Fig. 7.5B). After injection of NPs, cancer cells were clearly detected in the

right lung (Fig. 7.5C). Consequently, the use of NPs as contrast agents increased signal in the entire lung and also brightened a potential metastatic mass on the periphery. In the intraperitoneal model of ovarian cancer, the administration of MMP2/LHRH Mn_3O_4 NPs not only increase signals in the cancer masses, but also allowed for outline of their shapes.

MMP2/ab733 Mn_3O_4 NPs were also used as the contrast agents for the detection of melanoma in transgenic mice. These mice spontaneously develop cutaneous melanoma lesions with frequent metastases. While the cutaneous lesions are easily identifiable, better procedures are required for detecting metastases. The use of NPs as contrast agents helped to detect internal metastases in the right lung and in the abdomen of the transgenic mice (Fig. 7.5C, lower panel).

In a subcutaneous ovarian cancer xenograft model, the tumor mass is visible on the right flank of the mouse (Fig. 7.6A). MMP2/LHRH Mn_3O_4 NPs were injected subcutaneously on the contralateral side of the mouse. The time lapse images show signal brightening at the site of the injection. More impressively, the images clearly show the diffusion of the tumor-targeted MMP2/LHRH Mn_3O_4 NPs from site of administration to the tumor and preferential accumulation in the primary tumor and metastases. Quantitative measurements revealed that 45 min post-injection, the MR signal in the tumor had increased by 22.3% (Fig. 7.6B).

7.4 Discussion

In the present investigation, the manganese oxide cores were synthesized using manganese chloride, oleic acid, and oleylamine as precursors. As the manganese chloride dissolved, it gave the reaction solution a pinkish color. Later, this transitioned into an orange to brown color. The addition of deionized water turned the solution to a dark brown-black color. The color transition to a brown-black color indicates formation of nanoparticles [251]. The reaction temperature plays a role in the core shape; high reaction temperatures lead to one dimensional rod formation whereas lower temperatures over a longer time yield spherical nanocrystals. In this method for crystallization, water acted as a reagent and the source for oxygen, oleylamine acted as a base to catalyze the nucleation of crystal, and the addition of oleic acid helped to create a spherical nanocrystal as compared to nanocrystal plates [106]. The three hour aging time used for this study yielded particles with an average diameter around 6 nm. Increasing the aging time to four hours resulted in the increase of average diameter of cores to approximately 18 nm. The smaller cores were used because of the potential for higher contrast resulting from the higher surface area to volume ratio for the smaller core compared to the larger core.

These hydrophobic cores cannot be used by themselves for therapy and must be converted into a water-soluble, biocompatible form. Thin film hydration is a commonly used technique to coat hydrophobic nanoparticle cores with lipid-PEG molecules to

make water soluble nanoparticles. However, this process results in irreversible aggregation of nanoparticles, creation of empty micelles, and raises concerns of stability issues. Using a dual solvent exchange method [252], in which the hydrophobic cores are coated by changing the solvent from chloroform to dimethyl sulfoxide to water results in a higher surface coating density, more uniform distribution of nanoparticles, and more stable nanoparticles. Because the immiscibility of chloroform and water, an intermediary solvent, dimethyl sulfoxide, was used in the present study to transfer the core/lipid-PEG mixture into water as well as to induce coating of the cores through hydrophobic interactions. PEGylated Mn_3O_4 nanoparticles showed narrow size distribution and no change in mean particle size or size distribution after 164 days of storage.

The coating with lipid-PEG molecules endows free surface functional groups, amines and maleimides, for further modification. MMP2 cleavable peptide was conjugated to the free primary amines using a stable amide bond. LHRH cancer targeting peptide was also attached via the cysteine to the maleimide functional group forming a thioether bond. The attachment of LHRH peptide was confirmed using the BCA protein assay. The LHRH peptide developed a strong and clear absorbance signal in this assay because of the presence of aromatic structures on amino acid side chains in this peptide. According to the manufacturer, the color formation of the assay is principally due to the presence of certain amino acids (cysteine, tryptophan, and tyrosine). These three amino acids are present in the LHRH targeting peptide and are absent in the MMP2 cleavable peptide.

This difference in the composition of these peptides explains a strong color development in the BCA assay for LHRH peptide and the absence of color formation in case of the MMP2 cleavable peptide.

It was interesting that when the water soluble nanoparticles were modified with MMP2 cleavable peptide, the average size decreased from 42.17 $\pm$ 5.36 (mean $\pm$ SD) nm to 25.09 $\pm$ 2.99 (mean $\pm$ SD) nm. This phenomenon could probably be attributed to a change in structure of the DSPE-PEG molecules [253]. The PEG molecule on the surface of NH_2/MAL Mn_3O_4 NPs likely maintains a "brush" configuration. The modification of NPs with the MMP2 cleavable peptide, changes its configuration to a "mushroom" configuration. Based on the data obtained, this configuration appears to be maintained after conjugation of LHRH targeting peptide. A nanoparticle size between 10-100 nm is typically sought for most intravenous applications. Nanoparticles larger than 200 nm are subject to rapid elimination by the reticuloendothelial system and those smaller than 10 nm can be efficiently cleared by the kidneys [254]. This size range also allows for passive tumor accumulation by the enhanced permeation and retention effect. The increase in size of MMP2/LHRH Mn_3O_4 NPs after coating with PEG showed that the used synthetic conditions led to the covering of nanoparticles with a substantial protective layer but did not result in a so-called "thick" coating. A thinner core coating allows for an easier passage of water to the core, liberation of Mn^{2+} ions, and quicker core digestion; all three processes will be amicable in increasing MR signal.

We hypothesized that the expression of MMP2 in the tumor microenvironment can be considered as a hallmark feature or cancers with high metastatic potential and, consequently, MMP2 cleavable peptide can be used to enhance the detection of metastases by MRI. In order to verify this hypothesis, we measured the MMP2 expression in established ovarian cancer cells and highly metastatic cancer cells isolated from malignant ascites obtained from patients with advanced ovarian carcinoma using quantitative PCR. The results of these measurements showed that highly metastatic cancer cells had a 5-6 - fold higher expression of MMP2 mRNA when compared with A2780 ovarian cancer cells. It is possible that the digestion of the peptide is correlated to the expression and activity of MMP2 enzyme. Consequently, the increase release of the biotin-fragment from the MMP2 peptide used in the present study after its cleavage in the tumor could potentially represent an attractive target for avidin-conjugated nanoparticles containing a therapeutic agent. We are planning to use such avidin-modified nanoparticles for targeted chemotherapy after the pretreatment with biotin modified MMP2 cleavable peptide on the surface of the Mn_3O_4 NPs. Once the biotin-Gly-Pro-Leu-Gly fragment is dissociated, it can act as a signal to recruit avidin-modified therapeutic drug containing nanoparticles to the tumor sites. This will provide a basis for the responsive theragnostic platform in which the therapeutic payload is preferentially delivered to tumors with high activity of MMP2 enzymes (*i.e.* containing highly metastatic cancer cells).

In the current study, two substantially different lipids were used for synthesis of NLC. Precirol® ATO 5 consists of glycerol distearate (type I) EP, glyceryl distearate NF, and glyceryl palmitostearate (USA FDA IIG). The combination of spatially different lipids results in an imperfect solid matrix. The addition of a specialized liquid lipid such as isopropyl myristate prevents the crystallization of the matrix to β forms and caused an amorphous matrix [255]. The combination of the two processes may yield a NLC with high drug loading and reduced drug expulsion. This appears to be evident from our results. Tween 80 and DSPE-PEG-NH_2 were added to improve water solubility of the lipid carrier. The primary amine on the DSPE-PEG-NH_2 can be used to add other functionalities in the future such as targeting ligands such as avidin. A study by Bocca *et al.* [256] showed that PEGylated or stealth solid lipid nanoparticles had reduced phagocytosis rate compared to non-stealth counterparts. The increased circulation time will increase the likelihood of the nanoparticles to be recruited to tumor sites.

There is a restriction on the use of gadolinium chelate MRI contrast agents because of the potential of nephrogenic systemic fibrosis [257]. Several iron based contrast agents have been withdrawn from market due to safety concerns or discontinued by the manufacturer. GastroMARK® is the only available iron oxide contrast agent available and is approved for imaging of the gastrointestinal tract [80, 258]. However, performing solely a cytotoxicity assay does not adequately address safety concerns. Previously, we showed that even at safe levels, nanoparticles may impose negative effects on healthy tissues, *e.g.* induce genetic aberrations [259]. The CometAssay® allows for the

visualization of DNA damage caused by treatment with nanoparticles. After cells are treated with the nanoparticles, any DNA damage resulting in fragmentation appears as tails after electrophoresis. Long tails and more intense SYBR Gold® staining in the tail are indications of DNA damaging potential of nanoparticles. The results of this assay indicated that MMP2/LHRH Mn_3O_4 NPs and empty NLCs did not demonstrate signs of genotoxicity and thus are safe for *in* vivo use.

Free anticancer drugs have large volumes of distribution and therefore may have adverse side effects on normal tissues, fast clearance, and reach insufficient concentrations at tumor sites. Delivery of anticancer drugs using nanoparticles has the realistic potential of overcoming these deficiencies. Lipid-based nanoparticles are composed of biocompatible materials and are ideal in incorporating lipophilic compounds. Unlike SLNs, the inclusion of a liquid lipid in our formulation results in NLCs. The liquid lipid (isopropyl myristate) fills the gaps in the crystal structure of the solid lipid (Precirol ATO 5). The drug molecule is solubilized in the liquid lipid portion of the formulation for NLCs as opposed residing in the gaps of the crystal structure of SLNs. Although NLCs have been shown to have higher entrapment of small drug molecules and less significant drug leakage, the liquid lipid portion appears to be the limiting factor for drug loading as the amount of drug entrapped is partially determined by its solubility in the liquid lipid. The current formulation was able to achieve 62.3% entrapment efficiency. Increasing the amount of drug in the pre-synthesis reaction did not increase

loading. Therefore, the limiting factor may be the solubility of vemurafenib in isopropyl myristate.

The encapsulation of an anticancer agent within the matrix of a nanocarrier ensures that healthy tissues are not exposed to the substance. There was no release of vemurafenib from the liquid lipid filled matrix of the NLCs in neutral pH in PBS buffer for at least 72 h. Therefore, release of free drug would require nanoparticle digestion, which can occur in the lysosomal environment of cancer cells.

The cytotoxicity potential of the NLC entrapped vemurafenib formulation was assessed in COLO 829 human metastatic melanoma cell line. This cell line has the BRAF V600E, which is found in a large proportion of melanomas. Vemurafenib was developed as a molecularly targeted agent for this mutation. Because of its specificity to the mutation, vemurafenib should be effective in melanoma cells and not induce severe adverse side effects on normal cells. However, clinical use of the drug has shown the potential for the development of squamous cell carcinomas [20]. Delivery within a NLC can increase accumulation in melanoma cells and spare healthy skin tissue.

MTT cytotoxicity assay in COLO 829 revealed that encapsulation of the drug into nanocarriers significantly increased its cytotoxicity when compared with free non-encapsulated vemurafenib. The comparison of these finding with other results of the present study shows the potential of the cancer-targeted Vem-NLCs formulations for

decreasing systemic exposure to vemurafenib and increasing its cytotoxicity specifically in malignant melanoma cells.

Administration of MMP2/LHRH Mn_3O_4 NPs into a subcutaneous ovarian cancer model resulted in a significant increase in MR signal intensity. After 45 min, the signal had improved in average by 22.3%. The entire tumor mass showed an increase in signal demonstrating that the nanoparticles had preferentially accumulated in the tumors. This is important in the diagnosis of cancer because the more accurate determination of the size of the tumor can help in determining the next steps in therapy. High sensitivity of MRI combined the proposed imaging contrast NPs will help in early cancer diagnostics and detection of metastases. Also, imaging procedures can be used for monitoring therapy prognosis and decrease in tumor size. The preferential accumulation of cancer-targeted NPs in tumors was confirmed by monitoring the passage of the NPs from the administration site to the tumor xenograft with time. In addition to the subcutaneous model, Mn_3O_4 NPs were evaluated in orthotopic mouse models that resemble a similarity to cancer development in humans. The pre- and post-dose images demonstrate the power of the Mn_3O_4 NPs as MR imaging agents and showed a significant increase in the MR signal. Also, this experiment demonstrates that the particles are not simply deposited, but selectively accumulate in tumor tissue. In fact, the lungs without tumors demonstrated no signal even after injection of the contrast agent.

Although the intraperitoneal ovarian primary tumor with malignant ascites has some signal intensity without contrast administration, the post-dose image not only shows an increase in the signal but also demonstrated the delineation of the tumor shapes. Changing the targeting ligand from LHRH peptide to ab733 anti-melanoma monoclonal antibodies allows the particles to be adapted for use for detection of melanoma. The PEGylated Mn_3O_4 NPs provide an excellent foundation for further modification to meet required needs. The MMP2/ab733 Mn_3O_4 NPs showed increased signal in two sites of melanoma metastasis.

MRI revealed that the signal began to decrease 30 minutes after injection of NPs. The circulation time appears to be ample for tumor accumulation and short enough to prevent deposition in healthy tissues, which can limit potential adverse side effects. The circulation time is likely to be dependent on the size of the nanoparticles, but further studies will need to be conducted for the confirmation of such conclusion.

Compared to other studies using that also used manganese oxide based imaging agents for *in vivo* studies [11, 12, 105], the dose (Mn^{2+} concentration) in the current study was chosen to be at the substantially lower range. It is important to use the lowest effective dose to prevent toxicity especially for nanoparticles that will be administered repeatedly. The proposed Mn_3O_4 NPs have the potential to be effectively used for diagnosis of various cancers and monitoring therapy prognosis. The ability of the

particles to clearly outline shape of tumor masses can be used to monitor decrease in tumor volume.

7.5 Conclusions

An original design of cancer targeted responsive nanoparticle-based systems for magnetic resonance imaging and treatment of different cancers was proposed. Two types of nanoparticles were developed based on PEGylated water soluble Mn_3O_4 nanoparticles and nanostructured lipid carriers. The nanoparticles were modified with cancer-targeting moiety (LHRH peptide or anti-melanoma antibodies). The possibility of modification with other peptides (*e.g.* biotinylated MMP2 cleavable peptide) and encapsulation of anticancer drugs (*e.g.* vemurafenib) was also verified and tested. Synthesized nanoparticles were evaluated *in vitro* and *in vivo* using different models of cancer (transgenic mice developed melanoma, nude mice with orthotopic human lung and ovarian cancers, as well as subcutaneous xenografts of ovarian cancer). The results of the present investigation showed substantial advantages of the proposed nanoparticles as MRI contrasting agents. The usage of these nanoparticles significantly amplified a magnetic resonance signal specifically from cancer cells and improved the detection of primary tumors, precise determination of their shape, and visualization of metastases. Preferential accumulation of cancer targeted nanoparticles in cancer cells not only enhanced the sensitivity of MRI but also open a door for targeted treatment of various types of cancer.

Particles	Size,nm
Mn_3O_4 cores	6.17 ± 0.76
NH_2/MAL Mn_3O_4 NPs	42.17 ± 5.36
MMP2/MAL Mn_3O_4 NPs	25.09 ± 2.99
MMP2/LHRH Mn_3O_4 NPs	26.68 ± 3.49

Table 7.1 Size of manganese oxide nanoparticles. Means ± SD are shown.

	Post-Dose	15 min	30 min
Lung Cancer	No difference	+15%	No difference
Ovarian Primary Tumor and Malignant Ascites	Slight brightening	Delineation of tumor masses	Delineation of tumor masses
Primary and Metastatic Melanoma	+59.26%	+69.51%	+17.64%

Table 7.2 Increase in magnetic resonance signal intensity post-dose.

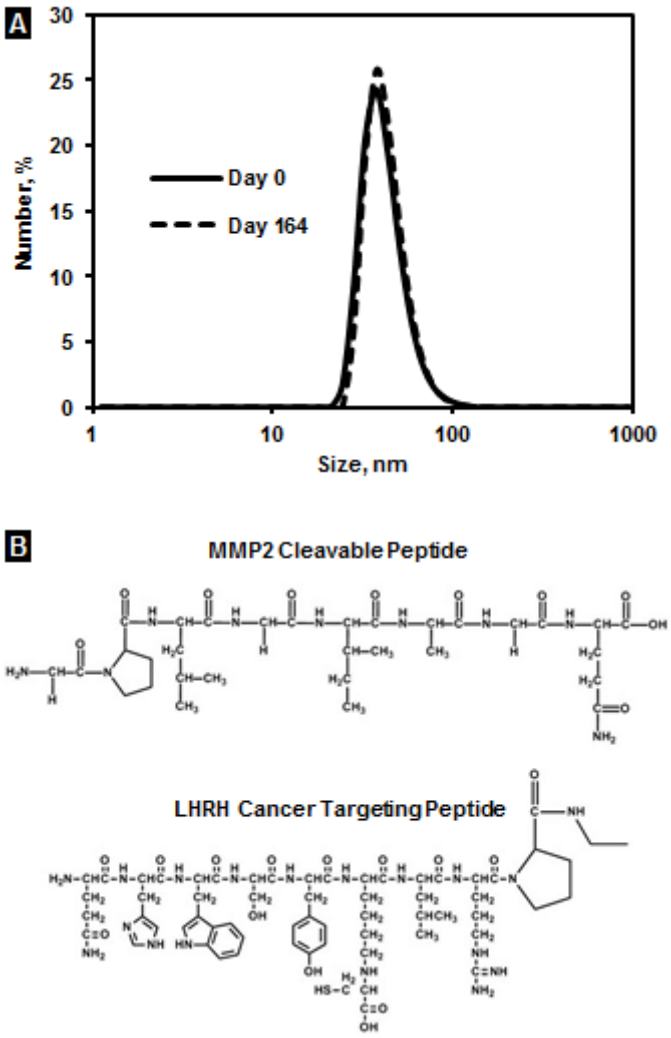

Figure 7.1 (A) Typical distribution of the size of PEGylated Mn_3O_4 nanoparticles before and after storage (164 days). (B) Chemical structures of MMP2 cleavable and LHRH cancer targeting peptides.

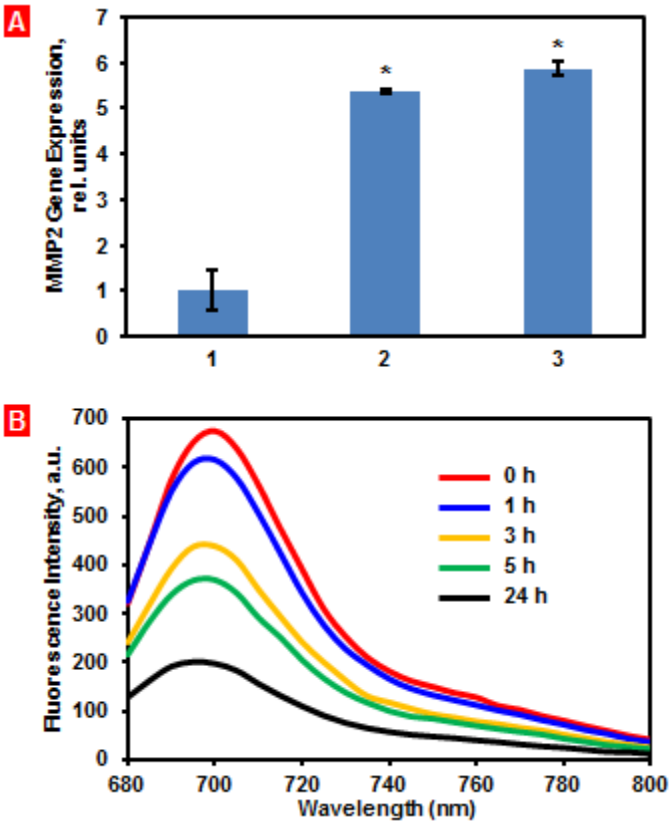

Figure 7.2 (A) Expression of MMP2 mRNA. The expression was measured by quantitative PCR in RNA isolated from: (1) A2780 human ovarian cancer cells; (2) cells from malignant ascites obtained from patients with ovarian carcinoma and grown *in vitro*; (3) tumor tissues from mice with xenografts of cancer cells from malignant ascites obtained from patients with ovarian carcinoma. Means ± SD are shown. *$P < 0.05$ when compared with A2780 human ovarian cancer cells. (B) Cleavage of MMP2 peptide after incubation with human MMP2 enzyme. Nanoparticles modified with cleavable MMP2 peptide were incubated with 1 mg/mL of human MMP2 enzyme in HEPES buffered saline. Representative fluorescence spectra are shown.

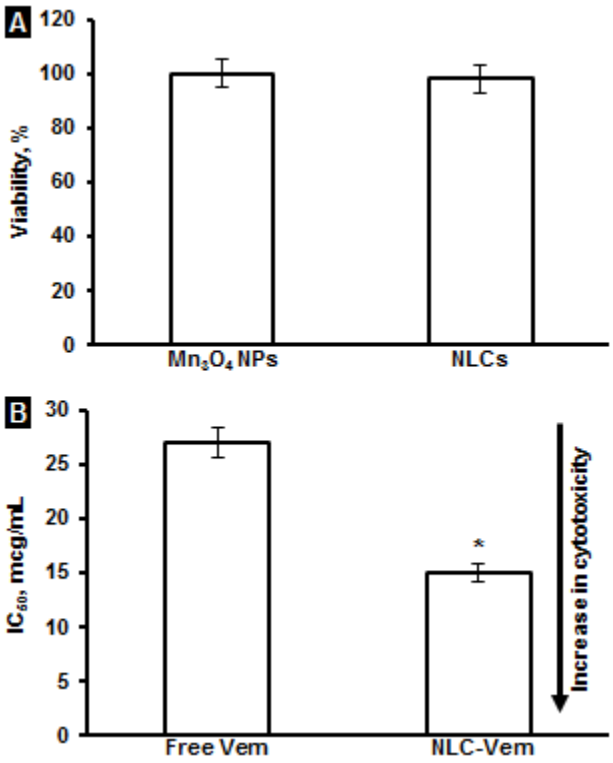

Figure 7.3 Cytotoxicity of nanoparticles (manganese oxide – Mn_3O_4 NPs and nanostructured lipid carriers – NLCs). (A) Cellular viability of CHO-K1 cells incubated with nanoparticles that do not contain an anticancer drug. The cells were incubated 24 h with nanoparticles indicated. (B) Cytotoxicity of free non-conjugated vemurafenib (Vem) and NLC-encapsulated Vem. COLO 829 metastatic melanoma cells with the targeted V600E mutation were incubated with free and encapsulated in NLC-Vem. Means ± SD are shown. *$P < 0.05$ when compared with free vemurafenib.

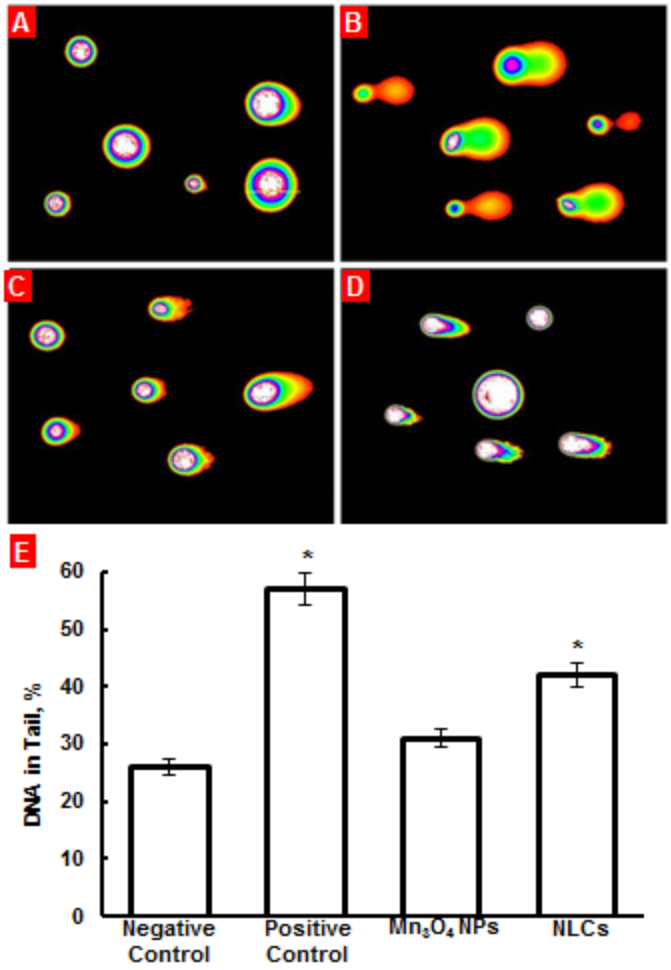

Figure 7.4 Genotoxicity of nanoparticles. (A-D) Representative fluorescence images of cells with DNA damage after treatment with (A) Negative control (fresh medium); (B) Positive control (hydrogen peroxide); (C) Mn_3O_4 NPs; (D) NLCs. (E) Quantitative analysis of genotoxicity evaluated using a comet assay method. Means ± SD are shown. *P < 0.05 when compared with negative control.

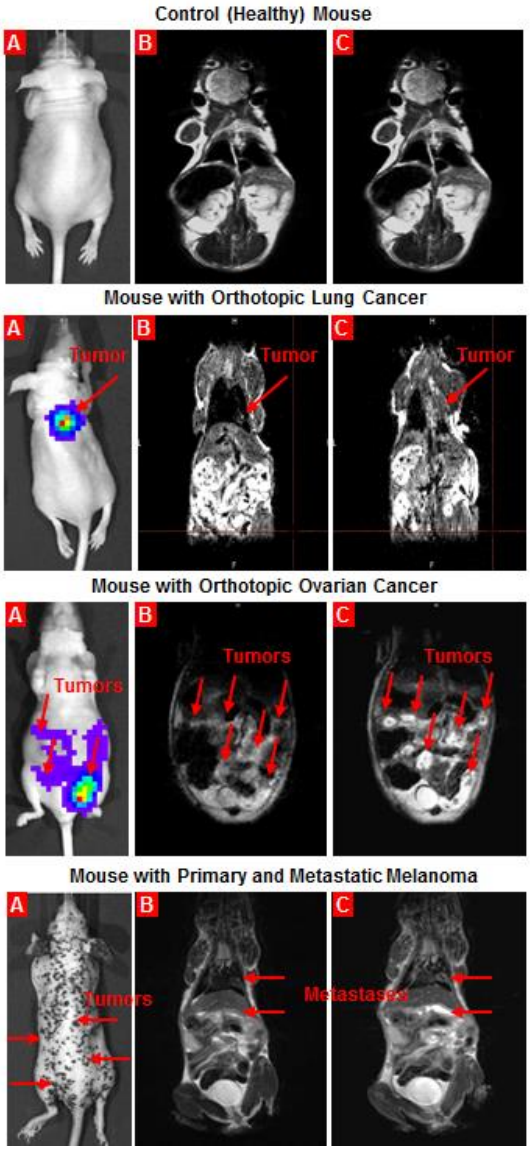

Figure 7.5 Enhancement in MRI sensitivity and specificity by cancer-targeted Mn_3O_4 nanoparticles. (A) Representative light or bioluminescence IVIS optical imaging. (B-C) Representative magnetic resonance imaging. (B) MRI without a contrast agent. (C) MRI after injection of biocompatible cancer-targeted Mn_3O_4 nanoparticles. Representative MR images are shown.

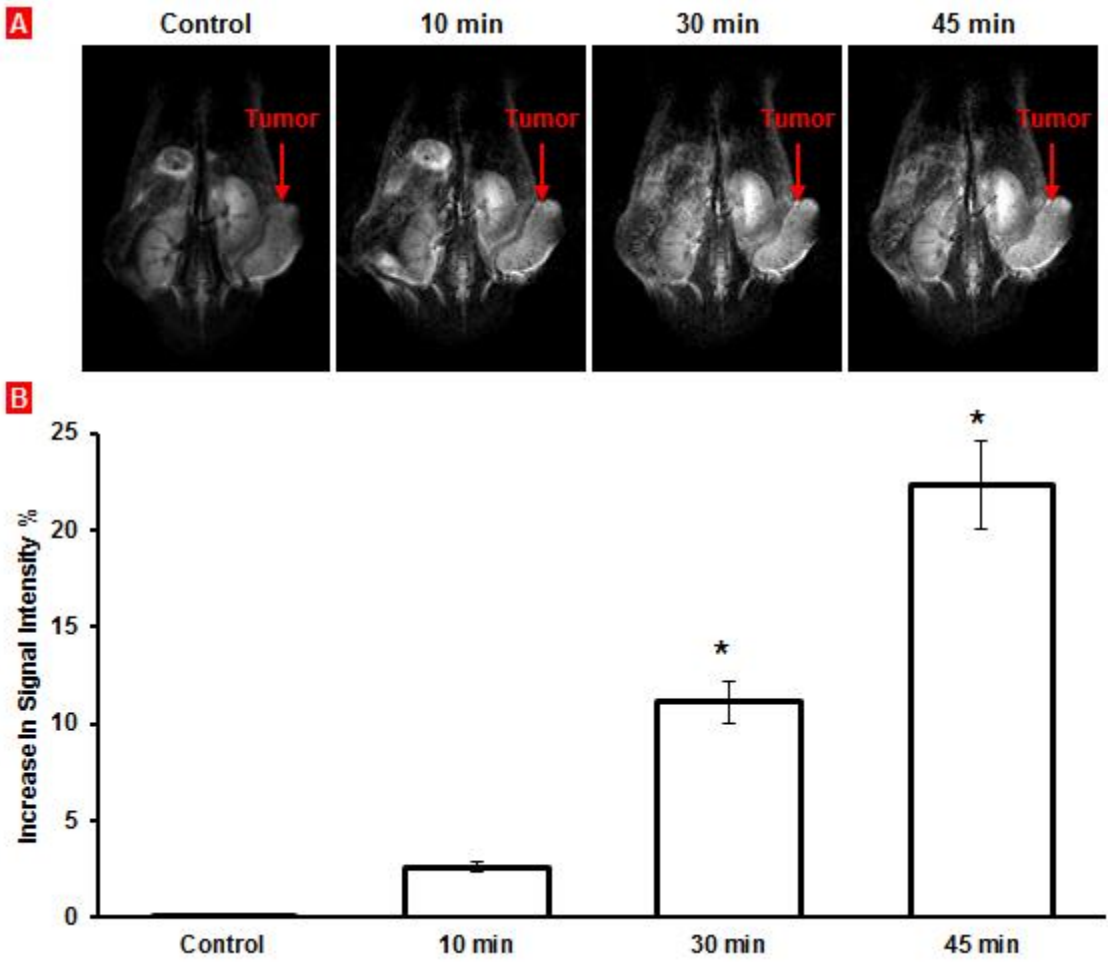

Figure 7.6 Distribution of cancer-targeted Mn_3O_4 nanoparticles and enhancement in MRI signal intensity. (A) Representative MR images of a mouse with subcutaneous xenografts of human ovarian cancer before (control) and 10, 30, and 45 min after injection of the nanoparticles. (B) Quantitative analysis of MRI signal intensity. Means ± SD are shown. *$P < 0.05$ when compared with control.

8 REFERENCES

1. Medina PJF, C. In: Dipiro JTT, R. L.; Yee, G. C.; Matzke, G. R.; Wells, B. G.; Posey, L. M., editor. Pharmacotherapy: A Pathophysiologic Approach. 7 ed. New York, NY: The McGraw-Hill Companies 2008. p. 2085-119.
2. Pelengaris SK, M. Introduction. In: Pelengaris SK, M., editor. The Molecular Biology of Cancer. Malden, MA: Blackwell Publishing; 2006. p. 1-34.
3. Siegel R, Ma J, Zou Z, Jemal A. Cancer statistics, 2014. CA: a cancer journal for clinicians. 2014;64(1):9-29.
4. Thomas ALS, R. A.; Steward, W. P. Treatment of Cancer: Chemotherapy and Radiotherapy. In: Pelengaris SK, M., editor. The Molecular Biology of Cancer. Malden, MA: Blackwell Publishing; 2006. p. 444-63.
5. Fang C, Zhang M. Nanoparticle-based theragnostics: Integrating diagnostic and therapeutic potentials in nanomedicine. J Control Release. 2010;146(1):2-5.
6. Grobmyer SR, Iwakuma N, Sharma P, Moudgil BM. What is cancer nanotechnology? Methods in molecular biology. 2010;624:1-9.
7. Cho K, Wang X, Nie S, Chen ZG, Shin DM. Therapeutic nanoparticles for drug delivery in cancer. Clin Cancer Res. 2008;14(5):1310-6.
8. Farokhzad OC, Langer R. Impact of nanotechnology on drug delivery. ACS Nano. 2009;3(1):16-20.
9. Jain KK. Advances in the field of nanooncology. BMC medicine. 2010;8:83.
10. Gullotti E, Yeo Y. Extracellularly activated nanocarriers: a new paradigm of tumor targeted drug delivery. Mol Pharm. 2009;6(4):1041-51.
11. Chen Y, Yin Q, Ji X, Zhang S, Chen H, Zheng Y, et al. Manganese oxide-based multifunctionalized mesoporous silica nanoparticles for pH-responsive MRI, ultrasonography and circumvention of MDR in cancer cells. Biomaterials. 2012;33(29):7126-37.
12. Lee YC, Chen DY, Dodd SJ, Bouraoud N, Koretsky AP, Krishnan KM. The Use of Silica Coated MnO Nanoparticles to Control MRI Relaxivity in Response to Specific Physiological Changes. Biomaterials. 2012;33(13):3560-7.
13. Yang H, Zhuang YM, Hu H, Du XX, Zhang CX, Shi XY, et al. Silica-Coated Manganese Oxide Nanoparticles as a Platform for Targeted Magnetic Resonance and Fluorescence Imaging of Cancer Cells. Adv Funct Mater. 2010;20(11):1733-41.
14. Huang WY, Davis JJ. Multimodality and nanoparticles in medical imaging. Dalton T. 2011;40(23):6087-103.
15. Masters JR, Koberle B. Curing metastatic cancer: lessons from testicular germ-cell tumours. Nat Rev Cancer. 2003;3(7):517-25.
16. McCubrey JA, Steelman LS, Chappell WH, Abrams SL, Wong EW, Chang F, et al. Roles of the Raf/MEK/ERK pathway in cell growth, malignant transformation and drug resistance. Biochimica et biophysica acta. 2007;1773(8):1263-84.
17. Gray-Schopfer V, Wellbrock C, Marais R. Melanoma biology and new targeted therapy. Nature. 2007;445(7130):851-7.

18. Haferkamp S, Borst A, Adam C, Becker TM, Motschenbacher S, Windhovel S, et al. Vemurafenib induces senescence features in melanoma cells. The Journal of investigative dermatology. 2013;133(6):1601-9.
19. Chapman PB, Hauschild A, Robert C, Haanen JB, Ascierto P, Larkin J, et al. Improved survival with vemurafenib in melanoma with BRAF V600E mutation. The New England journal of medicine. 2011;364(26):2507-16.
20. McArthur GA, Chapman PB, Robert C, Larkin J, Haanen JB, Dummer R, et al. Safety and efficacy of vemurafenib in BRAF and BRAF mutation-positive melanoma (BRIM-3): extended follow-up of a phase 3, randomised, open-label study. The lancet oncology. 2014.
21. Pakunlu RI, Wang Y, Saad M, Khandare JJ, Starovoytov V, Minko T. In vitro and in vivo intracellular liposomal delivery of antisense oligonucleotides and anticancer drug. J Control Release. 2006;114(2):153-62.
22. Wong HL, Bendayan R, Rauth AM, Xue HY, Babakhanian K, Wu XY. A mechanistic study of enhanced doxorubicin uptake and retention in multidrug resistant breast cancer cells using a polymer-lipid hybrid nanoparticle system. J Pharmacol Exp Ther. 2006;317(3):1372-81.
23. Elbashir SM, Lendeckel W, Tuschl T. RNA interference is mediated by 21-and 22-nucleotide RNAs. Gene Dev. 2001;15(2):188-200.
24. Dillon CP, Sandy P, Nencioni A, Kissler S, Rubinson DA, Van Parijs L. RNAI as an experimental and therapeutic tool to study and regulate physiological and disease processes. Annu Rev Physiol. 2005;67:147-73.
25. Fire A, Xu S, Montgomery MK, Kostas SA, Driver SE, Mello CC. Potent and specific genetic interference by double-stranded RNA in Caenorhabditis elegans. Nature. 1998;391(6669):806-11.
26. Kennerdell JR, Carthew RW. Use of dsRNA-mediated genetic interference to demonstrate that frizzled and frizzled 2 act in the wingless pathway. Cell. 1998;95(7):1017-26.
27. Oelgeschlager M, Larrain J, Geissert D, De Robertis EM. The evolutionarily conserved BMP-binding protein Twisted gastrulation promotes BMP signalling. Nature. 2000;405(6788):757-63.
28. Svoboda P, Stein P, Hayashi H, Schultz RM. Selective reduction of dormant maternal mRNAs in mouse oocytes by RNA interference. Development. 2000;127(19):4147-56.
29. Cogoni C, Macino G. Homology-dependent gene silencing in plants and fungi: a number of variations on the same theme. Current opinion in microbiology. 1999;2(6):657-62.
30. Ketting RF, Plasterk RHA. A genetic link between co-suppression and RNA interference in C-elegans. Nature. 2000;404(6775):296-8.
31. Zamore PD, Tuschl T, Sharp PA, Bartel DP. RNAi: double-stranded RNA directs the ATP-dependent cleavage of mRNA at 21 to 23 nucleotide intervals. Cell. 2000;101(1):25-33.
32. Chiu YL, Ali A, Chu CY, Cao H, Rana TM. Visualizing a correlation between siRNA localization, cellular uptake, and RNAi in living cells. Chem Biol. 2004;11(8):1165-75.

33. Dykxhoorn DM, Lieberman J. The silent revolution: RNA interference as basic biology, research tool, and therapeutic. Annual review of medicine. 2005;56:401-23.
34. Choung S, Kim YJ, Kim S, Park HO, Choi YC. Chemical modification of siRNAs to improve serum stability without loss of efficacy. Biochem Bioph Res Co. 2006;342(3):919-27.
35. Dominska M, Dykxhoorn DM. Breaking down the barriers: siRNA delivery and endosome escape. Journal of cell science. 2010;123(Pt 8):1183-9.
36. Rippe K, Mucke N, Langowski J. Superhelix dimensions of a 1868 base pair plasmid determined by scanning force microscopy in air and in aqueous solution. Nucleic acids research. 1997;25(9):1736-44.
37. Hagerman PJ. Flexibility of RNA. Annu Rev Bioph Biom. 1997;26:139-56.
38. Kebbekus P, Draper DE, Hagerman P. Persistence Length of Rna. Biochemistry. 1995;34(13):4354-7.
39. Shah SA, Brunger AT. The 1.8 angstrom crystal structure of a statically disordered 17 base-pair RNA duplex: Principles of RNA crystal packing and its effect on nucleic acid structure. J Mol Biol. 1999;285(4):1577-88.
40. Spagnou S, Miller AD, Keller M. Lipidic carriers of siRNA: differences in the formulation, cellular uptake, and delivery with plasmid DNA. Biochemistry. 2004;43(42):13348-56.
41. Bishop NE. An Update on Non-clathrin-coated Endocytosis. Reviews in medical virology. 1997;7(4):199-209.
42. Grayson AC, Doody AM, Putnam D. Biophysical and structural characterization of polyethylenimine-mediated siRNA delivery in vitro. Pharm Res. 2006;23(8):1868-76.
43. Bartlett DW, Davis ME. Insights into the kinetics of siRNA-mediated gene silencing from live-cell and live-animal bioluminescent imaging. Nucleic acids research. 2006;34(1):322-33.
44. Clayton J. RNA interference: the silent treatment. Nature. 2004;431(7008):599-605.
45. Gary DJ, Puri N, Won YY. Polymer-based siRNA delivery: Perspectives on the fundamental and phenomenological distinctions from polymer-based DNA delivery. Journal of Controlled Release. 2007;121(1-2):64-73.
46. Dokka S, Toledo D, Shi XG, Castranova V, Rojanasakul Y. Oxygen radical-mediated pulmonary toxicity induced by some cationic liposomes. Pharm Res. 2000;17(5):521-5.
47. Scheule RK, St George JA, Bagley RG, Marshall J, Kaplan JM, Akita GY, et al. Basis of pulmonary toxicity associated with cationic lipid-mediated gene transfer to the mammalian lung. Human gene therapy. 1997;8(6):689-707.
48. Freimark BD, Blezinger HP, Florack VJ, Nordstrom JL, Long SD, Deshpande DS, et al. Cationic lipids enhance cytokine and cell influx levels in the lung following administration of plasmid: cationic lipid complexes. J Immunol. 1998;160(9):4580-6.
49. Song YK, Liu F, Chu S, Liu D. Characterization of cationic liposome-mediated gene transfer in vivo by intravenous administration. Human gene therapy. 1997;8(13):1585-94.

50. Garbuzenko OB, Saad M, Betigeri S, Zhang M, Vetcher AA, Soldatenkov VA, et al. Intratracheal versus intravenous liposomal delivery of siRNA, antisense oligonucleotides and anticancer drug. Pharm Res. 2009;26(2):382-94.
51. Patil ML, Zhang M, Betigeri S, Taratula O, He H, Minko T. Surface-modified and internally cationic polyamidoamine dendrimers for efficient siRNA delivery. Bioconjug Chem. 2008;19(7):1396-403.
52. Taratula O, Garbuzenko OB, Kirkpatrick P, Pandya I, Savla R, Pozharov VP, et al. Surface-engineered targeted PPI dendrimer for efficient intracellular and intratumoral siRNA delivery. J Control Release. 2009;140(3):284-93.
53. Taratula O, Garbuzenko O, Savla R, Wang YA, He H, Minko T. Multifunctional nanomedicine platform for cancer specific delivery of siRNA by superparamagnetic iron oxide nanoparticles-dendrimer complexes. Curr Drug Deliv. 2011;8(1):59-69.
54. Kelkar SS, Reineke TM. Theranostics: Combining Imaging and Therapy. Bioconjug Chem. 2011;22(10):1879-903.
55. Klajnert B, Bryszewska M. Dendrimers: properties and applications. Acta biochimica Polonica. 2001;48(1):199-208.
56. Lee I, Athey BD, Wetzel AW, Meixner W, Baker JR. Structural molecular dynamics studies on polyamidoamine dendrimers for a therapeutic application: Effects of pH and generation. Macromolecules. 2002;35(11):4510-20.
57. Debrabandervandenberg EMM, Meijer EW. Poly(Propylene Imine) Dendrimers - Large-Scale Synthesis by Hetereogeneously Catalyzed Hydrogenations. Angewandte Chemie-International Edition in English. 1993;32(9):1308-11.
58. Hollins AJ, Benboubetra M, Omidi Y, Zinselmeyer BH, Schatzlein AG, Uchegbu IF, et al. Evaluation of generation 2 and 3 poly(propylenimine) dendrimers for the potential cellular delivery of antisense oligonucleotides targeting the epidermal growth factor receptor. Pharm Res. 2004;21(3):458-66.
59. Schatzlein AG, Zinselmeyer BH, Elouzi A, Dufes C, Chim YT, Roberts CJ, et al. Preferential liver gene expression with polypropylenimine dendrimers. J Control Release. 2005;101(1-3):247-58.
60. Vijayanathan V, Thomas T, Thomas TJ. DNA nanoparticles and development of DNA delivery vehicles for gene therapy. Biochemistry. 2002;41(48):14085-94.
61. Pack DW, Hoffman AS, Pun S, Stayton PS. Design and development of polymers for gene delivery. Nat Rev Drug Discov. 2005;4(7):581-93.
62. Malik N, Wiwattanapatapee R, Klopsch R, Lorenz K, Frey H, Weener JW, et al. Dendrimers: Relationship between structure and biocompatibility in vitro, and preliminary studies on the biodistribution of I-125-labelled polyamidoamine dendrimers in vivo (vol 65, pg 133, 2000). Journal of Controlled Release. 2000;68(2):299-302.
63. Agashe HB, Dutta T, Garg M, Jain NK. Investigations on the toxicological profile of functionalized fifth-generation poly (propylene imine) dendrimer. The Journal of pharmacy and pharmacology. 2006;58(11):1491-8.
64. Muller RH, Radtke M, Wissing SA. Solid lipid nanoparticles (SLN) and nanostructured lipid carriers (NLC) in cosmetic and dermatological preparations. Adv Drug Deliv Rev. 2002;54 Suppl 1:S131-55.

65. Das S, Ng WK, Tan RB. Are nanostructured lipid carriers (NLCs) better than solid lipid nanoparticles (SLNs): development, characterizations and comparative evaluations of clotrimazole-loaded SLNs and NLCs? European journal of pharmaceutical sciences : official journal of the European Federation for Pharmaceutical Sciences. 2012;47(1):139-51.
66. Wong HL, Bendayan R, Rauth AM, Li Y, Wu XY. Chemotherapy with anticancer drugs encapsulated in solid lipid nanoparticles. Adv Drug Deliv Rev. 2007;59(6):491-504.
67. zur Muhlen A, Schwarz C, Mehnert W. Solid lipid nanoparticles (SLN) for controlled drug delivery--drug release and release mechanism. Eur J Pharm Biopharm. 1998;45(2):149-55.
68. Fang JY, Fang CL, Liu CH, Su YH. Lipid nanoparticles as vehicles for topical psoralen delivery: solid lipid nanoparticles (SLN) versus nanostructured lipid carriers (NLC). Eur J Pharm Biopharm. 2008;70(2):633-40.
69. Saupe A, Gordon KC, Rades T. Structural investigations on nanoemulsions, solid lipid nanoparticles and nanostructured lipid carriers by cryo-field emission scanning electron microscopy and Raman spectroscopy. International journal of pharmaceutics. 2006;314(1):56-62.
70. Cho EC, Glaus C, Chen J, Welch MJ, Xia Y. Inorganic nanoparticle-based contrast agents for molecular imaging. Trends in molecular medicine. 2010;16(12):561-73.
71. Huang HC, Barua S, Sharma G, Dey SK, Rege K. Inorganic nanoparticles for cancer imaging and therapy. J Control Release. 2011;155(3):344-57.
72. Cormode DP, Sanchez-Gaytan BL, Mieszawska AJ, Fayad ZA, Mulder WJM. Inorganic nanocrystals as contrast agents in MRI: synthesis, coating and introduction of multifunctionality. Nmr Biomed. 2013;26(7):766-80.
73. Jokerst JV, Lobovkina T, Zare RN, Gambhir SS. Nanoparticle PEGylation for imaging and therapy. Nanomedicine (Lond). 2011;6(4):715-28.
74. Kim J, Lee JE, Lee SH, Yu JH, Lee JH, Park TG, et al. Designed fabrication of a multifunctional polymer nanomedical platform for simultaneous cancer-targeted imaging and magnetically guided drug delivery. Adv Mater. 2008;20(3):478-+.
75. Kircher MF, Mahmood U, King RS, Weissleder R, Josephson L. A multimodal nanoparticle for preoperative magnetic resonance imaging and intraoperative optical brain tumor delineation. Cancer research. 2003;63(23):8122-5.
76. Selvan ST, Patra PK, Ang CY, Ying JY. Synthesis of silica-coated semiconductor and magnetic quantum dots and their use in the imaging of live cells. Angew Chem Int Edit. 2007;46(14):2448-52.
77. Dosev D, Nichkova M, Dumas RK, Gee SJ, Hammock BD, Liu K, et al. Magnetic/luminescent core/shell particles synthesized by spray pyrolysis and their application in immunoassays with internal standard. Nanotechnology. 2007;18(5):55102.
78. Bennewitz MF, Lobo TL, Nkansah MK, Ulas G, Brudvig GW, Shapiro EM. Biocompatible and pH-Sensitive PLGA Encapsulated MnO Nanocrystals for Molecular and Cellular MRI. ACS Nano. 2011;5(5):3438-46.

79. Munnier E, Cohen-Jonathan S, Linassier C, Douziech-Eyrolles L, Marchais H, Souce M, et al. Novel method of doxorubicin-SPION reversible association for magnetic drug targeting. International journal of pharmaceutics. 2008;363(1-2):170-6.
80. Rosen JE, Chan L, Shieh DB, Gu FX. Iron oxide nanoparticles for targeted cancer imaging and diagnostics. Nanomed-Nanotechnol. 2012;8(3):275-90.
81. Chen F, Hong H, Zhang Y, Valdovinos HF, Shi S, Kwon GS, et al. In vivo tumor targeting and image-guided drug delivery with antibody-conjugated, radiolabeled mesoporous silica nanoparticles. ACS Nano. 2013;7(10):9027-39.
82. Liu H, Wang H, Xu Y, Shen M, Zhao J, Zhang G, et al. Synthesis of PEGylated low generation dendrimer-entrapped gold nanoparticles for CT imaging applications. Nanoscale. 2014.
83. Curry T, Kopelman R, Shilo M, Popovtzer R. Multifunctional theranostic gold nanoparticles for targeted CT imaging and photothermal therapy. Contrast media & molecular imaging. 2014;9(1):53-61.
84. Aryal S, Key J, Stigliano C, Landis MD, Lee DY, Decuzzi P. Positron Emitting Magnetic Nanoconstructs for PET/MR Imaging. Small. 2014.
85. Lee S, Kang SW, Ryu JH, Na JH, Lee DE, Han SJ, et al. Tumor-Homing Glycol Chitosan-Based Optical/PET Dual Imaging Nanoprobe for Cancer Diagnosis. Bioconjug Chem. 2014;25(3):601-10.
86. Yin M, O'Brien S. Synthesis of monodisperse nanocrystals of manganese oxides. J Am Chem Soc. 2003;125(34):10180-1.
87. Brunetti V, Chibli H, Fiammengo R, Galeone A, Malvindi MA, Vecchio G, et al. InP/ZnS as a safer alternative to CdSe/ZnS core/shell quantum dots: in vitro and in vivo toxicity assessment. Nanoscale. 2013;5(1):307-17.
88. Pelley JL, Daar AS, Saner MA. State of Academic Knowledge on Toxicity and Biological Fate of Quantum Dots. Toxicol Sci. 2009;112(2):276-96.
89. Nehilla BJ, Allen PG, Desai TA. Surfactant-free, drug-quantum-dot coloaded poly(lactide-co-glycolide) nanoparticles: towards multifunctional nanoparticles. ACS Nano. 2008;2(3):538-44.
90. Wu SM, Zhao X, Zhang ZL, Xie HY, Tian ZQ, Peng J, et al. Quantum-dot-labeled DNA probes for fluorescence in situ hybridization (FISH) in the microorganism Escherichia coli. Chemphyschem : a European journal of chemical physics and physical chemistry. 2006;7(5):1062-7.
91. Smith AM, Duan H, Mohs AM, Nie S. Bioconjugated quantum dots for in vivo molecular and cellular imaging. Adv Drug Deliv Rev. 2008;60(11):1226-40.
92. Medintz IL, Mattoussi H. Quantum dot-based resonance energy transfer and its growing application in biology. Physical chemistry chemical physics : PCCP. 2009;11(1):17-45.
93. Bruchez M, Moronne M, Gin P, Weiss S, Alivisatos AP. Semiconductor nanocrystals as fluorescent biological labels. Science. 1998;281(5385):2013-6.
94. Murray CB, Norris DJ, Bawendi MG. Synthesis and Characterization of Nearly Monodisperse Cde (E = S, Se, Te) Semiconductor Nanocrystallites. J Am Chem Soc. 1993;115(19):8706-15.

95. Zhang LW, Monteiro-Riviere NA. Mechanisms of Quantum Dot Nanoparticle Cellular Uptake. Toxicol Sci. 2009;110(1):138-55.
96. Bagalkot V, Zhang L, Levy-Nissenbaum E, Jon S, Kantoff PW, Langer R, et al. Quantum dot-aptamer conjugates for synchronous cancer imaging, therapy, and sensing of drug delivery based on bi-fluorescence resonance energy transfer. Nano Lett. 2007;7(10):3065-70.
97. Juzenas P, Chen W, Sun YP, Coelho MA, Generalov R, Generalova N, et al. Quantum dots and nanoparticles for photodynamic and radiation therapies of cancer. Adv Drug Deliv Rev. 2008;60(15):1600-14.
98. Bae KH, Lee K, Kim C, Park TG. Surface functionalized hollow manganese oxide nanoparticles for cancer targeted siRNA delivery and magnetic resonance imaging. Biomaterials. 2011;32(1):176-84.
99. Akbarzadeh A, Samiei M, Davaran S. Magnetic nanoparticles: preparation, physical properties, and applications in biomedicine. Nanoscale research letters. 2012;7(1):144.
100. van der Zee J. Heating the patient: a promising approach? Ann Oncol. 2002;13(8):1173-84.
101. Kruse AM, Meenach SA, Anderson KW, Hilt JZ. Synthesis and characterization of CREKA-conjugated iron oxide nanoparticles for hyperthermia applications. Acta biomaterialia. 2014.
102. Gilchrist RK, Medal R, Shorey WD, Hanselman RC, Parrott JC, Taylor CB. Selective inductive heating of lymph nodes. Annals of surgery. 1957;146(4):596-606.
103. Sundaresan V, Menon JU, Rahimi M, Nguyen KT, Wadajkar AS. Dual-responsive polymer-coated iron oxide nanoparticles for drug delivery and imaging applications. International journal of pharmaceutics. 2014;466(1-2):1-7.
104. Kumar CS, Mohammad F. Magnetic nanomaterials for hyperthermia-based therapy and controlled drug delivery. Adv Drug Deliv Rev. 2011;63(9):789-808.
105. Na HB, Lee JH, An KJ, Park YI, Park M, Lee IS, et al. Development of a T-1 contrast agent for magnetic resonance imaging using MnO nanoparticles. Angew Chem Int Edit. 2007;46(28):5397-401.
106. Yu T, Moon J, Park J, Park YI, Bin Na H, Kim BH, et al. Various-Shaped Uniform Mn3O4 Nanocrystals Synthesized at Low Temperature in Air Atmosphere. Chem Mater. 2009;21(11):2272-9.
107. Pirollo KF, Chang EH. Does a targeting ligand influence nanoparticle tumor localization or uptake? Trends in biotechnology. 2008;26(10):552-8.
108. Khandare JJ, Chandna P, Wang Y, Pozharov VP, Minko T. Novel polymeric prodrug with multivalent components for cancer therapy. J Pharmacol Exp Ther. 2006;317(3):929-37.
109. Tolkach Y, Joniau S, Van Poppel H. Luteinizing hormone-releasing hormone (LHRH) receptor agonists vs antagonists: a matter of the receptors? BJU international. 2013;111(7):1021-30.
110. Grundker C, Gunthert AR, Westphalen S, Emons G. Biology of the gonadotropin-releasing hormone system in gynecological cancers. European journal of endocrinology / European Federation of Endocrine Societies. 2002;146(1):1-14.

111. Weckermann D, Harzmann R. Hormone therapy in prostate cancer: LHRH antagonists versus LHRH analogues. European urology. 2004;46(3):279-83; discussion 83-4.
112. Emons G, Sindermann H, Engel J, Schally AV, Grundker C. Luteinizing hormone-releasing hormone receptor-targeted chemotherapy using AN-152. Neuroendocrinology. 2009;90(1):15-8.
113. Dharap SS, Minko T. Targeted proapoptotic LHRH-BH3 peptide. Pharm Res. 2003;20(6):889-96.
114. Dharap SS, Wang Y, Chandna P, Khandare JJ, Qiu B, Gunaseelan S, et al. Tumor-specific targeting of an anticancer drug delivery system by LHRH peptide. Proc Natl Acad Sci U S A. 2005;102(36):12962-7.
115. Minko T, Patil ML, Zhang M, Khandare JJ, Saad M, Chandna P, et al. LHRH-targeted nanoparticles for cancer therapeutics. Methods in molecular biology. 2010;624:281-94.
116. Hollingsworth MA, Swanson BJ. Mucins in cancer: protection and control of the cell surface. Nat Rev Cancer. 2004;4(1):45-60.
117. Singh PK, Hollingsworth MA. Cell surface-associated mucins in signal transduction. Trends in cell biology. 2006;16(9):467-76.
118. Hikita ST, Kosik KS, Clegg DO, Bamdad C. MUC1* mediates the growth of human pluripotent stem cells. PloS one. 2008;3(10):e3312.
119. Wang L, Ma J, Liu F, Yu Q, Chu G, Perkins AC, et al. Expression of MUC1 in primary and metastatic human epithelial ovarian cancer and its therapeutic significance. Gynecologic oncology. 2007;105(3):695-702.
120. Pochampalli MR, el Bejjani RM, Schroeder JA. MUC1 is a novel regulator of ErbB1 receptor trafficking. Oncogene. 2007;26(12):1693-701.
121. Khodarev NN, Pitroda SP, Beckett MA, MacDermed DM, Huang L, Kufe DW, et al. MUC1-induced transcriptional programs associated with tumorigenesis predict outcome in breast and lung cancer. Cancer research. 2009;69(7):2833-7.
122. Ferreira CS, Matthews CS, Missailidis S. DNA aptamers that bind to MUC1 tumour marker: design and characterization of MUC1-binding single-stranded DNA aptamers. Tumour biology : the journal of the International Society for Oncodevelopmental Biology and Medicine. 2006;27(6):289-301.
123. Mahanta S, Fessler SP, Park J, Bamdad C. A minimal fragment of MUC1 mediates growth of cancer cells. PloS one. 2008;3(4):e2054.
124. Zuker M. Mfold web server for nucleic acid folding and hybridization prediction. Nucleic acids research. 2003;31(13):3406-15.
125. Gary DJ, Puri N, Won YY. Polymer-based siRNA delivery: perspectives on the fundamental and phenomenological distinctions from polymer-based DNA delivery. J Control Release. 2007;121(1-2):64-73.
126. Patil ML, Zhang M, Betigeri S, Taratula O, He H, Minko T. Surface-modified and internally cationic polyamidoamine dendrimers for efficient siRNA delivery. Bioconjug Chem. 2008;19(7):1396-403.

127. Patil ML, Zhang M, Taratula O, Garbuzenko OB, He H, Minko T. Internally cationic polyamidoamine PAMAM-OH dendrimers for siRNA delivery: effect of the degree of quaternization and cancer targeting. Biomacromolecules. 2009;10(2):258-66.
128. Saad M, Garbuzenko OB, Minko T. Co-delivery of siRNA and an anticancer drug for treatment of multidrug-resistant cancer. Nanomed. 2008;3(6):761-76.
129. Taratula O, Garbuzenko OB, Kirkpatrick P, Pandya I, Savla R, Pozharov VP, et al. Surface-engineered targeted PPI dendrimer for efficient intracellular and intratumoral siRNA delivery. J Control Release2009.
130. Zhou J, Wu J, Hafdi N, Behr JP, Erbacher P, Peng L. PAMAM dendrimers for efficient siRNA delivery and potent gene silencing. Chem Commun (Camb). 2006(22):2362-4.
131. Kang H, DeLong R, Fisher MH, Juliano RL. Tat-conjugated PAMAM dendrimers as delivery agents for antisense and siRNA oligonucleotides. Pharm Res. 2005;22(12):2099-106.
132. Bessis N, GarciaCozar FJ, Boissier MC. Immune responses to gene therapy vectors: influence on vector function and effector mechanisms. Gene Ther. 2004;11(Suppl 1):S10-7.
133. Shah SA, Brunger AT. The 1.8 A crystal structure of a statically disordered 17 base-pair RNA duplex: principles of RNA crystal packing and its effect on nucleic acid structure. J Mol Biol. 1999;285(4):1577-88.
134. Garbuzenko OB, Saad M, Betigeri S, Zhang M, Vetcher AA, Soldatenkov VA, et al. Intratracheal Versus Intravenous Liposomal Delivery of siRNA, Antisense Oligonucleotides and Anticancer Drug. Pharm Res. 2009;26(2):382-94.
135. Dufes C, Uchegbu IF, Schatzlein AG. Dendrimers in gene delivery. Adv Drug Deliv Rev. 2005;57(15):2177-202.
136. Chen A, Santhakumaran LM, Nair SK, Amenta PS, Thomas T, He H, et al. Oligodeoxynucleotide nanostructure formation in the presence of polypropyleneimine dendrimers and their uptake in breast cancer cells. Nanotechnology. 2006;17(21):5449-60.
137. Santhakumaran LM, Thomas T, Thomas TJ. Enhanced cellular uptake of a triplex-forming oligonucleotide by nanoparticle formation in the presence of polypropylenimine dendrimers. Nucleic Acids Res. 2004;32(7):2102-12.
138. Jayant S, Khandare JJ, Wang Y, Singh AP, Vorsa N, Minko T. Targeted sialic acid-doxorubicin prodrugs for intracellular delivery and cancer treatment. Pharm Res. 2007;24(11):2120-30.
139. Saad M, Garbuzenko OB, Ber E, Chandna P, Khandare JJ, Pozharov VP, et al. Receptor targeted polymers, dendrimers, liposomes: Which nanocarrier is the most efficient for tumor-specific treatment and imaging? J Control Release. 2008;130(2):107-14.
140. Pakunlu RI, Cook TJ, Minko T. Simultaneous modulation of multidrug resistance and antiapoptotic cellular defense by MDR1 and BCL-2 targeted antisense oligonucleotides enhances the anticancer efficacy of doxorubicin. Pharm Res. 2003;20(3):351-9.

141. Izumrudov VA, Zhiryakova MV, Kudaibergenov SE. Controllable stability of DNA-containing polyelectrolyte complexes in water-salt solutions. Biopolymers. 1999;52(2):94-108.
142. Thomas M, Lu JJ, Ge Q, Zhang C, Chen J, Klibanov AM. Full deacylation of polyethylenimine dramatically boosts its gene delivery efficiency and specificity to mouse lung. Proc Natl Acad Sci U S A. 2005;102(16):5679-84.
143. Oh JK, Tang C, Gao H, Tsarevsky NV, Matyjaszewski K. Inverse miniemulsion ATRP: a new method for synthesis and functionalization of well-defined water-soluble/cross-linked polymeric particles. J Am Chem Soc. 2006;128(16):5578-84.
144. Kunath K, von Harpe A, Fischer D, Kissel T. Galactose-PEI-DNA complexes for targeted gene delivery: degree of substitution affects complex size and transfection efficiency. J Control Release. 2003;88(1):159-72.
145. Zinselmeyer BH, Mackay SP, Schatzlein AG, Uchegbu IF. The lower-generation polypropylenimine dendrimers are effective gene-transfer agents. Pharm Res. 2002;19(7):960-7.
146. Rietveld IB, Smit JAM. Colligative and viscosity properties of poly(propyleneimine) dendrimers in methanol. Macromolecules. 1999;32(14):4608-14.
147. Guillot-Nieckowski M, Eisler S, Diederich F. Dendritic vectors for gene transfection. New J Chem. 2007;31(7):1111-27.
148. Dennig J, Duncan E. Gene transfer into eukaryotic cells using activated polyamidoamine dendrimers. J Biotechnol. 2002;90(3-4):339-47.
149. Kabanov VA, Sergeyev VG, Pyshkina OA, Zinchenko AA, Zezin AB, Joosen JGH, et al. Interpolyelectrolyte complexes formed by DNA and astramol poly(propylene imine) dendrimers. Macromolecules. 2000;33(26):9587-93.
150. Liu G, Molas M, Grossmann GA, Pasumarthy M, Perales JC, Cooper MJ, et al. Biological properties of poly-L-lysine-DNA complexes generated by cooperative binding of the polycation. J Biol Chem. 2001;276(37):34379-87.
151. Chiu YL, Ali A, Chu CY, Cao H, Rana TM. Visualizing a correlation between siRNA localization, cellular uptake, and RNAi in living cells. Chem Biol. 2004;11(8):1165-75.
152. Keller M. Lipidic carriers of RNA/DNA oligonucleotides and polynucleotides: what a difference a formulation makes! J Control Release. 2005;103(3):537-40.
153. Bloomfield VA. DNA condensation. Curr Opin Struct Biol. 1996;6(3):334-41.
154. van Duijvenbode RC, Borkovec M, Koper GJM. Acid-base properties of poly(propylene imine)dendrimers. Polymer. 1998;39(12):2657-64.
155. Devi GR. siRNA-based approaches in cancer therapy. Cancer gene therapy. 2006;13(9):819-29.
156. Chang Z, Hu Z. RNAi therapeutics: can siRNAs conquer SARS? Gene therapy. 2006;13(11):871-2.
157. Rozema DB, Lewis DL, Wakefield DH, Wong SC, Klein JJ, Roesch PL, et al. Dynamic PolyConjugates for targeted in vivo delivery of siRNA to hepatocytes. Proc Natl Acad Sci U S A. 2007;104(32):12982-7.
158. Betigeri S, Pakunlu RI, Wang Y, Khandare JJ, Minko T. JNK1 as a molecular target to limit cellular mortality under hypoxia. Mol Pharm. 2006;3(4):424-30.

159. Uprichard SL. The therapeutic potential of RNA interference. FEBS letters. 2005;579(26):5996-6007.
160. Ikeda Y, Taira K. Ligand-targeted delivery of therapeutic siRNA. Pharm Res. 2006;23(8):1631-40.
161. Akhtar S, Benter IF. Nonviral delivery of synthetic siRNAs in vivo. J Clin Invest. 2007;117(12):3623-32.
162. Crombez L, Charnet A, Morris MC, Aldrian-Herrada G, Heitz F, Divita G. A non-covalent peptide-based strategy for siRNA delivery. Biochem Soc T. 2007;35:44-6.
163. Bessis N, GarciaCozar FJ, Boissier MC. Immune responses to gene therapy vectors: influence on vector function and effector mechanisms. Gene therapy. 2004;11 Suppl 1:S10-7.
164. Medarova Z, Pham W, Farrar C, Petkova V, Moore A. In vivo imaging of siRNA delivery and silencing in tumors. Nat Med. 2007;13(3):372-7.
165. Saad M, Garbuzenko OB, Minko T. Co-delivery of siRNA and an anticancer drug for treatment of multidrug-resistant cancer. Nanomedicine (Lond). 2008;3(6):761-76.
166. Ogris M, Brunner S, Schuller S, Kircheis R, Wagner E. PEGylated DNA/transferrin-PEI complexes: reduced interaction with blood components, extended circulation in blood and potential for systemic gene delivery. Gene therapy. 1999;6(4):595-605.
167. Oupicky D, Carlisle RC, Seymour LW. Triggered intracellular activation of disulfide crosslinked polyelectrolyte gene delivery complexes with extended systemic circulation in vivo. Gene therapy. 2001;8(9):713-24.
168. Wang X, Yang LL, Chen Z, Shin DM. Application of nanotechnology in cancer therapy and imaging. Ca-Cancer J Clin. 2008;58(2):97-110.
169. Atri M. New technologies and directed agents for applications of cancer imaging. J Clin Oncol. 2006;24(20):3299-308.
170. Thorek DLJ, Chen A, Czupryna J, Tsourkas A. Superparamagnetic iron oxide nanoparticle probes for molecular imaging. Ann Biomed Eng. 2006;34(1):23-38.
171. Lee JH, Lee K, Moon SH, Lee Y, Park TG, Cheon J. All-in-One Target-Cell-Specific Magnetic Nanoparticles for Simultaneous Molecular Imaging and siRNA Delivery. Angew Chem Int Edit. 2009;48(23):4174-9.
172. Boyer C, Priyanto P, Davis TP, Pissuwan D, Bulmus V, Kavallaris M, et al. Anti-fouling magnetic nanoparticles for siRNA delivery. J Mater Chem. 2010;20(2):255-65.
173. Pan BF, Cui DX, Sheng Y, Ozkan CG, Gao F, He R, et al. Dendrimer-modified magnetic nanoparticles enhance efficiency of gene delivery system. Cancer research. 2007;67(17):8156-63.
174. Oliveira S, Storm G, Schiffelers RM. Targeted delivery of siRNA. J Biomed Biotechnol. 2006.
175. Kim SH, Jeong JH, Mok H, Lee SH, Kim SW, Park TG. Folate receptor targeted delivery of polyelectrolyte complex micelles prepared from ODN-PEG-Folate conjugate and cationic lipids. Biotechnol Progr. 2007;23(1):232-7.
176. Kularatne SA, Low PS. Targeting of nanoparticles: folate receptor. Methods in molecular biology. 2010;624:249-65.

177. Dharap SS, Qiu B, Williams GC, Sinko P, Stein S, Minko T. Molecular targeting of drug delivery systems to ovarian cancer by BH3 and LHRH peptides. Journal of Controlled Release. 2003;91(1-2):61-73.
178. Chandna P, Saad M, Wang Y, Ber E, Khandare J, Vetcher AA, et al. Targeted proapoptotic anticancer drug delivery system. Mol Pharm. 2007;4(5):668-78.
179. Saad M, Garbuzenko OB, Ber E, Chandna P, Khandare JJ, Pozharov VP, et al. Receptor targeted polymers, dendrimers, liposomes: which nanocarrier is the most efficient for tumor-specific treatment and imaging? J Control Release. 2008;130(2):107-14.
180. Yu WW, Chang E, Sayes CM, Drezek R, Colvin VL. Aqueous dispersion of monodisperse magnetic iron oxide nanocrystals through phase transfer. Nanotechnology. 2006;17(17):4483-7.
181. Yang LL, Peng XH, Wang YA, Wang XX, Cao ZH, Ni CC, et al. Receptor-Targeted Nanoparticles for In vivo Imaging of Breast Cancer. Clinical Cancer Research. 2009;15(14):4722-32.
182. Pakunlu RI, Wang Y, Tsao W, Pozharov V, Cook TJ, Minko T. Enhancement of the efficacy of chemotherapy for lung cancer by simultaneous suppression of multidrug resistance and antiapoptotic cellular defense: novel multicomponent delivery system. Cancer research. 2004;64(17):6214-24.
183. Wang Y, Saad M, Pakunlu RI, Khandare JJ, Garbuzenko OB, Vetcher AA, et al. Nonviral nanoscale-based delivery of antisense oligonucleotides targeted to hypoxia-inducible factor 1 alpha enhances the efficacy of chemotherapy in drug-resistant tumor. Clin Cancer Res. 2008;14(11):3607-16.
184. Fischer D, Osburg B, Petersen H, Kissel T, Bickel U. Effect of poly(ethylene imine) molecular weight and pegylation on organ distribution and pharmacokinetics of polyplexes with oligodeoxynucleotides in mice. Drug metabolism and disposition: the biological fate of chemicals. 2004;32(9):983-92.
185. Wood KC, Little SR, Langer R, Hammond PT. A family of hierarchically self-assembling linear-dendritic hybrid polymers for highly efficient targeted gene delivery. Angewandte Chemie. 2005;44(41):6704-8.
186. Omidi Y, Hollins AJ, Drayton RM, Akhtar S. Polypropylenimine dendrimer-induced gene expression changes: the effect of complexation with DNA, dendrimer generation and cell type. J Drug Target. 2005;13(7):431-43.
187. de Wolf HK, Snel CJ, Verbaan FJ, Schiffelers RM, Hennink WE, Storm G. Effect of cationic carriers on the pharmacokinetics and tumor localization of nucleic acids after intravenous administration. International journal of pharmaceutics. 2007;331(2):167-75.
188. Dash PR, Read ML, Barrett LB, Wolfert MA, Seymour LW. Factors affecting blood clearance and in vivo distribution of polyelectrolyte complexes for gene delivery. Gene therapy. 1999;6(4):643-50.
189. Schiffelers RM, Ansari A, Xu J, Zhou Q, Tang Q, Storm G, et al. Cancer siRNA therapy by tumor selective delivery with ligand-targeted sterically stabilized nanoparticle. Nucleic acids research. 2004;32(19):e149.
190. Mao S, Neu M, Germershaus O, Merkel O, Sitterberg J, Bakowsky U, et al. Influence of polyethylene glycol chain length on the physicochemical and biological

properties of poly(ethylene imine)-graft-poly(ethylene glycol) block copolymer/SiRNA polyplexes. Bioconjug Chem. 2006;17(5):1209-18.
191. See HTKJJ. Ovarian Cancer. In: Kantarjian H. M.; Wolff RAKCA, editor. MD Anderson Manual of Medical Oncology. New York, NY: The McGraw-Hill Companies; 2006.
192. Jemal A, Siegel R, Ward E, Murray T, Xu J, Smigal C, et al. Cancer statistics, 2006. CA: a cancer journal for clinicians. 2006;56(2):106-30.
193. Brennan KMB, V. V.; Dorigo, O. Premalignant & Malignant Disorders of the Ovaries & Oviducts. In: De Cherney AHN, L., editor. CURRENT Diagnosis & Treatment Obstetrics & Gynecology. 10 ed. New York, NY: The McGraw-Hill Companies; 2007.
194. Smith JAW, J. K. Ovarian Cancer. In: Dipiro JTT, R. L.; Yee, G. C.; Matzke, G. R.; Wells, B. G.; Posey, L. M., editor. Pharmacotherapy: A Pathophysiologic Approach. 7 ed. New York, NY: The McGraw-Hill Companies; 2008. p. 2245-58.
195. Visintin I, Feng Z, Longton G, Ward DC, Alvero AB, Lai Y, et al. Diagnostic markers for early detection of ovarian cancer. Clin Cancer Res. 2008;14(4):1065-72.
196. Bast RC, Jr., Hennessy B, Mills GB. The biology of ovarian cancer: new opportunities for translation. Nat Rev Cancer. 2009;9(6):415-28.
197. Markman M, Bookman MA. Second-line treatment of ovarian cancer. The oncologist. 2000;5(1):26-35.
198. Porche DJ. Liposomal doxorubicin (Doxil). The Journal of the Association of Nurses in AIDS Care : JANAC. 1996;7(2):55-9.
199. Steppan I, Reimer D, Sevelda U, Ulmer H, Marth C, Zeimet AG. Treatment of recurrent platinum-resistant ovarian cancer with pegylated liposomal doxorubicin--an evaluation of the therapeutic index with special emphasis on cardiac toxicity. Chemotherapy. 2009;55(6):391-8.
200. Tejada-Berges T, Granai CO, Gordinier M, Gajewski W. Caelyx/Doxil for the treatment of metastatic ovarian and breast cancer. Expert review of anticancer therapy. 2002;2(2):143-50.
201. Malugin A, Kopeckova P, Kopecek J. Liberation of doxorubicin from HPMA copolymer conjugate is essential for the induction of cell cycle arrest and nuclear fragmentation in ovarian carcinoma cells. J Control Release. 2007;124(1-2):6-10.
202. Prabaharan M, Grailer JJ, Pilla S, Steeber DA, Gong S. Gold nanoparticles with a monolayer of doxorubicin-conjugated amphiphilic block copolymer for tumor-targeted drug delivery. Biomaterials. 2009;30(30):6065-75.
203. Lebold T, Jung C, Michaelis J, Brauchle C. Nanostructured silica materials as drug-delivery systems for Doxorubicin: single molecule and cellular studies. Nano Lett. 2009;9(8):2877-83.
204. Lai PS, Lou PJ, Peng CL, Pai CL, Yen WN, Huang MY, et al. Doxorubicin delivery by polyamidoamine dendrimer conjugation and photochemical internalization for cancer therapy. J Control Release. 2007;122(1):39-46.
205. Oskay-Ozcelik G, Sehouli J. Pros and cons for systemic therapy in recurrent ovarian cancer. Anticancer research. 2009;29(7):2831-6.
206. Minko T, Dharap SS, Pakunlu RI, Wang Y. Molecular targeting of drug delivery systems to cancer. Current drug targets. 2004;5(4):389-406.

207. Bakalova R, Ohba H, Zhelev Z, Ishikawa M, Baba Y. Quantum dots as photosensitizers? Nature biotechnology. 2004;22(11):1360-1.
208. Bae Y, Alani AW, Rockich NC, Lai TS, Kwon GS. Mixed pH-sensitive polymeric micelles for combination drug delivery. Pharm Res. 2010;27(11):2421-32.
209. Yuan Q, Yeudall WA, Yang H. PEGylated polyamidoamine dendrimers with bis-aryl hydrazone linkages for enhanced gene delivery. Biomacromolecules. 2010;11(8):1940-7.
210. Kale AA, Torchilin VP. Environment-responsive multifunctional liposomes. Methods in molecular biology. 2010;605:213-42.
211. Aryal S, Hu CMJ, Zhang LF. Polymer-Cisplatin Conjugate Nanoparticles for Acid-Responsive Drug Delivery. ACS Nano. 2010;4(1):251-8.
212. Banerjee SS, Chen DH. Multifunctional pH-sensitive magnetic nanoparticles for simultaneous imaging, sensing and targeted intracellular anticancer drug delivery. Nanotechnology. 2008;19(50):505104.
213. Minko T, Kopeckova P, Pozharov V, Kopecek J. HPMA copolymer bound adriamycin overcomes MDR1 gene encoded resistance in a human ovarian carcinoma cell line. J Control Release. 1998;54(2):223-33.
214. Etrych T, Jelinkova M, Rihova B, Ulbrich K. New HPMA copolymers containing doxorubicin bound via pH-sensitive linkage: synthesis and preliminary in vitro and in vivo biological properties. J Control Release. 2001;73(1):89-102.
215. Lee CC, Gillies ER, Fox ME, Guillaudeu SJ, Frechet JMJ, Dy EE, et al. A single dose of doxorubicin-functionalized bow-tie dendrimer cures mice bearing C-26 colon carcinomas. Proc Natl Acad Sci U S A. 2006;103(45):16649-54.
216. Jares-Erijman EA, Jovin TM. FRET imaging. Nature biotechnology. 2003;21(11):1387-95.
217. Hruby M, Konak C, Ulbrich K. Polymeric micellar pH-sensitive drug delivery system for doxorubicin. Journal of Controlled Release. 2005;103(1):137-48.
218. Minko T, Kopeckova P, Kopecek J. Comparison of the anticancer effect of free and HPMA copolymer-bound adriamycin in human ovarian carcinoma cells. Pharm Res. 1999;16(7):986-96.
219. Fang C, Zhang M. Nanoparticle-based theragnostics: Integrating diagnostic and therapeutic potentials in nanomedicine. Journal of controlled release : official journal of the Controlled Release Society. 2010;146(1):2-5.
220. Frangioni JV. In vivo near-infrared fluorescence imaging. Current opinion in chemical biology. 2003;7(5):626-34.
221. Ntziachristos V, Ripoll J, Weissleder R. Would near-infrared fluorescence signals propagate through large human organs for clinical studies? Errata. Optics letters. 2002;27(18):1652.
222. Chandna P, Khandare JJ, Ber E, Rodriguez-Rodriguez L, Minko T. Multifunctional tumor-targeted polymer-peptide-drug delivery system for treatment of primary and metastatic cancers. Pharmaceutical research. 2010;27(11):2296-306.
223. Khandare JJ, Chandna P, Wang Y, Pozharov VP, Minko T. Novel polymeric prodrug with multivalent components for cancer therapy. The Journal of pharmacology and experimental therapeutics. 2006;317(3):929-37.

224. Shah V, Taratula O, Garbuzenko OB, Taratula OR, Rodriguez-Rodriguez L, Minko T. Targeted Nanomedicine for Suppression of CD44 and Simultaneous Cell Death Induction in Ovarian Cancer: An Optimal Delivery of siRNA and Anticancer Drug. Clin Cancer Res. 2013.
225. Taratula O, Kuzmov A, Shah M, Garbuzenko OB, Minko T. Nanostructured lipid carriers as multifunctional nanomedicine platform for pulmonary co-delivery of anticancer drugs and siRNA. J Control Release. 2013;171(3):349-57.
226. Zhang M, Garbuzenko OB, Reuhl KR, Rodriguez-Rodriguez L, Minko T. Two-in-one: combined targeted chemo and gene therapy for tumor suppression and prevention of metastases. Nanomedicine (Lond). 2012;7(2):185-97.
227. Howell M, Mallela J, Wang C, Ravi S, Dixit S, Garapati U, et al. Manganese-loaded lipid-micellar theranostics for simultaneous drug and gene delivery to lungs. Journal of controlled release : official journal of the Controlled Release Society. 2013;167(2):210-8.
228. Pan D, Caruthers SD, Senpan A, Schmieder AH, Wickline SA, Lanza GM. Revisiting an old friend: manganese-based MRI contrast agents. Wiley interdisciplinary reviews Nanomedicine and nanobiotechnology. 2010.
229. Minko T, Kopeckova P, Kopecek J. Chronic exposure to HPMA copolymer-bound adriamycin does not induce multidrug resistance in a human ovarian carcinoma cell line. Journal of controlled release : official journal of the Controlled Release Society. 1999;59(2):133-48.
230. Matsumura Y, Gotoh M, Muro K, Yamada Y, Shirao K, Shimada Y, et al. Phase I and pharmacokinetic study of MCC-465, a doxorubicin (DXR) encapsulated in PEG immunoliposome, in patients with metastatic stomach cancer. Annals of oncology : official journal of the European Society for Medical Oncology / ESMO. 2004;15(3):517-25.
231. Matsumura Y. Poly (amino acid) micelle nanocarriers in preclinical and clinical studies. Advanced drug delivery reviews. 2008;60(8):899-914.
232. Batist G, Gelmon KA, Chi KN, Miller WH, Jr., Chia SK, Mayer LD, et al. Safety, pharmacokinetics, and efficacy of CPX-1 liposome injection in patients with advanced solid tumors. Clin Cancer Res. 2009;15(2):692-700.
233. Seymour LW, Ferry DR, Kerr DJ, Rea D, Whitlock M, Poyner R, et al. Phase II studies of polymer-doxorubicin (PK1, FCE28068) in the treatment of breast, lung and colorectal cancer. International journal of oncology. 2009;34(6):1629-36.
234. Valle JW, Armstrong A, Newman C, Alakhov V, Pietrzynski G, Brewer J, et al. A phase 2 study of SP1049C, doxorubicin in P-glycoprotein-targeting pluronics, in patients with advanced adenocarcinoma of the esophagus and gastroesophageal junction. Investigational new drugs. 2011;29(5):1029-37.
235. Patil ML, Zhang M, Minko T. Multifunctional triblock Nanocarrier (PAMAM-PEG-PLL) for the efficient intracellular siRNA delivery and gene silencing. ACS Nano. 2011;5(3):1877-87.
236. Huang ZR, Hua SC, Yang YL, Fang JY. Development and evaluation of lipid nanoparticles for camptothecin delivery: a comparison of solid lipid nanoparticles, nanostructured lipid carriers, and lipid emulsion. Acta pharmacologica Sinica. 2008;29(9):1094-102.

237. Li X, Nie SF, Kong J, Li N, Ju CY, Pan WS. A controlled-release ocular delivery system for ibuprofen based on nanostructured lipid carriers. International journal of pharmaceutics. 2008;363(1-2):177-82.
238. Muller RH, Radtke M, Wissing SA. Solid lipid nanoparticles (SLN) and nanostructured lipid carriers (NLC) in cosmetic and dermatological preparations. Advanced drug delivery reviews. 2002;54 Suppl 1:S131-55.
239. Fang JY, Fang CL, Liu CH, Su YH. Lipid nanoparticles as vehicles for topical psoralen delivery: solid lipid nanoparticles (SLN) versus nanostructured lipid carriers (NLC). European journal of pharmaceutics and biopharmaceutics : official journal of Arbeitsgemeinschaft fur Pharmazeutisc. 2008;70(2):633-40.
240. Zhu L, Kate P, Torchilin VP. Matrix Metalloprotease 2-Responsive Multifunctional Liposomal Nanocarrier for Enhanced Tumor Targeting. ACS Nano. 2012;6(4):3491-8.
241. Serrat FB. 3,3 ',5,5 '-Tetramethylbenzidine for the colorimetric determination of manganese in water. Mikrochim Acta. 1998;129(1-2):77-80.
242. Zheng Y, Thomas-Schoemann A, Sakji L, Boudou-Rouquette P, Dupin N, Mortier L, et al. An HPLC-UV method for the simultaneous quantification of vemurafenib and erlotinib in plasma from cancer patients. J Chromatogr B. 2013;928:93-7.
243. Savla R, Taratula O, Garbuzenko O, Minko T. Tumor targeted quantum dot-mucin 1 aptamer-doxorubicin conjugate for imaging and treatment of cancer. J Control Release. 2011;153(1):16-22.
244. Garbuzenko OB, Saad M, Pozharov VP, Reuhl KR, Mainelis G, Minko T. Inhibition of lung tumor growth by complex pulmonary delivery of drugs with oligonucleotides as suppressors of cellular resistance. Proc Natl Acad Sci U S A. 2010;107(23):10737-42.
245. Taratula O, Garbuzenko OB, Chen AM, Minko T. Innovative strategy for treatment of lung cancer: targeted nanotechnology-based inhalation co-delivery of anticancer drugs and siRNA. J Drug Target. 2011;19(10):900-14.
246. Alb M, Sie C, Adam C, Chen S, Becker JC, Schrama D. Cellular and cytokine-dependent immunosuppressive mechanisms of grm1-transgenic murine melanoma. Cancer immunology, immunotherapy : CII. 2012;61(12):2239-49.
247. Schiffner S, Chen S, Becker JC, Bosserhoff AK. Highly pigmented Tg(Grm1) mouse melanoma develops non-pigmented melanoma cells in distant metastases. Experimental dermatology. 2012;21(10):786-8.
248. Singh A, Sahoo SK. Magnetic nanoparticles: a novel platform for cancer theranostics. Drug discovery today. 2013.
249. Seong SY, Matzinger P. Hydrophobicity: an ancient damage-associated molecular pattern that initiates innate immune responses. Nature reviews Immunology. 2004;4(6):469-78.
250. Egeblad M, Werb Z. New functions for the matrix metalloproteinases in cancer progression. Nature reviews Cancer. 2002;2(3):161-74.
251. Park J, Kang EA, Bae CJ, Park JG, Noh HJ, Kim JY, et al. Synthesis, characterization, and magnetic properties of uniform-sized MnO nanospheres and nanorods. J Phys Chem B. 2004;108(36):13594-8.
252. Tong S, Hou SJ, Ren BB, Zheng ZL, Bao G. Self-Assembly of Phospholipid-PEG Coating on Nanoparticles through Dual Solvent Exchange. Nano Lett. 2011;11(9):3720-6.

253. Garbuzenko O, Barenholz Y, Priev A. Effect of grafted PEG on liposome size and on compressibility and packing of lipid bilayer. Chemistry and physics of lipids. 2005;135(2):117-29.
254. Gupta AK, Gupta M. Synthesis and surface engineering of iron oxide nanoparticles for biomedical applications. Biomaterials. 2005;26(18):3995-4021.
255. Uner M. Preparation, characterization and physico-chemical properties of solid lipid nanoparticles (SLN) and nanostructured lipid carriers (NLC): their benefits as colloidal drug carrier systems. Die Pharmazie. 2006;61(5):375-86.
256. Bocca C, Caputo O, Cavalli RB, Gabriel L, Miglietta A, Gasco MR. Phagocytic uptake of fluorescent stealth and non-stealth solid lipid nanoparticles. International journal of pharmaceutics. 1998;175(2):185-93.
257. Weller A, Barber JL, Olsen OE. Gadolinium and nephrogenic systemic fibrosis: an update. Pediatric nephrology. 2013.
258. Gallo J, Long NJ, Aboagye EO. Magnetic nanoparticles as contrast agents in the diagnosis and treatment of cancer. Chem Soc Rev. 2013;42(19):7816-33.
259. Shah V, Taratula O, Garbuzenko OB, Patil ML, Savla R, Zhang M, et al. Genotoxicity of different nanocarriers: possible modifications for the delivery of nucleic acids. Curr Drug Discov Technol. 2013;10(1):8-15.